

Condition-Based Maintenance

Guest Editors: Nezhir Mrad, Peter Foote, Victor Giurgiutiu,
and Jérôme Pinsonnault





Condition-Based Maintenance

International Journal of Aerospace Engineering

Condition-Based Maintenance

Guest Editors: Nezhir Mrad, Peter Foote, Victor Giurgiutiu,
and Jérôme Pinsonnault



Copyright © 2013 Hindawi Publishing Corporation. All rights reserved.

This is a special issue published in "International Journal of Aerospace Engineering." All articles are open access articles distributed under the Creative Commons Attribution License, which permits unrestricted use, distribution, and reproduction in any medium, provided the original work is properly cited.

Editorial Board

- Noor Afzal, India
Brij N. Agrawal, USA
Saad A. Ahmed, UAE
C. B. Allen, UK
N. Ananthkrishnan, India
Hikmat Asadov, Azerbaijan
Nicolas Avdelidis, Greece
Hyochoong Bang, Korea
Wen Bao, China
Ronald M. Barrett, USA
D. Bhattacharyya, New Zealand
Keh-Chin Chang, Taiwan
C. J. Damaren, Canada
Roger L. Davis, USA
Gang Ding, China
Dany Dionne, Canada
Boris Epstein, Israel
Jinghong Fan, China
Jiancheng Fang, China
Ikkoh Funaki, Japan
Mohamed Gad-el-Hak, USA
R. Ganguli, India
M. R. Hajj, USA
Kathleen C. Howell, USA
Qinglei Hu, China
- Hui Hu, USA
Mikhail S. Ivanov, Russia
Ratneshwar Jha, USA
Jacob I. Kleiman, Canada
John B. Kosmatka, USA
Hamid M. Lankarani, USA
Yunhua Li, China
T. T. Lim, Singapore
Rick Lind, USA
W. W. Liou, USA
Richard W. Longman, USA
Enrico C. Lorenzini, Italy
T. J. Lu, UK
Siao Chung Luo, Singapore
Joseph Majdalani, USA
Pier Marzocca, USA
Josep Masdemont, Spain
Philippe Masson, USA
Franco Mastroddi, Italy
James J. McGuirk, UK
Giovanni Mengali, Italy
Achille Messac, USA
Koorosh Mirfakhraie, USA
Hong Nie, China
C. O. Paschereit, Germany
- Chris L. Pettit, USA
Mark Price, UK
N. Qin, UK
Markus Raffel, Germany
Srinivasan Raghunathan, UK
Mahmut Reyhanoglu, USA
Corin Segal, USA
Kenneth M. Sobel, USA
K. Sudhakar, India
Martin Tajmar, Germany
Paolo Tortora, Italy
Jean-Yves Trépanier, Canada
Srinivas R. Vadali, USA
Linda L. Vahala, USA
Mehdi Vahdati, UK
George Vukovich, Canada
Shaoping Wang, China
Paul Williams, The Netherlands
R. K. Yedavalli, USA
Youngbin Yoon, Korea
Huang Yuan, Germany
Gecheng Zha, USA
Youmin Zhang, Canada
Xiaolin Zhong, USA
Mei Zhuang, USA

Contents

Condition-Based Maintenance, Nezhir Mrad, Peter Foote, Victor Giurgiutiu, and Jérôme Pinsonnault
Volume 2013, Article ID 348532, 2 pages

A Methodological Review of Piezoelectric Based Acoustic Wave Generation and Detection Techniques for Structural Health Monitoring, Zhigang Sun, Bruno Rocha, Kuo-Ting Wu, and Nezhir Mrad
Volume 2013, Article ID 928627, 22 pages

Operational Readiness Simulator: Optimizing Operational Availability Using a Virtual Environment, Shaun Horning, Philip Leung, Andy Fitzgerald, and Nezhir Mrad
Volume 2012, Article ID 804747, 8 pages

Integrated Instrumentation and Sensor Systems Enabling Condition-Based Maintenance of Aerospace Equipment, Richard C. Millar
Volume 2012, Article ID 804747, 6 pages

Assessment of Combustor Working Environments, Leiyong Jiang and Andrew Corber
Volume 2012, Article ID 217463, 6 pages

Corrosion Sensor Development for Condition-Based Maintenance of Aircraft, Gino Rinaldi, Trisha Huber, Heather McIntosh, Les Lebrun, Heping Ding, and John Weber
Volume 2012, Article ID 684024, 11 pages

Editorial

Condition-Based Maintenance

Nezih Mrad,¹ Peter Foote,² Victor Giurgiutiu,³ and Jérôme Pinsonnault⁴

¹ *Defence Research and Development Canada (DRDC), Centre for Security Science (CSS), National Defence Headquarters, Ottawa, ON, Canada K1A 0K7*

² *Manufacturing and Materials Department, School of Applied Sciences, Cranfield University, Cranfield, Bedfordshire MK43 0AL, UK*

³ *Department of Mechanical Engineering, University of South Carolina, Columbia, SC 29208, USA*

⁴ *Bombardier Aerospace, Station Centre-ville, Montreal, QC, Canada H3C 3G9*

Correspondence should be addressed to Nezih Mrad; nezih.mrad@drdc-rddc.gc.ca

Received 27 January 2013; Accepted 27 January 2013

Copyright © 2013 Nezih Mrad et al. This is an open access article distributed under the Creative Commons Attribution License, which permits unrestricted use, distribution, and reproduction in any medium, provided the original work is properly cited.

The drive to reduce aircraft operation and support (O&S) costs, increase platform availability, and enhance their performance and safety has motivated researchers, technology developers, aircraft manufacturers, and fleet operators to explore effective concepts, methodologies, and technologies as an alternative to the traditional schedule-based maintenance philosophy.

Condition-based maintenance (CBM), also known as “predictive maintenance,” is a maintenance practice that derives maintenance requirements, in large part, from real-time assessment of platform or weapon system condition obtained from embedded sensors and/or external tests and measurements using built-in diagnostic equipment. When coupled with real-time asset data, sophisticated materials, and structural and propulsion models, it promises the delivery of enhanced effectiveness of maintenance programs, preventing unplanned downtime, making better use of maintenance resources, and maximizing the operational life of the asset.

Our analysis indicated that the areas with the highest level of contribution to CBM are sensor technologies, health assessment and analytics (diagnostic and prognostic methods), communications technologies, and decisions support. This issue on CBM addresses all identified areas and focuses on maturing the understanding of the contributing concepts and technologies to achieve a wider implementation of CBM, particularly in the aerospace and defence sectors.

Miller presented the use of a systems’ engineering approach to guide the development of integrated instrumentation/sensor systems (IISS) and concluded that such

approach provides clear benefits in identifying the overall system requirements and architectural framework for categorizing and evaluating alternative architectures. While Miller effectively addressed the instrumentation functional features such as interrogation of sensor types, sensors interfaces, multiplexing, and communication to provide flexibility and rapid system reconfiguration to adapt to evolving sensor and data needs, G. Rinaldi et al. focused on a specific structural issue and presented a novel approach to aid in shifting time-based maintenance schedules towards condition-based maintenance procedures. The proposed novel approach demonstrated the innovation in the design of integrated microelectromechanical- (MEMS-) based multiparameters sensing using carbon nanotube/polyaniline polymer sensors for corrosion sensing and monitoring of aircraft structural materials (e.g., aluminium alloys). Through fusion of the multiparameters sensor data (chloride ion concentration, hydrogen gas evolution, humidity variations, and material degradation), a corrosion index was developed to be used in a condition-based maintenance protocol consisting of both preventative and corrective maintenance scheduling. Due to the criticality of sensor data in the CBM framework, Zhigang et al. presented a meticulous and well-thought-out review of piezoelectric-based acoustic wave generation and detection techniques for structural applications. They reviewed a variety of ingenious ways on how piezoelectric transducers are used in today’s structural health monitoring (SHM) methodologies as a means for generation and/or detection of diagnostic acoustic waves. Although this review presented three different approaches, all-piezoelectric

approaches, hybrid approaches, and wireless excitation and detection techniques, these can easily be integrated to provide a more powerful solution to specific problems (e.g., wireless fiber-acoustic approach).

While the above discussed contributions focused on addressing sensor issues for structural applications, L. Jiang and A. Corber presented a thermal fluid dynamics modeling and analysis of a gas turbine engine combustor. This effort is to define the aerothermodynamic working environments and service histories that will enable the assessment of the remaining life of gas turbine critical components, hence significantly reducing the cost and time of gas turbine engine fleet management. Their results illustrated a complicated (uneven distribution) flow features inside a combustor and the need for future improved modeling tools.

Not only key processes, technologies, concepts, and methodologies are critical to the cost-effective implementation of efficient CBM but also decisions support. S. Horning et al. developed and demonstrated an operational readiness simulator for optimizing maintenance activities and operational availability focussing on a rotary wing aircraft. The developed simulator provides a synthetic environment to forecast and assess the ability of a fleet, squadron, or aircraft to achieve the desired flying rates and the capability of the sustainment systems to respond to the resultant demands, while maintaining efficient and optimized maintenance program. They used this virtual simulator to assess several operational scenarios including adjustment of preventative maintenance schedules, including impact of condition-based maintenance, variation of the annual flying rate, and investigation of deployment options.

By compiling these selected papers, we hope to provide an opportunity to researchers, practitioners, and operators with the opportunity to enrich their knowledge in increasing the operational acceptability of the condition-based maintenance approach, particularly within the aerospace sector and air weapons systems.

Nezih Mrad
Peter Foote
Victor Giurgiutiu
Jérôme Pinsonnault

Review Article

A Methodological Review of Piezoelectric Based Acoustic Wave Generation and Detection Techniques for Structural Health Monitoring

Zhigang Sun,¹ Bruno Rocha,² Kuo-Ting Wu,¹ and Nezhir Mrad³

¹ Energy, Mining and Environment Portfolio, National Research Council Canada, Boucherville, QC, Canada J4B 6Y4

² Aerospace Portfolio, National Research Council Canada, Ottawa, ON, Canada K1A 0R6

³ Operational Analysis and Systems Integration Support, Defence R&D Canada-Atlantic, Department of National Defence, Ottawa, ON, Canada K1A 0K

Correspondence should be addressed to Zhigang Sun; zhigang.sun@cnrc-nrc.gc.ca

Received 21 August 2012; Revised 19 December 2012; Accepted 25 December 2012

Academic Editor: Victor Giurgiutiu

Copyright © 2013 Zhigang Sun et al. This is an open access article distributed under the Creative Commons Attribution License, which permits unrestricted use, distribution, and reproduction in any medium, provided the original work is properly cited.

Piezoelectric transducers have a long history of applications in nondestructive evaluation of material and structure integrity owing to their ability of transforming mechanical energy to electrical energy and vice versa. As condition based maintenance has emerged as a valuable approach to enhancing continued aircraft airworthiness while reducing the life cycle cost, its enabling structural health monitoring (SHM) technologies capable of providing on-demand diagnosis of the structure without interrupting the aircraft operation are attracting increasing R&D efforts. Piezoelectric transducers play an essential role in these endeavors. This paper is set forth to review a variety of ingenious ways in which piezoelectric transducers are used in today's SHM technologies as a means of generation and/or detection of diagnostic acoustic waves.

1. Introduction

Piezoelectric transducers are omnipresent in modern human life, from a kitchen gas lighter to popular gadgets such as smart phones and tablet computers, from submarine sonar to medical echography systems, and from electric watches to more dedicated measurement devices such as accelerometers for aircraft vibration monitoring and pressure sensors in jet engines for engine operation monitoring. Piezoelectric transducers can be used either as an actuator, for example, as the ultrasonic motor in a camera lens, or as a sensor, as in the case of an ultrasonic fish finder. These transducers can be used stand-alone, as are the case of conventional ultrasonic nondestructive evaluation (NDE) and nondestructive inspection (NDI) sensors, or be an integrated part of microelectromechanical systems (MEMS). The piezoelectric elements can also be used as harvesters of mechanical vibration energy.

From an acoustic point of view, there is no difference between SHM and conventional NDE/NDI since both rely

on the same physics in the sense that in either case acoustic waves need to be generated and then detected, independently of the acoustic wave mode or method used. What truly differentiates an SHM approach from an NDE/NDI approach is that the former usually requires the sensing elements to be permanently mounted on or embedded in the structure to be evaluated while allowing the wave generation elements, if active wave generation is used by the inspection method, to be either permanently mounted or mobile, whereas in the latter case both wave generation and detection elements are mobile. The requirement of permanently installed SHM sensors, and in some cases, of acoustic wave generation devices, poses challenges and at the same time spurs the development of new sensing concepts which are not practicable in conventional NDE/NDI. The main objective of this paper is to review some of these unique concepts. Since the focus is on presenting the concepts, there will be no attempt to review all existing works which implement a same idea. Instead, the idea will be presented only through representative cases. It is important

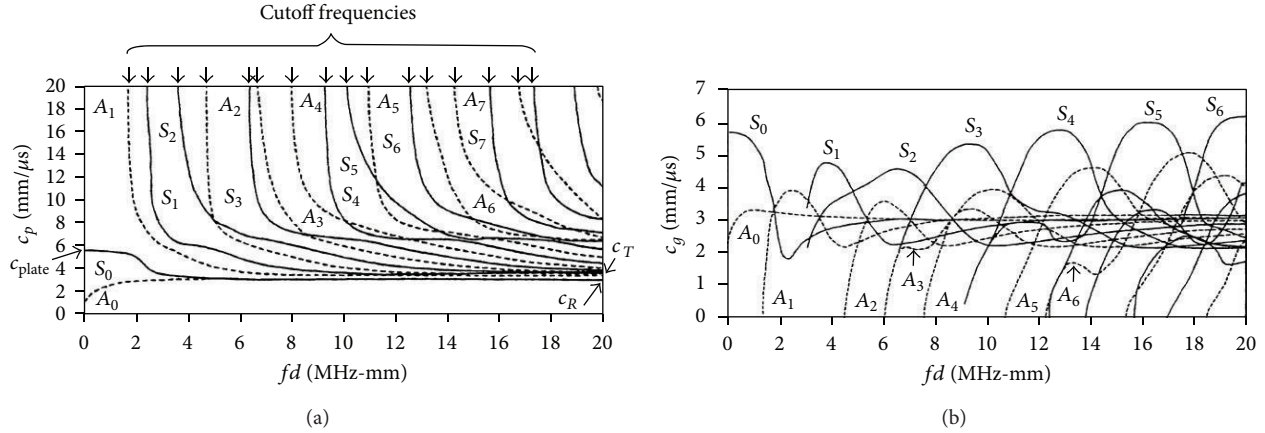


FIGURE 1: Dispersion curves for a traction free aluminum plate (the classic Lamb wave problem): (a) phase velocity dispersion curves and (b) group velocity dispersion curves [1, 2].

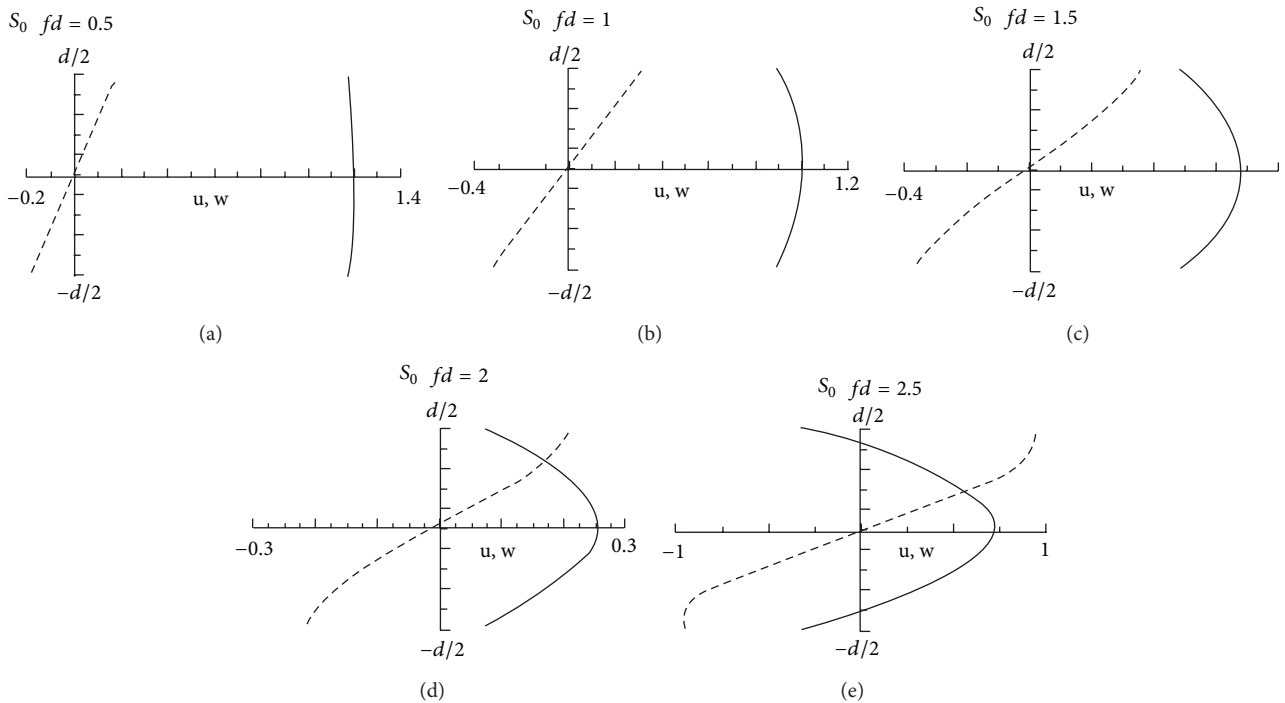


FIGURE 2: A wave structure for various points (particle displacements) for the S_0 mode in an aluminum plate, showing the in-plane (u —solid line) and out-of-plane (w —dashed line) displacement profiles across the thickness of the plate, for different wave frequency and plate thickness products [1, 2].

to note that as sensors, piezoelectric transducers can be used in acoustic and nonacoustic based techniques. Piezoelectric pressure sensors, accelerometers, and structural electromechanical impedance sensors are examples of nonacoustic applications of piezoelectric transducers. Although these sensors are widely used in SHM, they are not within the scope of the present paper.

This paper is divided into three sections. The first section is dedicated to all-piezoelectric acoustic based approaches in

which piezoelectric transducers are used for both generation and detection of acoustic waves. The second section presents hybrid approaches in which either piezoelectric transducers are used for acoustic wave generation (i.e., as exciters) and a nonpiezoelectric transducer based technique is used for wave detection or are used for wave detection whereas a nonpiezoelectric based technique is used for acoustic wave generation. The third section is devoted to wireless wave generation and detection techniques.

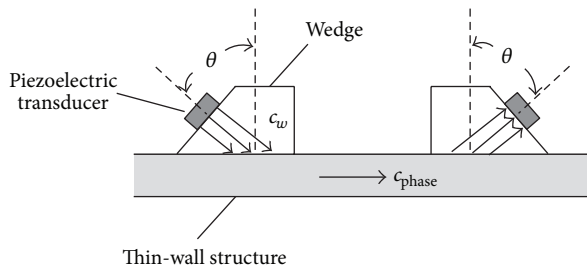


FIGURE 3: Wave tuning using a wedge.



FIGURE 4: Olympus NDT variable angle beam wedge.

2. All-Piezoelectric Approaches

2.1. Some Basics. Thin-wall structural elements such as shells, plates, and pipes are building blocks of aircraft structures. While NDE/NDI techniques are in their majority applied in localized areas of the structure, employing through-the-thickness wave propagation, SHM of aerospace structures via acoustic based techniques inevitably necessitates detection, and possibly also generation of acoustic waves propagating in thin-wall structures. Since these waves' propagation is confined in a thin layer and being guided by the two close-by and parallel (or quasiparallel) free surface boundaries in a thin-wall member, they are usually called guided plate acoustic waves. Because of their confinement in a thin-wall structure and the close-by free surface boundary conditions, guided acoustic waves can travel over a long distance, even in high acoustic attenuating materials such as carbon fiber-reinforced composites (CFRP). This long distance reaching capability makes guided acoustic waves a powerful tool for evaluation of thin-wall structure integrity, broadening the inspection area and enabling the inspection of multiple sites in a thin-wall member with a limited number of transducers—smaller than the number of mounted transducers that would have to be used for the application of through-the-thickness propagating waves in a conventional NDE/NDI fashion.

There are two types of guided acoustic waves that can propagate in thin-wall structures. The first type is called Lamb

waves to honor the British mathematician Horace Lamb who was the first to prove mathematically the existence of this type of waves, publishing a comprehensive analysis in 1917 [4]. Lamb waves can be decomposed into particle vibrations in two orthogonal (polarization) directions: one in line with wave propagation direction, also called in-plane direction, and another one perpendicular to both wave propagation direction and the wall surface, also called out-of-plane direction. Particle vibrations in these two directions are coupled. Depending on the vibration strength in each direction across wall thickness, different vibration patterns (modes) are formed. The second type of waves is horizontally polarized shear waves that vibrate in a direction perpendicular to the wave propagation direction and parallel to the wall surface. Owing to relative easiness of generation and detection with conventional piezoelectric acoustic transducers, Lamb waves are used more widely than shear horizontal (SH) waves for NDE/NDI of structures.

By nature, guided acoustic waves are multimodal and frequency dispersive. This means that a plurality of particle vibration patterns (modes) can coexist in the same structure and each vibration pattern propagates at a different speed. Furthermore, the propagation speed and the vibration pattern of each mode can vary with the frequency of the wave. This multi-modal and dispersive nature can make a diagnostic signal so complicated that even an expert may not be able to extract relevant information about the structure integrity from the signal. For this reason, a great deal of applications in acoustic NDE/NDI has been focused on how to selectively generate and single out one or two simple modes of the generated acoustic waves and to make signal interpretation much less prohibitive while ensuring that the selected mode is sensitive to the defects or damage to detect—a process often called “tuning.” For example, the detection of through-the-thickness cracks with the pulse-echo method is considerably more successful with the use of the fundamental symmetric mode (usually denoted by S_0) than with the fundamental antisymmetric mode (usually denoted by A_0). On the other hand, A_0 mode seems to be better suited for the detection of delaminations, disbonds, and corrosion with pitch-catch acoustoultrasonics techniques [5]. The fundamental symmetric mode (S_0) consists in a traction-compression occurring parallel to the wave propagation direction and free surface boundaries and mid-plane of the thin-wall structural element where the wave propagates with the particles presenting a symmetric displacement with respect to the mid-plane of the structural component. The fundamental antisymmetric mode (A_0) consists in a bending wave, with the main movement of the particles in the cross section of the thin-wall structural element being out of plane, that is, perpendicular to the wave propagation direction and to the free surface boundaries and mid-plane of the thin-wall structural member, and with the particles presenting an anti-symmetric movement with respect to its mid-plane. The wave generation and receiving transducers should be “tuned” in order to enhance a specific mode while suppressing others.

The dispersive behavior of Lamb waves is represented by the dispersion curves, depicting the relationship between different wave characteristics which must be considered to

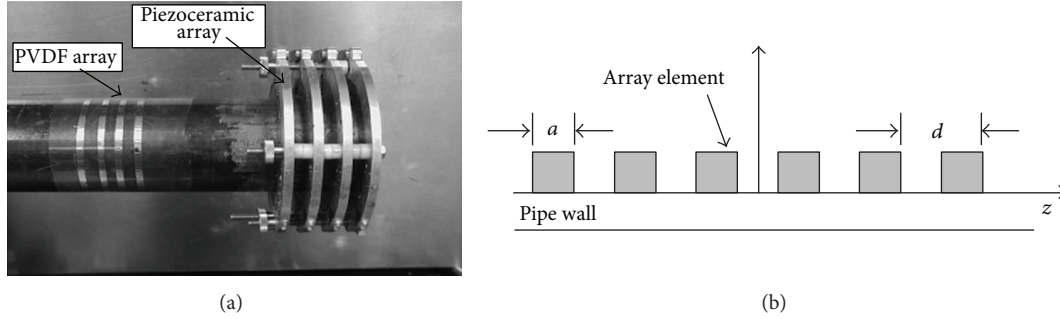


FIGURE 5: (a) Four-element PVDF and piezoceramic arrays and (b) array geometry [3].

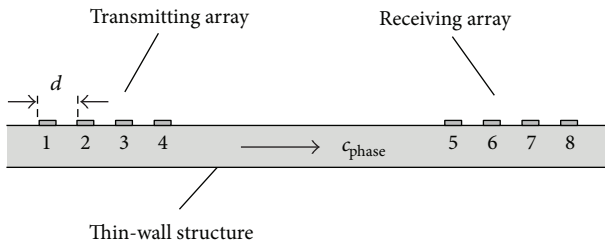


FIGURE 6: Phased arrays for tuned wave generation and detection.

accomplish an effective tuning. For a thin-wall structural element with a certain thickness and made of a specific material, the dispersion curves present the dependence of wave phase velocity and group velocity on the wave frequency. The dependence of the waves' velocity on their frequency also results in a dependence of the wavelength on wave frequency. In Figure 1, the dispersion curves for the fundamental, 1st order, 2nd order, and so forth, symmetrical modes of Lamb waves, respectively, S_0 , S_1 , S_2 , and so forth, are presented. In addition, the dispersion curves for the anti-symmetrical modes of corresponding orders to A_0 , A_1 , A_2 , and so forth are depicted. In these figures fd represents the product of the frequency and the plate thickness. As depicted in Figure 2, for different Lamb wave modes, wave displacement profiles across the thin-wall member cross section are different. The first step in a tuning process consists, therefore, in the selection of the mode to apply (detect and potentially generate) in the inspection method. Afterwards, in an active technique, the excitation frequency of the wave generation transducer (exciter) must be selected. Generally, it is preferable to select an excitation frequency at which the following requirements are met as much as possible for the selected mode: (1) frequency dispersion of the phase velocity is minimal, that is; the slope in the phase velocity dispersion curve is minimal for a frequency range around the selected frequency (to minimize signal width spreading in time as a result of its propagation in space), at these frequencies the group velocity approximates well the phase velocity; (2) its group velocity differs sufficiently from those of other modes that coexist in the structure (to minimize the chance of observing the merge of different propagating wave modes); (3) wave displacement profile favors desired sensing of certain

physical properties or defects; (4) wave displacement at the structure surface is easily detectable with the wave detection means. For example, if a longitudinal wave transducer is used, the displacement profile (f) in Figure 2 may be preferable to profile (a) due to much larger out-of-plane displacement at $fd = 3$ and the fact that a longitudinal transducer is sensitive to out-of-plane wave motion. If a shear wave transducer polarized in the wave propagation direction is used, then profile (a) could be preferable to profile (d) because the shear wave transducer senses in-plane wave motion at the surface which is stronger in case (a). Depending on the application, used method and defects to detect, some of the above rules may not apply. For example, if the inspection method is based on the use of wave dispersion for structure integrity evaluation, then it may be preferable to excite the transducer at a frequency where the desired mode manifests significant frequency dispersion (i.e., a sharp slope in the dispersion curve). Some key characteristics of guided acoustic wave inspection and its applications in SHM are summarized in [6].

2.2. Tuned Wave Excitation and Detection with Wedge Transducers. In the previous section, the importance of wave mode and wave frequency selections was explained in terms of the phase and group velocity dispersion curves and wave structure. In a practical application, the wave mode and frequency can be defined effortlessly by controlling the generated wave frequency through an electric excitation device. Furthermore, the selection of phase velocity can be realized by using a wedge. Let c_w be the velocity of the acoustic waves (longitudinal or transverse) in the wedge, c_{phase} the phase velocity of a desired wave mode at a selected frequency in the thin-wall structure, and θ the incident angle of the acoustic waves impinging on the structure, as depicted in Figure 3. According to Snell's law, acoustic waves with a phase velocity of c_{phase} will be enhanced through phase matching, much more than waves of any other phase velocities, if the following condition is met:

$$\sin \theta = \frac{c_w}{c_{\text{phase}}}. \quad (1)$$

Therefore, a wedge and transducer pair can be used for tuned wave excitation and detection as well. Examples of applying this wave tuning method to anomaly detection

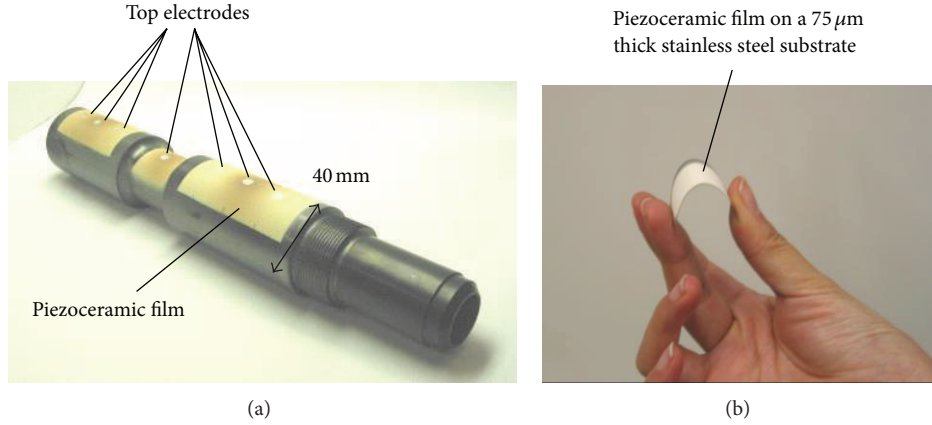


FIGURE 7: Examples of spray-on piezoelectric acoustic transducers: (a) IUTs and (b) an FUT.

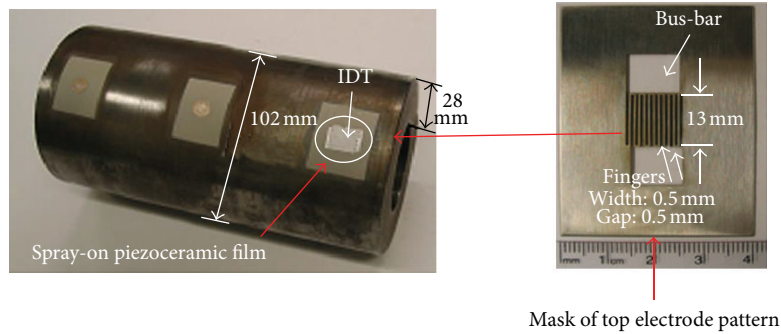


FIGURE 8: An interdigital transducer fabricated on a steel pipe (left) for generation and detection of Rayleigh surface acoustic waves. The interdigital top electrodes were silver-painted with help of a mask (right).

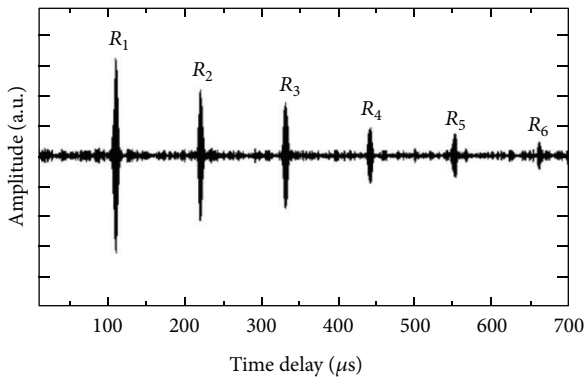


FIGURE 9: Rayleigh surface acoustic wave signal generated and detected with the IDT shown in Figure 8 at 150°C.

in aircraft component can be found in [7]. Wedge based wave tuning has, however, several drawbacks. First, the phase velocity c_w must be smaller than c_{phase} . This can limit either the choices of wedge materials appropriate for generation of a desired mode or the availability of modes that can be generated with a given wedge material. Secondly, spurious signals, resulting from wave reverberation inside the wedge, may deteriorate the quality of the useful signal, that

is, intended applied wave. Thirdly, due to beam spreading of acoustic waves propagating through the wedge to the structure surface, other wave modes beyond the mode of interest may be generated. Furthermore, if a fixed-angle wedge is used, the efficiency of wave tuning can be affected by temperature, due to temperature dependence of wave velocities. A variable angle beam wedge can be used to cope with temperature variation or to tune wave generation to a different mode by adjusting the incident angle, as presented in Figure 4. However, in this case, an extra block introduced in the wedge is needed, which not only reduces the wave energy transferred to the structure but also creates additional wave reverberation noise.

2.3. Tuned Wave Excitation and Detection with Piezoelectric Wafers. Piezoelectric wafer active sensors (PWASs) made of lead zirconate titanate (PZT) and bonded onto a plate substrate have been studied theoretically and experimentally for the generation of and detection of acoustic waves. Compared with conventional ultrasound transducers, which generate and detect out-of-plane particle displacement at the transducer/structure interface, the PWAS is able to generate and detect both out-of-plane and in-plane particle displacements through thickness-wise piezoelectric coupling (d_{33}) and lateral piezoelectric coupling (d_{31}). If the wafer thickness

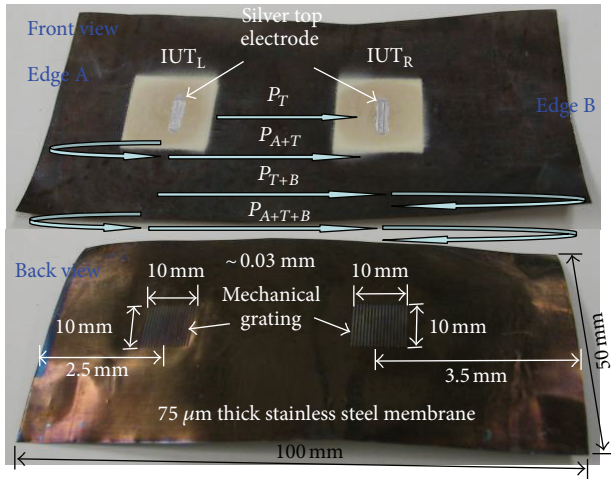


FIGURE 10: Two $62\ \mu\text{m}$ thick piezoceramic films are sprayed onto a $75\text{-}\mu\text{m}$ thick stainless steel (SS) membrane to form two IUTs (upper pane). On the other side of the membrane and opposing each IUT, a grooved grating is made with electrical discharge machining (EDM) (lower pane). Each grating is composed of seventeen $0.3\ \text{mm}$ wide, $\sim 0.03\ \text{mm}$ deep, $10\ \text{mm}$ long, and $0.6\ \text{mm}$ equidistant grooves.

is much smaller than its lateral dimensions, the fundamental thickness-wise resonance frequency will be much higher than lateral resonant frequencies to an order equivalent to the ratio of lateral dimensions to the thickness of the piezoelectric wafer. Wave generation and detection are much more efficient when the PWAS is excited at one of its natural resonant frequencies. It happens that the most exploitable Lamb wave modes, in terms of easier excitation and detection, are the S_0 and A_0 modes in the frequency range of hundreds of kHz. Also, in this frequency range, the coexistence and potential interference of propagating multiple higher order modes are avoided, resulting in simplified wave propagation, detection, and interpretation (of the corresponding sensor signals). Waves in this frequency range can be fairly easily generated and detected by PWASs of adequate sizes and PZT material and excited at or near one of their lateral resonant frequencies. In this configuration, the d_{31} piezoelectric coupling is essential for an efficient generation and detection of S_0 and A_0 Lamb wave modes in a plate. Thickness-wise piezoelectric coupling is far less efficient for this purpose due to much higher thickness-wise resonant frequencies and also due to the fact that by using a planar d_{31} effect, a more uniform direction-wise excitation and sensing capability are obtained.

It has been shown that the mode of wave motion inside a plate structure can be tuned by properly selecting the dimensions of the wafer and the excitation signal frequency and by taking into consideration the plate thickness and constituent material [8]. For example, if a square PWAS is used, efficient excitation of a particular mode of Lamb wave may be achieved if the length of the PWAS is half the wavelength of that wave at the excitation frequency. However, this excitation could still not be optimal, because this excitation frequency may not match a lateral resonant frequency of the PWAS due to different wave speeds in

the wafer and in the substrate being inspected. This means that further frequency tuning (and more careful selection of PWAS material and dimensions) would be needed to achieve optimal excitation efficiency. The excitation efficiency is also affected by the bonding quality and the ratio of the stiffness of PWAS to that of the substrate at the excitation frequency. Maximum energy is transferred from PWAS to the structure and vice versa when the stiffness of PWAS matches that of the substrate [9]. Since the stiffness of a plate is proportional to its thickness, both of the thickness of PWAS and that of the substrate affect the efficiency of energy transfer. To enhance the generation of a specific mode even further, two identical PWASs may be bonded vis-à-vis onto the upper and lower surfaces of the substrate. If they are excited electrically in phase, symmetric modes will be enhanced. If the two PWASs are excited electrically out of phase, anti-symmetric modes will be enhanced.

It is important to point out that efficient excitation of a wave mode does not guarantee effective detection of this mode, since this propagating wave mode may interfere and merge with other propagating modes that coexist in the structure, or it may be so dispersive in the excitation frequency range that the wave pattern arrived at the detector has largely widened, resulting in reduced spatial and time resolutions. To achieve optimal detection ability of a desired mode, it is important to follow the four guidelines set forth in Section 2.1. The detection ability may be further improved by carefully selecting the excitation frequency and the lateral dimensions of the transducer in such a way that favors excitation of a desired mode while suppressing the generation of undesired modes. For instance, when a square wafer is used, it may be possible to select an excitation frequency at which the length of the wafer is an odd multiple of the half wavelength of a desired mode and at the same time a multiple of the wavelength of an undesired mode [10].

2.4. Tuned Wave Excitation and Detection with Transducer Arrays. One other way of selectively generating and detecting a desired guided wave mode is to use an array of ultrasonic transducers. In Figure 5 an example of the application of a periodic array structure of piezoelectric polyvinylidene fluoride (PVDF) transducers and an array of piezoceramic transducers is presented [3]. As in the case of a square PWAS, under uniform loading and application/installation conditions (i.e., excitation and bonding), a wave mode is most efficiently excited when the array element width is as close as possible to $1/2$ of the wavelength λ of the guided wave propagating in the structure. The wave generation efficiency is further enhanced via promoting constructive interference of waves generated by all the elements when the array element spacing d is equal to λ for the excitation of waves propagating in the direction of the array. As pointed out by the authors in [3], the PVDF array has the merits of being thin, flexible, and thus convenient for conformal mounting or embedded applications. The cost of PVDF transducers is usually much lower than that of PZT transducers. On the downside, PVDF has much weaker piezoelectric strength than PZT and its lowest operation temperature (about -30°C) may be too high

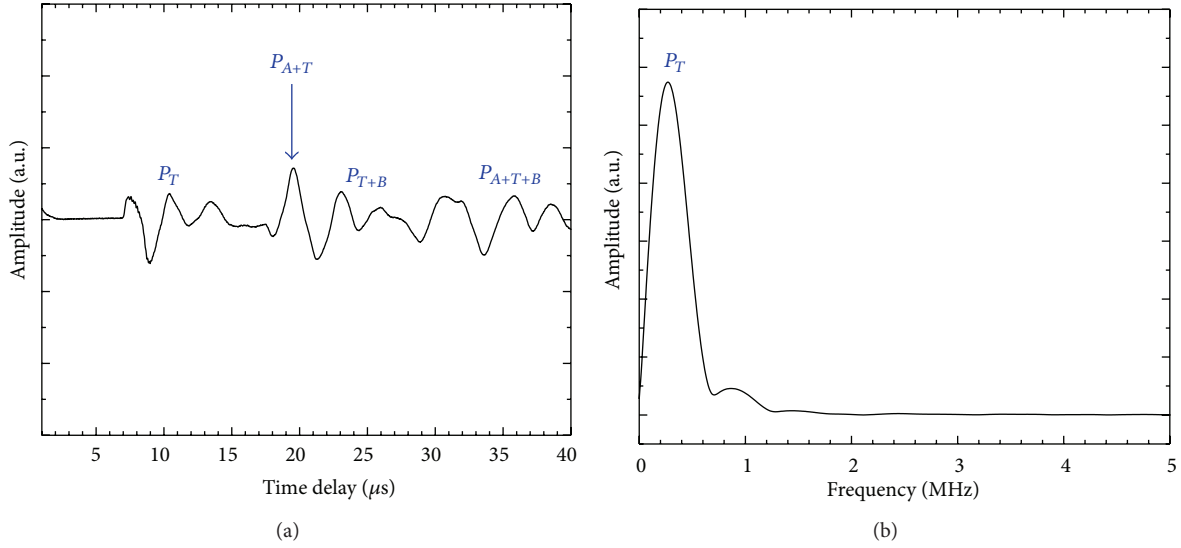


FIGURE 11: Ultrasonic performance of the IUTs shown in Figure 10 and operated in transmission mode. A 10-groove grating area was covered by the silver top electrode. (a) Signal in time domain and (b) spectrum of echo signal P_T .

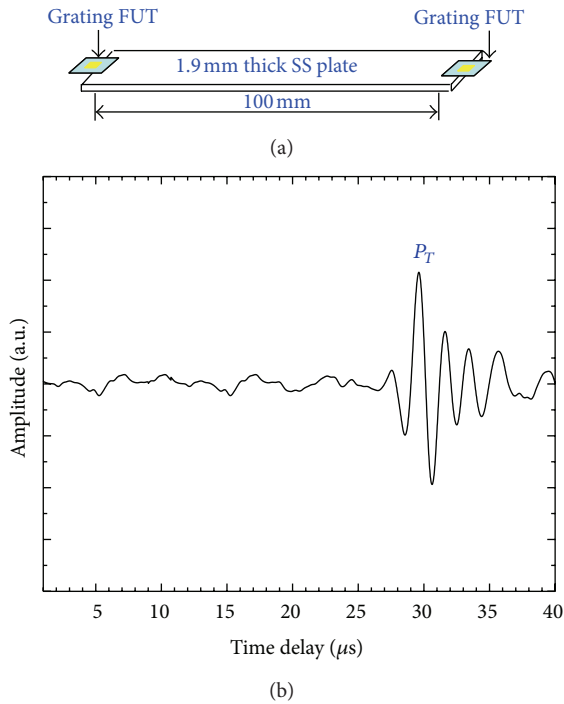


FIGURE 12: (a) Flexible grating transducers shown in Figure 10 are bonded at two ends of a 1.9 mm thick stainless steel plate. (b) Ultrasonic performance obtained by operating the two grating transducers in transmission mode.

for an application to aircraft SHM. It is important to point out that the piezoceramic transducer array in the figure was designed for pipeline monitoring, where the transducer array was pressed onto the outer surface of the pipe to realize better contact between transducers and the concerned structure.



FIGURE 13: Integrated ultrasound transducer deposited onto one end edge of an aluminum plate, for generation and detection of symmetrical plate acoustic waves (PAW).

For aircraft SHM, one can bond onto aircraft structures an array of low profile piezoceramic transducers.

2.5. Tuned Wave Excitation and Detection with Phased Arrays.

Wave mode tuning can be achieved by using a tuned wave phased array [12]. The array elements can be piezoelectric PZT, PVDF, or other types of acoustic transducers. The first step in constructing a tuned wave phased array would be to decide on the desired wave mode to apply and therefore on the type and dimensions of array elements and excitation frequency that would favor the generation and detection of the wave mode selected. In a simple tuned wave phased array, the array elements are mounted equidistantly onto the thin-wall structure to inspect, in the direction of wave propagation, as shown in Figure 6. For illustration purpose only four elements are used for the transmitting and receiving arrays. For a tuned phased array configuration for the excitation of a particular wave mode at a selected frequency, the time interval ($\Delta\tau$), or phase shift, in between the activation of consecutive elements in the array for the generation of the tuned wave mode is determined according to the frequency of the wave mode to apply, its propagation velocity, and wavelength (according to the dispersion relations explained previously). Let d be the array element spacing, defined to be equal to the wavelength (λ) of the wave mode to apply in an optimized configuration, according to the (excitation)

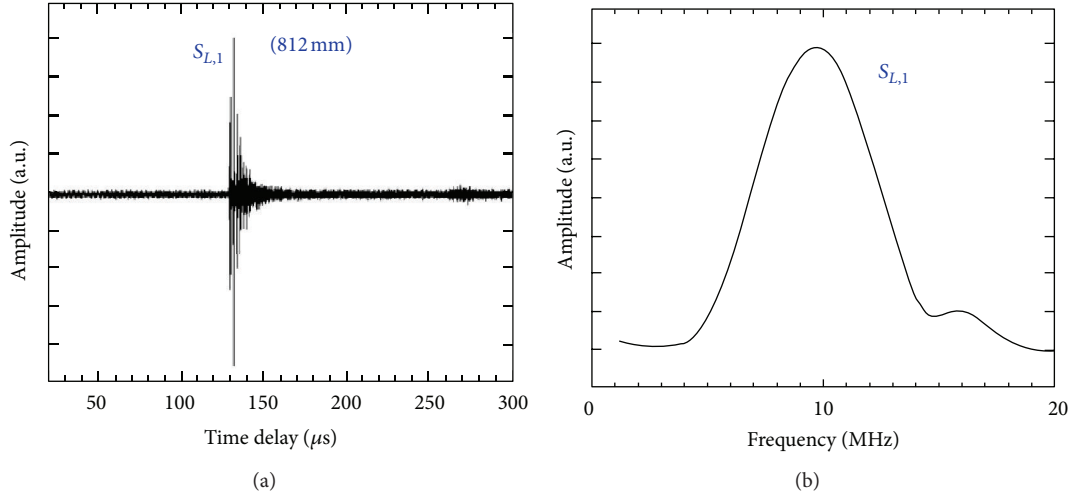


FIGURE 14: Measured reflected symmetrical PAW mode echoes from the edge opposite to the IUT (experiment performed with environment temperature of 150°C) in (a) time and (b) frequency domains.

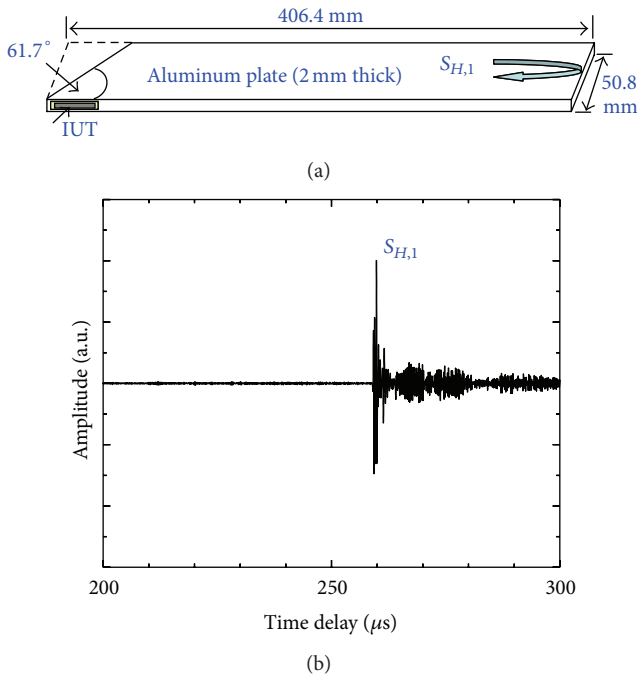


FIGURE 15: Schematic diagram of an IUT fabricated directly onto the side edge of a 2 mm thick aluminum plate to generate and detect SH PAWs (a) and a received echo signal (b).

frequency selected (f) and the phase velocity (c_{phase}) of a selected mode in the structure, $\Delta\tau$ is determined as the time of flight for the wave front of the selected mode to travel a distance d in the structure

$$\Delta\tau = \frac{d}{c_{\text{phase}}} \left(= \frac{\lambda}{c_{\text{phase}}} = \frac{1}{f} \right). \quad (2)$$

Array elements 1, 2, 3, and 4 are excited sequentially with excitation pulses to elements 2, 3, and 4 being delayed by $\Delta\tau$,



FIGURE 16: Integrated longitudinal wave ultrasound transducer (LUT) for the generation and detection of antisymmetrical PAWs using mode conversion.

$2\Delta\tau$, and $3\Delta\tau$ respectively with respect to the excitation pulse applied to element 1. This ensures constructive interference of waves excited at all the elements, with these waves travelling towards the receiving array with a phase velocity c_{phase} . At the receiving array, the waves will be sensed and the corresponding sensor signal will be given by elements 5, 6, 7, and 8. The signals given by sensors 5, 6, and 7 will be delayed by $3\Delta\tau$, $2\Delta\tau$, and $\Delta\tau$, respectively, with respect to the time at which the propagating wave was sensed by element 5 and then added to the signal received by element 8. This enables the constructive interference of the signals of the different sensing elements and hence further enhances the sensitivity of the array to the propagating selected wave mode. The most significant advantage of phased array wave tuning is the capability of tuning to any desired mode (departing, however, from an optimized array since the sensor dimensions may not be optimized for inspection at the selected mode and frequency) by adjusting time delays and excitation frequency without changing the layout of array elements. This makes automatic tuning possible to compensate for temperature variation or to cope with situations where precise velocity dispersion curves are not available. The downside is the need for more sophisticated electronics than other wave tuning methods.

For selective directional generation and detection of acoustic waves, array elements can be arranged in a line, a circle, or forming a two-dimensional pattern to achieve a desired directivity pattern [15]. For example, an embedded

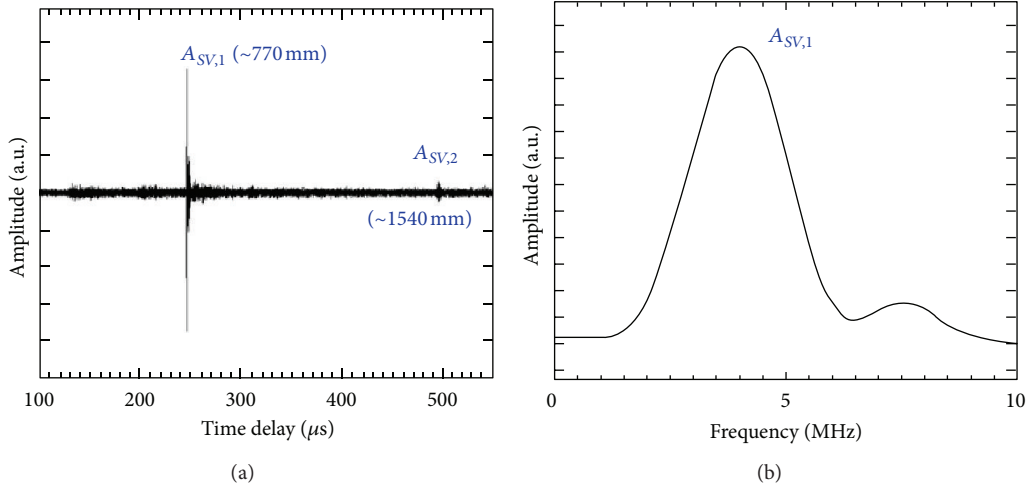


FIGURE 17: Measured anti-symmetrical PAWs reflected from the edge opposite to the IUT (experiment performed at 150°C). (a) Time domain signal and (b) frequency spectrum of the 1st round trip echo signal.

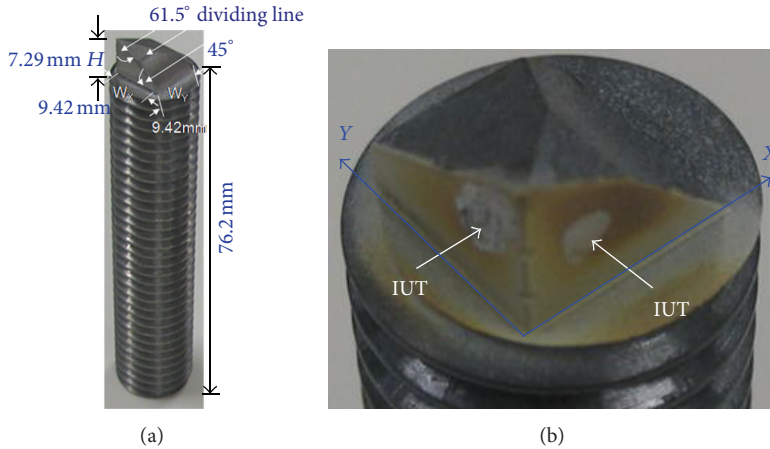


FIGURE 18: (a) An integrated probe which can generate and receive longitudinal and two orthogonal shear waves. (b) Probe head having two IUTs.

phased array can be formed by using a plurality of PWASs to scan a planar thin-wall structure in a similar way to conventional ultrasonic phased array system [16], using in the former case guided acoustic waves. By using a phased array, guided acoustic waves can also be focused to a point in a non-planar structure, for instance, a pipe, resulting in an improved flaw detectability [17].

2.6. Wave Excitation and Detection with Sol-Gel Based Piezoceramic Transducers. A sol-gel based process has been applied to the fabrication of piezoelectric acoustic transducers [18, 19]. A key feature in this process is the spray of a piezoceramic powder solution directly onto a substrate on which to make the transducer. This means that piezoelectric transducers could be conveniently fabricated on curved surfaces as integrated ultrasound transducers (IUTs). The process also allows fabricating flexible transducers by spraying the piezoceramic powder solution onto a thin metallic

foil. The flexible ultrasound transducers (FUTs) can then be bonded onto a structure to be evaluated. An array can be formed by depositing a plurality of top electrodes directly on the piezoceramic film. Figure 7 shows two examples. Depending on the piezoceramic power used, the transducer can work at temperatures up to 200°C or up to 500°C. On the lower temperature side, the transducers have been tested working at -60°C in an environmental chamber.

On a microscopic level, what differentiates the sol-gel based spray-on piezoceramic transducers from conventional PZT transducers is the much higher porosity of the former. This porosity endows a spray-on ceramic film with a certain degree of flexibility, illustrated in Figure 7, and allows the spray-on type transducers to be conformally mounted onto a base structure and, as a result, to be able to sustain much higher external stresses than conventional PZT transducers without cracking. This porosity also provides a unique acoustic characteristic to sol-gel based piezoceramic acoustic transducers; that is, they are highly efficient wideband longitudinal

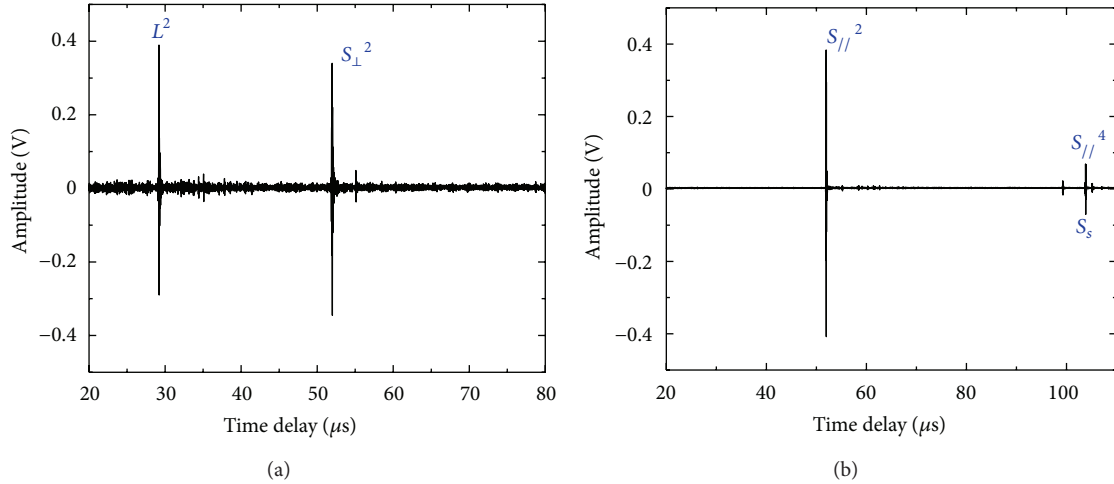


FIGURE 19: (a) Longitudinal wave echo signal (L) and shear wave echo signal (S_{\perp}), reflected from the probe’s end. Waves generated and received by one IUT; (b) shear wave echo signal (S_{\parallel}), reflected from the probe’s end. Waves generated and received by the other IUT. Superscripts 2 and 4 designate the first and second round trip waves, respectively.

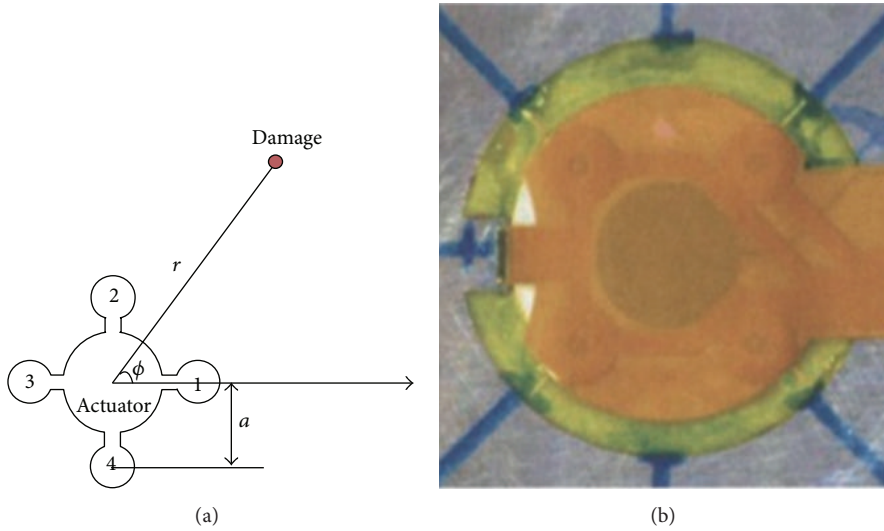


FIGURE 20: An SHM transducer node. (a) Schematic design; (b) packaged prototype.

wave transducers but not efficient in generating in-plane wave motions. A performance comparison study was completed between sol-gel based piezoceramic transducers and conventional PZT transducers [22]. It was found that for bulk wave generation and detection, sol-gel based transducers produce cleaner signals and generate much less crosstalk and therefore are better suited for applications where ultrasound transducer networks or bulk wave diagnostic signals with high signal-to-noise ratio (SNR) are required. Conventional PZT acoustic transducers are able to generate much stronger plate acoustic waves and therefore are better suited for applications where plate acoustic waves are used.

Sol-gel based acoustic transducers can be installed into the structures to inspect in several different ways. In Figure 8, a piezoceramic layer was first deposited onto a steel tube with 102 mm outer and 46 mm inner diameters. Then, a pair

of interdigital colloidal silver electrodes were painted on the piezoceramic layer with help of a stainless steel (SS) mask to form an interdigital transducer (IDT). The width of and the gaps between the electrode fingers were designed in such a way that favored the generation and detection of Rayleigh surface acoustic waves through constructive interference, in a similar way presented in Section 2.4. In Figure 9, the sensed waves by the transducer are presented, when such waves were generated by the same transducer in an experiment with an environment temperature of 150°C. In the figure, R_n , with $n = 1, 2, \dots, 6$, indicates the n th round trip echo signal around the cylindrical surface of the tube. The center frequency, 6 dB bandwidth, and SNR of the first round trip echo signal were 1.5 MHz, 0.3 MHz, and 24 dB, respectively [24].

Guided acoustic waves in a plate can also be generated by introducing line shaped mechanical gratings on the side of

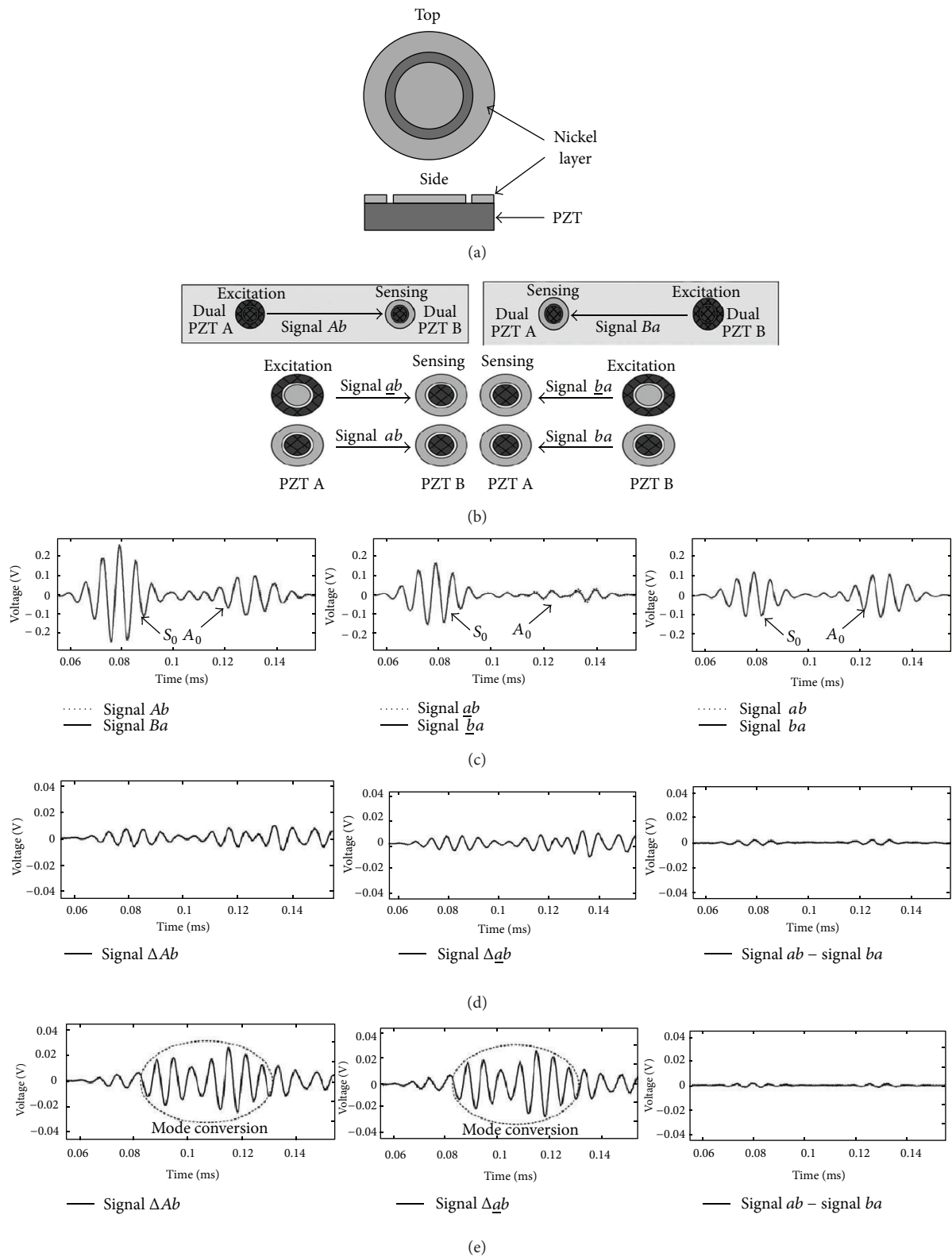


FIGURE 21: Sensing design using dual PZT transducers. (a) A schematic drawing of a dual PZT transducer; (b) different excitation and sensing combinations; (c) signals measured with sensing configurations illustrated in (b); (d) difference between signal pairs in each of the panes of (c); (e) corresponding signal differences of those illustrated in the panes of (d) but with introduction of a notch in the plate.

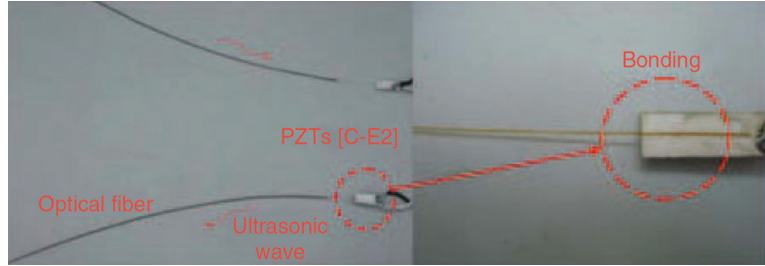


FIGURE 22: Construction of an ultrasonic active fiber sensor [11].

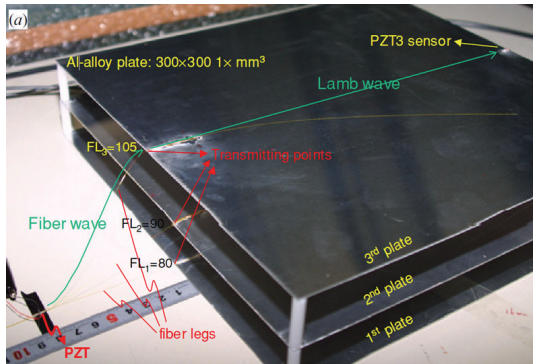


FIGURE 23: Experimental setup for ultrasonic transmission using a fiber wave PZT transducer (FL = fiber length between the PZT in the fiber wave PZT transducer and the remote transmitting point in mm). Three transmission paths, each in an individual plate, were explored simultaneously [13].

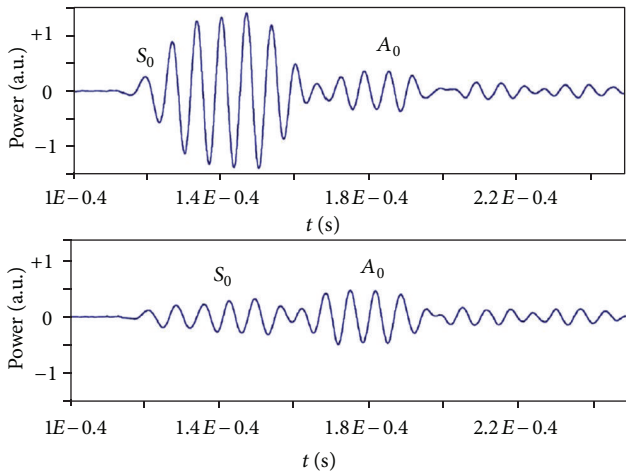


FIGURE 24: Lamb wave signals obtained by the polarimetric method for different polarizer orientations: top -10° to the plane of the plate and bottom -60° orientation [14].

the plate and exciting these gratings acoustically with a spray-on piezoceramic integrated ultrasound transducer (IUT), deposited on the opposite side of the panel with respect to the grating. This approach has been adopted for fabrication of two flexible guided wave transducers, shown in Figure 10 [26]. The width of the top electrodes is used to control the size

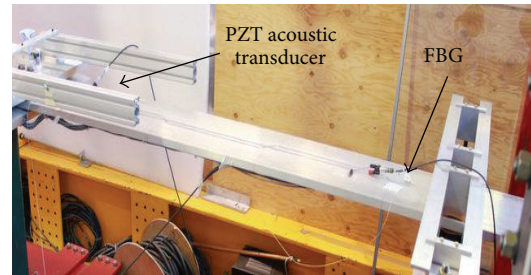


FIGURE 25: Generation and detection of acoustic waves in a 25.4 mm thick aluminum beam.

of active piezoelectric area. The IUTs operate predominantly in their thickness resonance mode. The gratings either convert longitudinal waves to plate acoustic waves or vice versa. In Figure 11, the signals obtained from IUT_R are presented, where sensing waves were excited by IUT_L . Different wave propagation paths are illustrated in Figure 10, corresponding to the different signal arrivals depicted in Figure 11. It is important to point out the difference between the 15 MHz center frequency of the excited longitudinal waves by IUT_L and the much lower center frequency of about 300 kHz of the plate acoustic waves received at IUT_R .

The two grating transducers shown in Figure 10 were then separated and bonded at two ends of a 1.9 mm thick, 100 mm long, and 50 mm wide SS plate, as shown in Figure 12(a). The ultrasonic signal obtained in transmission mode is shown in Figure 12(b). The signal-to-noise ratio (SNR) of the received signal was 20 dB.

In Figure 13, an IUT was fabricated onto one end edge of a 6.35 mm thick aluminum plate to generate and detect predominantly symmetrical Lamb wave modes. The signal reflected from the opposite end of the plate with respect to the transducer location and its frequency spectrum is shown in Figure 14 [24]. The center frequency of the signal was about 10 MHz, resulting in a frequency-thickness product value of 63.5 MHz mm. By referring to Figure 1, one will see that a plurality of modes could be generated. This is indeed the case as manifested by the rather complex detected waveform.

In Figure 15, a set-up configuration to generate and detect shear horizontal plate acoustic waves (SH PAWs), with help of mode conversion, is illustrated. An IUT is deposited at the side edge near the end of a 2 mm thick aluminum plate with a length of 406.4 mm and a width of 50.8 mm. The thickness of

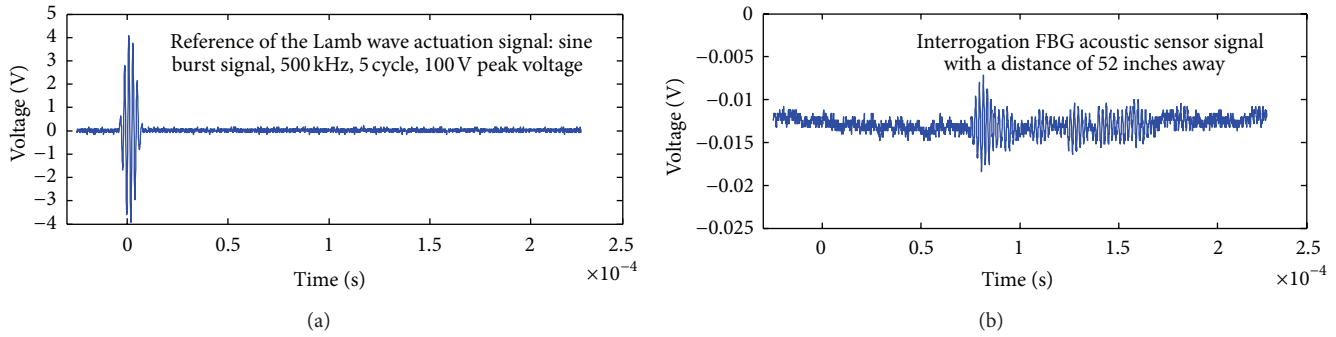


FIGURE 26: FBG response to acoustic wave excitation by a PZT transducer.

the IUT piezoceramic layer was $90\ \mu\text{m}$. The top rectangular electrode was 20 mm long and 1.6 mm wide, defining the IUT active area. Symmetrical PAW modes are first generated by the IUT and travel nearly 25.4 mm to the oblique edge, depicted in the figure, where they are converted to SH PAWs. The SH PAWs propagate then to the straight end of the plate and are reflected back to the oblique edge where they are back converted to symmetrical PAWs, which are captured by the same IUT. For this configuration the chosen mode conversion angle is 61.7° . This value was obtained by using Snell's law based on measured extension mode velocity and the shear wave velocity in the plate [29].

Longitudinal to shear mode conversion and vice versa can also be applied to generate and detect predominantly anti-symmetric PAWs. In Figure 16, a set-up configuration to achieve such mode conversion is demonstrated. An aluminum plate, 6.35 mm thick, has one of its end edge obliquely cut to form a 64.6° angle between the end edge surface and the plate upper surface. This angle was calculated using Snell's law, according to the longitudinal and shear wave velocities in the plate material. At this angle, the energy conversion ratio from longitudinal waves to shear waves is 75.1%, which is only 0.06% smaller than the maximum conversion ratio. Longitudinal wave ultrasound transducers, denoted by LUT in the figure, were fabricated onto the upper plate surface to its very end, above the oblique edge, by using the sol-gel spray technique. Acoustic waves generated by the LUT hit the oblique edge and are then mode converted to shear vertical vibrations, with the resulting boundary reflected waves propagating in a direction towards the other end of the plate. Shear vertical vibrations at the oblique edge are forced predominantly to anti-symmetric Lamb waves that propagate in the plate to its other end and then are reflected back to the oblique edge, where they are mode converted back to longitudinal waves and then captured by the LUT. In Figure 17, the signal from LUT is presented, for an experiment performed at a temperature of 150°C . The 1st and 2nd round trip signals, denoted by $A_{SV,1}$ and $A_{SV,2}$, can be observed in the graph. The frequency spectrum of the 1st round trip echo is also shown in the figure. The 3.9 MHz center frequency of this signal results in a frequency thickness product of 14.2 MHz-mm at which a plurality of anti-symmetrical modes are generated and propagate in co-existence in the plate [24].

Owing to the low footprint of sol-gel based acoustic transducers, it is possible to make a probe that generates longitudinal and shear waves simultaneously through mode conversion. The probe design shown in Figure 18 is able to generate a longitudinal wave and two orthogonal shear waves, simultaneously, through the use of two IUTs deposited on the probe head [31]. In Figure 19, the signals corresponding to the sensed waves (generated by the same probe and transducers) are presented. Simultaneous information of longitudinal and orthogonal shear waves' velocities can be used for the characterization of the substrate material (for example, to determine residual stresses).

2.7. Other Multielement Wave Excitation and Detection Methods. Multiple elements can be built into a single unit. Kessler and Raghavan [32], at Metis Design Corporation (MDC), patented an SHM transducer node design composed of a PZT actuator at the center and four PZT sensors equidistantly distributed in a circle, around the center actuator, as shown in Figure 20 [32]. It is claimed that through the use of this transducer node design, it is possible to determine with good accuracy a damage location, with a single node. The accuracy of this node to damage localization is limited, however, by its size.

A common SHM practice for damage detection is to compare the currently gathered data with "baseline data" previously obtained when the structure was in a pristine state or a reference condition. With the objective of detecting newer and/or developing damages, the reference condition may correspond to a structure with existing damages, which were previously detected, located, and well characterized. Strictly speaking, this approach is valid only if the performance of the sensors and associated systems remains unchanged over time. In practice, this is rarely true due to the effects of many factors on the sensors and electronics. These factors include temperature, pressure, humidity, corrosion, UV radiation, structure load, material degradation, debonding of sensors from the structure, and variation in wiring conditions. Approaches which are capable of damage identification, localization, and assessment, without the need of baseline data, and in which the effects mentioned previously in the acquired data are minimized, are deemed to be more reliable and are highly

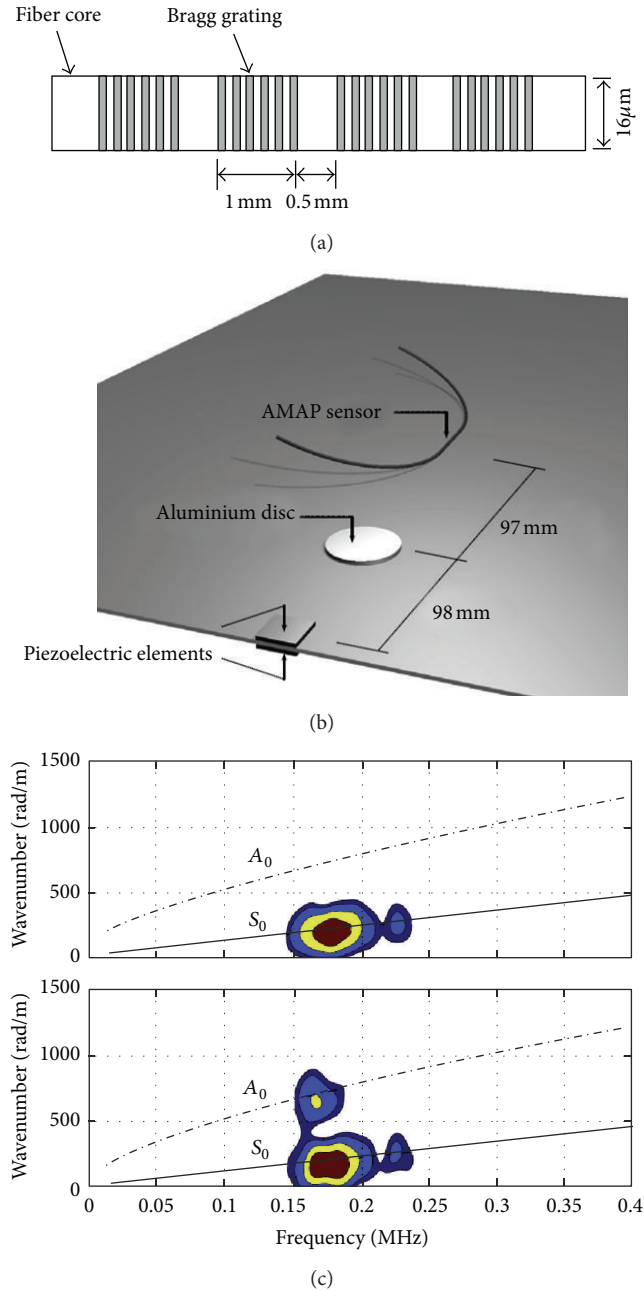


FIGURE 27: AMAP sensor demonstration. (a) Key dimensions in a section of the optical fiber core in the AMAP sensor; (b) test panel made of an aluminum alloy with the wave generation element, AMAP sensor, and bonded disc, attached to simulate a damage, as a source of reflected waves; (c) spectral decomposition of the AMAP sensor response measured for a selectively excited S_0 mode in the absence of the bonded disc (top) and after attachment of the disc (bottom) [20].

sought after. A dual PZT transducer sensing design has been proposed as a response to the need for reference-free crack detection methodologies [33]. In Figure 21(a), a schematic drawing of a dual PZT transducer is presented. One pair of such transducers is used according to six different excitation and sensing combinations, with respect to the use of the

outer ring of the transducers (configuration denoted by a and b , respectively, for the first and second transducer), the inner disc of the transducers (denoted by \underline{a} and \underline{b}), and by the use of both of the inner and outer regions of the transducers simultaneously (configuration denoted by A and B). These six excitation and sensing configurations are depicted in Figure 21(b), and the signals, obtained for each configuration, are presented in Figure 21(c), for a 122 cm \times 122 cm \times 0.6 cm aluminum plate without defects. With these signals, the differences between corresponding propagation and counter-propagation signal pairs can be calculated, for example, for the signal pair Ab and Ba indicated in the upper two panes of Figure 21(b). These calculated differences are depicted in Figure 21(d). In Figure 21(e), the signal differences corresponding to the ones illustrated in the panes of Figure 21(d) are displayed for the same aluminum plate but now with an introduced 0.15 cm deep \times 0.10 cm wide \times 6 cm long notch. The comparison between the corresponding signals in Figure 21(d) and Figure 21(e) shows that the signal differences are noticeably larger in the presence of the notch. The larger differences are believed to result from the mode conversion from S_0 mode to A_0 mode and vice versa due to the presence of the notch. The differences of the three signal pairs are used in a damage classifier method proposed by the authors to assess the damage. It should be pointed out that the proposed method assumes no mode conversion when there is no crack in the structure, that is, for a pristine structural condition. This may not be true for composite structures or for structures with more complicated geometries, with joining elements (such as fasteners and rivets) and with different boundary conditions than the plate in which this method was investigated by the authors. However, the proposed technique still has its merit in revealing defects which may not be detectable using a conventional single PZT element actuator/sensor pair.

2.8. Ultrasonic Active Fiber Sensor (UAFS) Based Pulse-Echo Method. Ultrasonic Active Fiber Sensor (UAFS) is simply a PZT acoustic transducer bonded to one end of an optical fiber, as depicted in Figure 22. The PZT transducer excites ultrasonic waves in an optical fiber, used as a wave guide, and captures ultrasonic waves reflected from the opposite end of the optical fiber or from a location in the fiber where a mechanical load is applied [11, 34]. This sensor has been used to locate the position of the application point of a mechanical load, detect liquid spills, monitor the cure of solder, and to measure the level of liquid in a reservoir. Research efforts were dedicated to demonstrate the applicability of the PZT coupled optical fiber, as a wave guide, to transmit, generate, and acquire Lamb waves propagating in a solid media. In particular, aluminum plates were used for such demonstration [13]. In this work, the optical fiber termination, opposed to the one attached to the PZT element working as a transducer, that is, either as actuator or sensing element, was bonded to the edge of the aluminum plate. Additionally, another PZT element was bonded to the opposite edge of the plate with respect to the location where the optical fiber termination was bonded. Subsequently, either of the

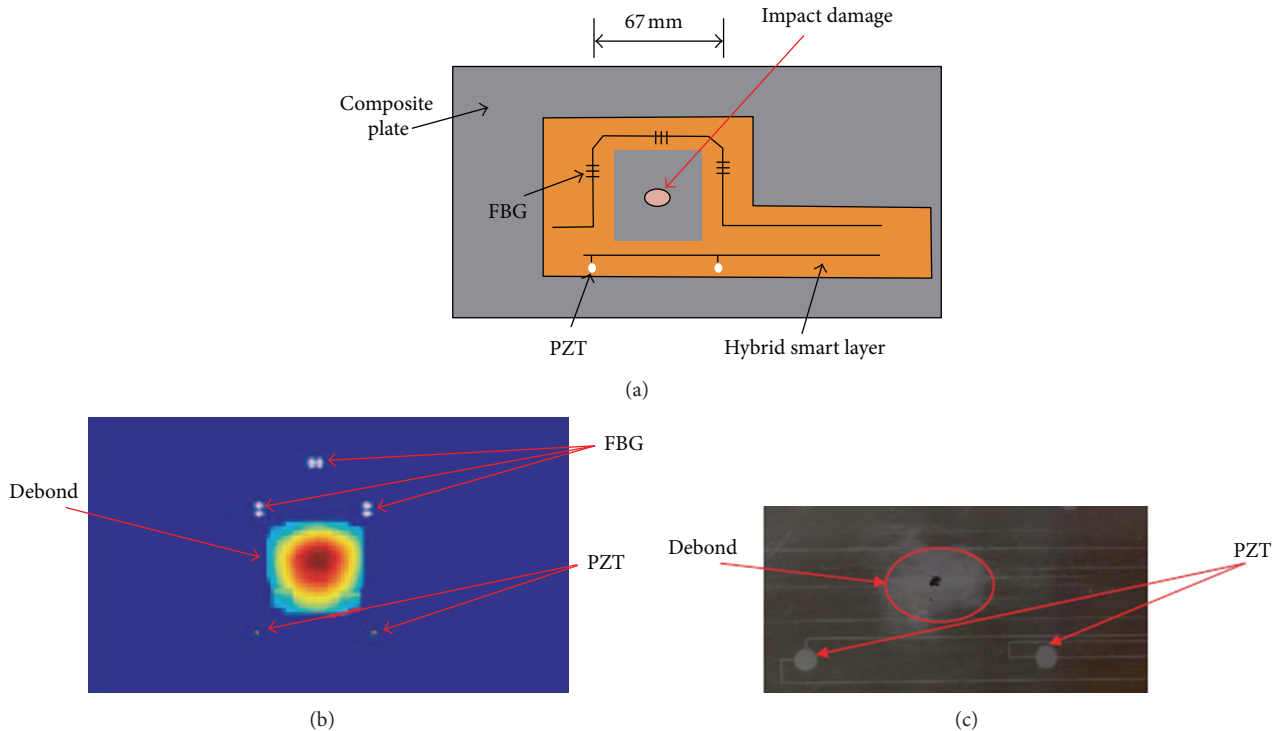


FIGURE 28: Hybrid sensor network used for damage detection. (a) Hybrid layer mounted on the surface of a composite panel; (b) diagnostic image of debond on the composite plate; (c) X-ray image of the damage [21].

PZT elements was excited while the other one was used as sensor (Figure 23). These experiments proved the capability of using the fiber wave piezoelectric transducer in a pitch-catch network configuration, with the optical fiber serving as a wave guide, to generate or sense Lamb waves propagating in the aluminum plate, with the subsequent possibility of using this transducer configuration for a damage detection system.

A main advantage of this sensor over other fiber optic sensors is its low cost, as only a common optical fiber used for telecommunications is needed, without any printed sensors. While it may not be suitable for certain embedded applications due to possibly considerable leakage of acoustic energy into the surrounding medium, this technique may be useful when embedding is not required and when the effect of bonding can be minimized or well characterized. The sensor may also be used for high temperature SHM by using the optical fiber to transfer diagnostic acoustic waves to a hot structure through a bonding layer, so that a direct contact of the PZT transducer with the hot structure is avoided. Depending on applications, the optical fiber can be replaced with wires/wave guides made of other materials.

3. Hybrid Approaches

3.1. Detection of Ultrasound Using Fiber Optic Sensors (FOSs).

The application of Fiber Optic Sensors (FOSs) offers certain advantages in comparison with the use of conventional PZT sensors in terms of the following: directional sensitivity; more broadband response; denser sensor multiplexing; immunity

to and not generating Electro-Magnetic Interference (EMI) and therefore showing good electromagnetic compatibility (EMC) with other on-board avionic systems; good mechanical and environmental durability; potential application in explosive environments, such as inside fuel tanks, possibly inside wetted structure, with minimal risk due to the fact that required sensor power and signal transmission is performed through light travelling in an optical fiber, possibly to remote locations, with the optical fibers replacing required electrical networks; and ease of embedment in composite materials without bulky wiring scheme. It has been shown that FOS can be sensitive to acoustic pressure (fiber polarimeters) or acoustic wave induced strain (using Fiber Bragg Grating (FBG) sensors) [14], and therefore, FOS can be used for detection of ultrasound. The combination of using PZT actuators for ultrasonic wave generation and FOS for diagnostic ultrasonic waves detection can be a powerful inspection tool for guided wave based SHM. Figure 24 shows that Lamb waves can be detected by using a polarimetric fiber optic sensor and that the sensitivity of the sensor to the fundamental symmetric mode (S_0) and the fundamental anti-symmetric mode (A_0) can be tuned by varying the polarizer orientation.

In a recent study, an FBG sensor was used to detect acoustic waves generated with a 6.35 mm diameter PZT acoustic transducer. The PZT transducer and the FBG sensor were 1.32 meters apart and both were bonded onto the upper surface of a 25.4 mm thick aluminum beam, as shown in Figure 25. The FBG sensor was able to detect acoustic waves generated by the PZT transducer at a distance of 1.32

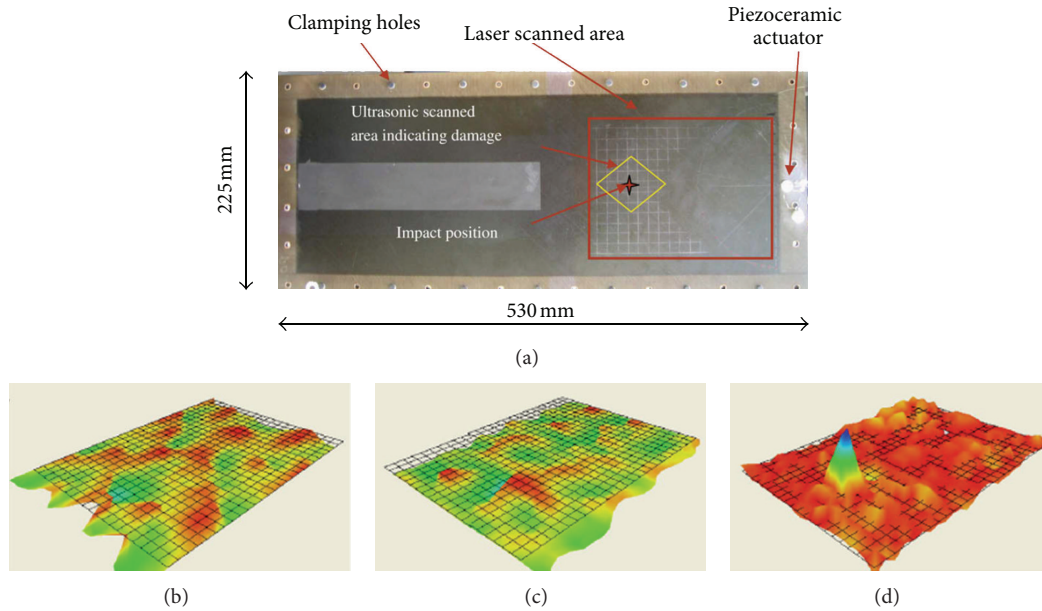


FIGURE 29: Combined use of piezoelectric actuator and laser vibrometer for SHM of aerospace composite structures. Composite plate and experimental setup used in active impact damage detection investigations (a) and Lamb wave amplitude in the in-plane x -direction (b), in the in-plane y -direction (c), and in the out-of-plane z -direction (d) [23].

meters from the FBG sensor, with the waves propagating in a relatively thick structural component, in comparison to the thin-wall members usually used for experimentation with guided acoustic waves. Figure 26 shows the excitation signal applied to the PZT transducer and the acoustic signal captured by the FBG sensor [35].

A distributed Bragg grating sensor array, termed acoustic mode assessment photonic (AMAP) sensor has been proposed in conjunction with the two-dimensional Fourier transform, to resolve the Lamb wave field both spatially and temporally. The method, as depicted in Figure 27, has shown its capability of the detection of structural damage by identifying acoustic wave mode conversion caused by the damage [20]. Mode conversion from S_0 to A_0 caused by the presence of an aluminum disc simulating damage, as an added discontinuity in mass and stiffness, can be clearly seen in Figure 27(c).

There are several possibilities to combine fiber optic sensors with piezoelectric actuators for guided wave based SHM. The following example shows a network configuration explored at Stanford University for damage detection in a composite laminate plate [21]. A main merit of a hybrid PZT/FBG system is the decoupling of actuator and sensor signals, whereas in an all-PZT actuating and sensing system the crosstalk between the actuation signals and sensor signals is an inherent problem particularly when highly integrated. As depicted in Figure 28, the applied system was successful in detecting, locating, and estimating the dimensions of an imposed impact resulting delamination in a composite material substrate, at the center of the sensor network. A pitch-catch based methodology was used, as well as a previously developed damage index method based on energy scattering of the waves' corresponding FBG sensor signal.

3.2. Wave Generation with Piezoelectric Actuator and Detection with Laser Vibrometer for SHM of Aerospace Composite Structures. In this method, a piezoelectric transducer is used as actuator to generate Lamb waves in a host material, such as in the carbon/epoxy composite plate depicted in Figure 29 [23]. Subsequently, a scanning 3D laser vibrometer is used to acquire Lamb wave responses from the analyzed plate and to monitor the propagation of the waves and the effect on such propagation of the interaction with existing damage. The damage introduced in the composite plate by an impact has been clearly detected by the laser vibrometer, through the out-of-plane (z -direction) vibration measurement. This technique has three attractive merits. First of all, a complicated sensor layout is not required. Secondly, it is easy to apply without the need of sophisticated signal processing and wave analysis. Finally, and importantly, it does not need any baseline data as reference.

3.3. Ultrasonic Wave Generation with Laser and Wave Detection with Piezoelectric Sensor. In this technique, a laser is used for the excitation of the waves and a piezoelectric element is used as a sensor, in opposition to the technique presented in Section 3.2. The present technique uses a laser, with the help of a rotation stage, as depicted in Figure 30(a) [36], or a mirror scanner, as presented in Figure 30(b) [37], to excite, point after point, the entire surface of a structure, and uses the piezoelectric element to sense the laser induced ultrasonic waves propagating in the host material being scanned. Subsequently, all the traces of signals obtained from the piezoelectric sensor are combined to obtain a sequence of images showing the propagation of the waves in the structure, as depicted in Figure 30(c) [38]. In Figure 30(d),

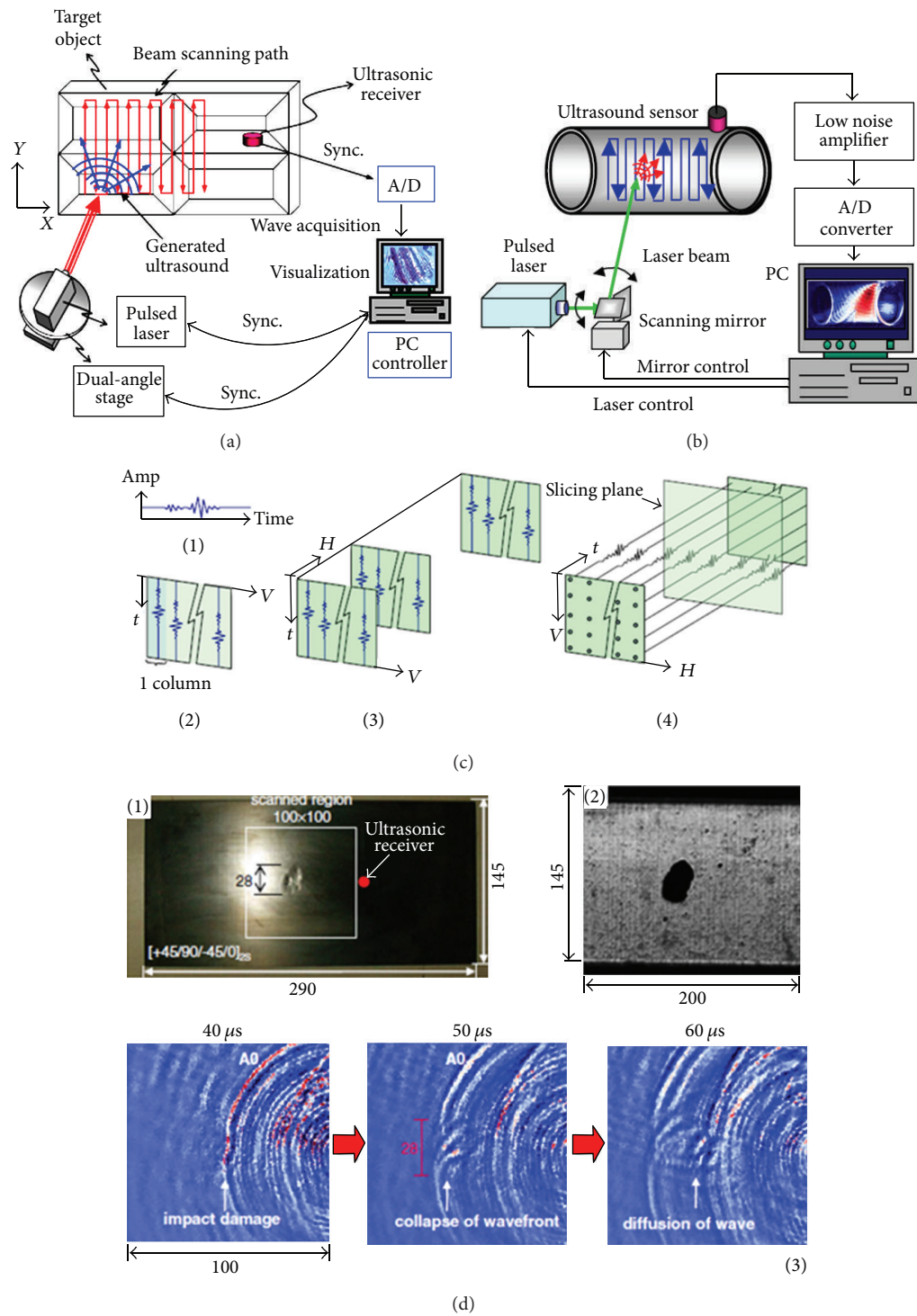


FIGURE 30: Application of a laser for ultrasonic wave generation and of a piezoelectric sensor for ultrasonic wave detection. (a) Laser ultrasonic visualization system using a dual-angle stage for scanning; (b) laser ultrasonic visualization system using a scanning mirror; (c) illustration of an image construction process: (1) one ultrasonic signal saved, (2) matrix data structure for one vertical scan, (3) raw matrix data structure for the different vertical scans, and (4) data manipulated to fit the shown structure and sliced along the time axis; (d) application example for damage detection: (1) Hammer-struck damage on a CFRP skin, (2) C-scan image, and (3) wave field propagation snapshots in the vicinity of the impact damage (dimensions in mm).

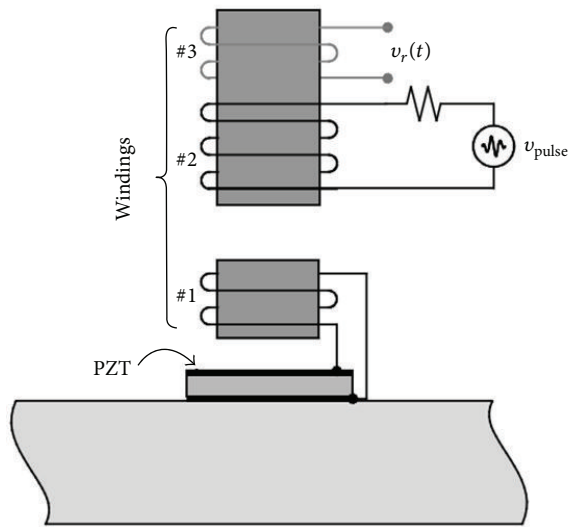


FIGURE 31: Inductively coupled PZT transducer [25].

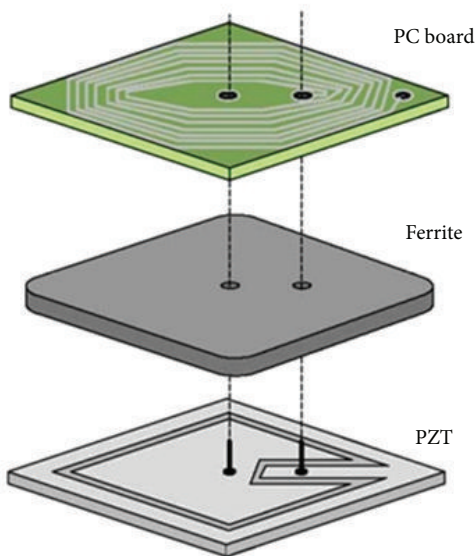


FIGURE 32: A planar transducer design using a coil on a printed circuit board [25].

an example of the application of this technique for damage detection is presented [36]. The technique has been applied to composite aircraft debonding visualization. The inspection showed that the location, shape, and size of the poor bonding defect, artificial stringer tip debonding, and real skin-spar debonding could be visualized and/or measured from the imaging results [39]. This hybrid approach has been adopted by other researchers [40, 41] and particularly for high temperature applications [42]. In comparison with the technique presented in Section 3.2, the current technique may present some advantages when inspecting a complex structure where it is difficult to use a piezoelectric actuator to generate detectable, strong, and diagnostic ultrasonic waves propagating through the entire structural component. By

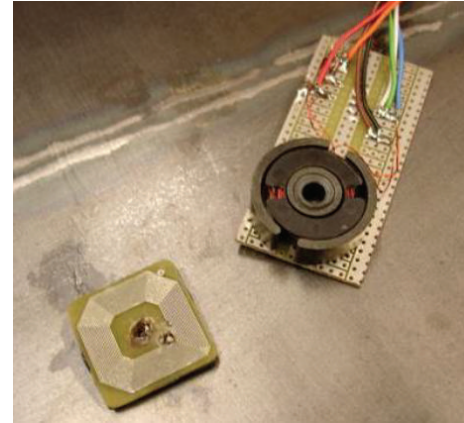


FIGURE 33: A prototype planar transducer based on the design in Figure 32 (lower left) and a pulse generation and detection probe (upper right). The PZT was 1 mm thick and 25 mm square, and the ferrite sheet was 1 mm in thickness and 26 mm square [27].

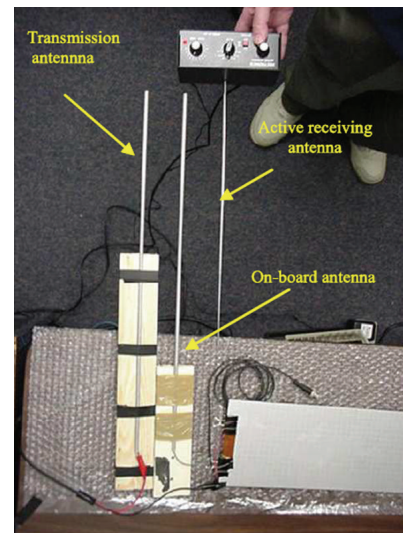


FIGURE 34: A wireless test setup [28].

utilizing a laser as an actuation element in the way adopted by the present technique, unlike in the selective (or tuned) mode generation of ultrasound with a piezoelectric actuator, different wave modes will unavoidably be generated in the structure. This will increase the complexity of required signal processing and data interpretation. The selection and analysis of a particular wave mode at a preferred frequency among a plurality of wave modes and frequencies in dispersive modes generated by the laser type actuation, can be tackled through wavelet transformation [43], or through analysis in the frequency-wavenumber domain [44]. One other aspect that must be taken in to account is that an ultrasonic wave generation laser usually uses powerful short laser pulses for wave generation. The applied laser beam may be detrimental to the structure, as studied by Hong et al. [45] among others.

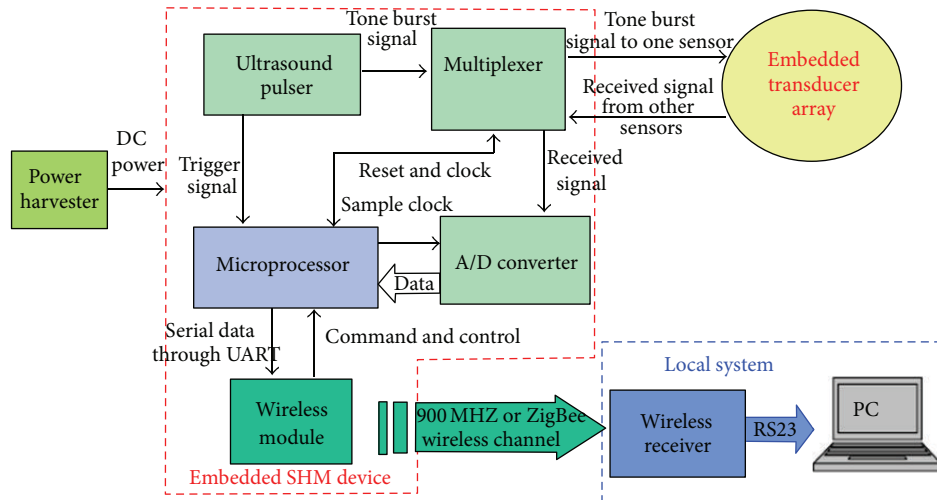


FIGURE 35: Diagram of the embedded ultrasonic structural health monitoring system [28].

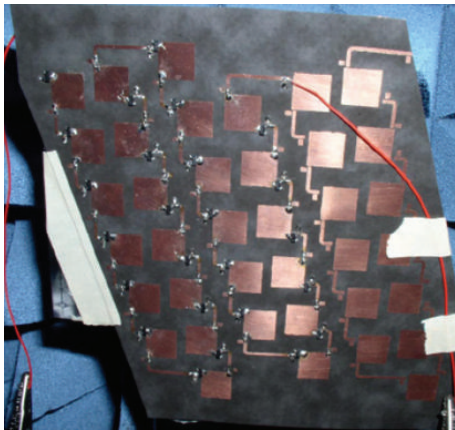


FIGURE 36: The 10 GHz 25-element microwave rectenna array for wireless powering of on-board electronics [28].

4. Wireless Excitation and Detection Techniques

The present section reviews four noncontact wave generation and detection techniques that involve the use of piezoelectric acoustic transducers. These techniques aim to explore and achieve the benefits of wireless piezoelectric (mechanical) based acoustic wave actuation and sensing. These simulate the advantages presented by other noncontact transducers for acoustic wave excitation and sensing, such as electromagnetic acoustic transducers (EMATs), which base acoustic wave generation and sensing on eddy currents and electric and magnetic field conversion, transmission, and influence [46].

4.1. Inductively Coupled Piezoelectric Acoustic Transducer. Electrical excitation to a piezoelectric acoustic transducer can be achieved through inductive coupling. In Figure 31, this concept is depicted. A PZT wafer is wired to a winding (1) and bonded onto the substrate to inspect. The electrical

excitation is sent to winding 2 and coupled to winding #1 inductively to excite the PZT wafer. Ferrite cores are used to increase the mutual inductance. The PZT wafer, when excited electrically, generates acoustic waves in the structure through converse piezoelectric effect. The same setup can also sense acoustic waves propagating in the structure via piezoelectric effect and inductive coupling. If operated in pulse/echo mode, an additional coil, winding 3, can be used for sensor signal output [25]. Depending on the characteristics of the probes, the separation of the excitation and sensing probes (windings 2 and 3) from the sensing element (PZT and winding 1) can be as large as 20 cm [47] and allows both the probe and the sensing element to be completely sealed, therefore offering a superior protection. Since the sensing element can be entirely built in a compact enclosure, it could be conveniently embedded in or mounted on a structure for structural health monitoring [25]. Figure 32 illustrates a planar transducer design using a coil on a printed circuit board. The PZT top surface is patterned to form two electrodes. Connections are made through a ferrite sheet to a printed circuit board containing a two-layer and spiral-wound coil [25]. A prototype of this design, paired with a pulse generation and detection probe with winding 2 wound on a ferrite pot core of similar size, is shown in Figure 33. This transducer pair was able to generate and detect S_0 and A_0 modes of Lamb waves in a 3.2 mm thick steel plate girder in a frequency range from 250 kHz to 351 kHz and for a probe-to-transducer coil distance up to 6 mm. The inductively coupled non-contact wave generation and detection approach could be highly beneficial to applications for inspection of a mobile structure, for example, a helicopter rotor blade, by bonding a sensing element on the blade while keeping the excitation/sensing probe(s) on a fixed base at a close distance to the blade. A diagnostic signal can be generated and detected when the sensing element passes in front of the excitation/sensing probe(s). This configuration enables a minimization of the weight of the transducer system installed in the rotating component with a view to respect the small maximum weight

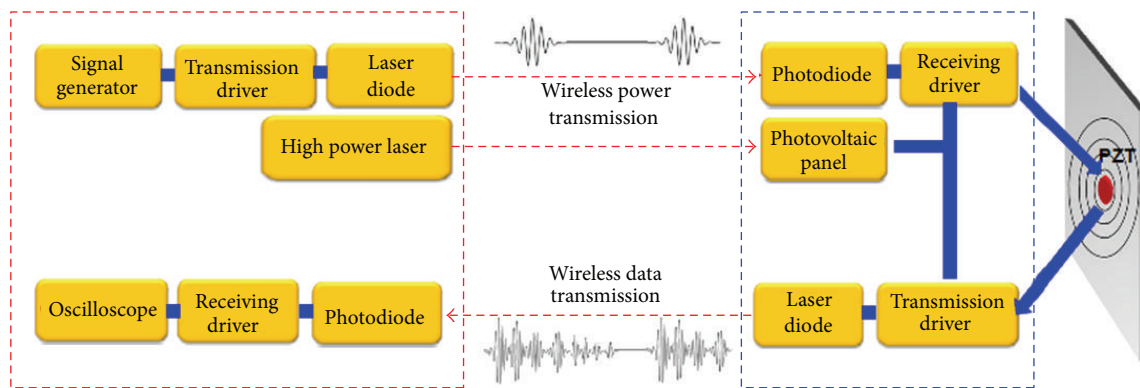


FIGURE 37: A schematic for optics based wireless guided wave generation and sensing [30].

that can be added to such rotating components (restricted by the operation conditions of such structures, in terms of their inertia, vibration, balancing, etc.).

4.2. Capacitively Coupled Piezoelectric Acoustic Transducer. Capacitive coupling is another approach to wireless acoustic wave excitation and detection. In Figure 34, a test setup is presented, in which a PVDF transducer is bonded to one end of an aluminum plate. A transmitting monopole antenna delivers radio frequency (RF) pulses wirelessly through an on-board monopole antenna to the PVDF transducer for generating Lamb waves, and another active monopole receives the ultrasonic echoes from the PVDF sensor through the same on-board monopole antenna. The antennas are made of 6.5 mm diameter aluminum tubes [28]. A fundamental limitation of this approach is the required short coupling distance (<10 cm). Large antenna size can also be an issue for practical applications.

4.3. Microwave Powered Wave Generation and Detection. Microwaves are electro-magnetic waves in the 300 MHz to 300 GHz frequency range. These frequencies are too high for the generation and detection of acoustic waves through direct coupling with conventional piezoelectric acoustic transducers which usually operate in the tens of kHz to several tens of MHz range for most NDE/NDI applications. However, microwave energy can be used to power an embedded piezoelectric based diagnostic device. In Figure 35, the diagram of an embedded ultrasonic SHM system is presented [28]. As embodiment, the power for the embedded sensor system was provided wirelessly from a 10 GHz transmitter and horn antenna at a 1 m range from the inspected aircraft wing. A 10 GHz patch antenna array loaded with rectifiers (rectenna array) was conformably mounted onto the inspected wing to convert incident microwave power to DC power, as depicted in Figure 36.

4.4. Wireless PZT Excitation and Sensing with Laser. Lasers have also been used to generate and transmit power wirelessly to achieve non-contact piezoelectric based acoustic wave generation and sensing. A schematic of the concept is given in Figure 37. An electric waveform generated with a signal

generator is converted into a laser power modulation using a transmission (T_x) driver, and the laser wirelessly transmits a generated waveform to a photodiode. The photodiode converts the received laser light modulated intensity into electric current (proportionally to the received light power). The generated current signal is then converted into proportional electric voltage, through on-board electronic circuitry, by a receiving (R_x) driver, which is used to excite the PZT attached onto the host structure. The excited PZT consequently creates diagnostic guided waves within the structure. The reflected waves are measured by the same PZT and reconverted into a laser power modulation using the on-board laser and T_x driver. The laser light with modulated power is transmitted back to another photodiode located in the data acquisition unit for diagnosis. Again, in this photodiode the variations in the received laser light intensity (proportional to the PZT sensor signal and to the detected waves) are translated to corresponding variations in an electrical signal, which can be interpreted for wave detection analysis. An additional 5 W high power laser is utilized to supply the power necessary for operation of the T_x and R_x drivers at the PZT transducer node [30]. The laser based approach enabled the excitation of the transducer and the acquisition of diagnostic signals with the laser and transducer being separated by distances of around 0.6 m to 1 m (with the working pairs of emitting lasers and receiving photodiodes having to be in-line of sight between each other). This feature could be beneficial for inspection of areas which are difficult to access. Owing to its capability of transmitting arbitrary waveforms and capability of the PZT to sense both in-plane and out-of-plane vibrations, the technique could be better suited for tuned wave generation and detection than conventional laser ultrasonics. Examples of potential applications and usefulness for this system are presented in [48–51].

5. Conclusions

In this paper, different concepts and a number of approaches to generating and detecting diagnostic acoustic waves for SHM through the use of piezoelectric acoustic transducers are reviewed. All approaches aim to address three basic

requirements to attain a successful SHM system and application: generating a diagnostic wave which is effective in revealing structure integrity information; generating and detecting the desired wave in an efficient manner; generating and detecting the desired wave in a way that is practical. Although this paper is divided into three categories, some of the concepts may be fused together to form a more powerful solution to a specific problem.

References

- [1] J. L. Rose, "Dispersion curves in guided wave testing," *Materials Evaluation*, vol. 61, no. 1, pp. 20–22, 2003.
- [2] J. L. Rose, "Waves in plates," in *Ultrasonic Waves in Solid Media*, pp. 101–131, Cambridge University Press, New York, NY, USA, 1999.
- [3] T. R. Hay and J. L. Rose, "Flexible piezopolymer ultrasonic guided wave arrays," *IEEE Transactions on Ultrasonics, Ferroelectrics, and Frequency Control*, vol. 53, no. 6, pp. 1212–1217, 2006.
- [4] H. Lamb, "On waves in an elastic plate," *Proceedings of the Royal Society of London. Series A*, vol. 93, pp. 114–128, 1917.
- [5] V. Giurgiutiu, "Tuned Lamb wave excitation and detection with piezoelectric wafer active sensors for structural health monitoring," *Journal of Intelligent Material Systems and Structures*, vol. 16, no. 4, pp. 291–305, 2005.
- [6] J. L. Rose, "Ultrasonic guided waves in structural health monitoring," *Key Engineering Materials*, vol. 270–273, no. 1, pp. 14–21, 2004.
- [7] J. L. Rose and L. E. Soley, "Ultrasonic guided waves for anomaly detection in aircraft components," *Materials Evaluation*, vol. 58, no. 9, pp. 1080–1086, 2000.
- [8] V. Giurgiutiu, "Tuned waves generated with piezoelectric wafer active sensors," in *Structural Health Monitoring With Piezoelectric Wafer Active Sensors*, pp. 309–362, Academic Press, San Diego, Calif, USA, 1 edition, 2008.
- [9] V. Giurgiutiu, "Piezoelectric wafer active sensors," in *Structural Health Monitoring with Piezoelectric Wafer Active Sensors*, pp. 297–300, Academic Press, San Diego, Calif, USA, 1 edition, 2008.
- [10] B. Rocha, *Structural Health Monitoring of Aircraft Structures*, Instituto Superior Tecnico (IST), Lisbon, Portugal, 2011.
- [11] S. H. Lim, I. K. Oh, and J.-R. Lee, "Ultrasonic active fiber sensor based on pulse-echo method," *Journal of Intelligent Material Systems and Structures*, vol. 20, no. 9, pp. 1035–1043, 2009.
- [12] S.-C. Wooh, "Tuned wave phased array," USA Patent 6,728,515 B1, 27, April 2004.
- [13] J.-R. Lee and H. Tsuda, "Investigation of a fibre wave piezoelectric transducer," *Measurement Science and Technology*, vol. 17, no. 9, pp. 2414–2420, 2006.
- [14] B. Culshaw, G. Thursby, D. Betz, and B. Sorazu, "The detection of ultrasound using fiber-optic sensors," *IEEE Sensors Journal*, vol. 8, no. 7, pp. 1360–1367, 2008.
- [15] V. Giurgiutiu, "In-situ phased arrays with piezoelectric wafer active sensors," in *Structural Health Monitoring With Piezoelectric Wafer Active Sensors*, pp. 503–588, Academic Press, New York, NY, USA, 2008.
- [16] V. Giurgiutiu and J. Bao, "Embedded-ultrasonics structural radar for in situ structural health monitoring of thin-wall structures," *Structural Health Monitoring*, vol. 3, no. 2, pp. 121–140, 2004.
- [17] J. L. Rose, Z. Sun, P. J. Mudge, and M. J. Avioli, "Guided wave flexural mode tuning and focusing for pipe testing," *Materials Evaluation*, vol. 61, no. 2, pp. 162–167, 2003.
- [18] M. Kobayashi and C.-K. Jen, "Piezoelectric thick bismuth titanate/lead zirconate titanate composite film transducers for smart NDE of metals," *Smart Materials and Structures*, vol. 13, no. 4, pp. 951–956, 2004.
- [19] M. Kobayashi, C.-K. Jen, J. F. Bussiere, and K.-T. Wu, "High-temperature integrated and flexible ultrasonic transducers for nondestructive testing," *NDT & E International*, vol. 42, no. 2, pp. 157–161, 2009.
- [20] N. Rajic, C. Davis, and A. Thomson, "Acoustic-wave-mode separation using a distributed Bragg grating sensor," *Smart Materials and Structures*, vol. 18, no. 12, Article ID 125005, 2009.
- [21] Z. Wu, X. P. Qing, and F. K. Chang, "Damage detection for composite laminate plates with a distributed hybrid PZT/FBG sensor network," *Journal of Intelligent Material Systems and Structures*, vol. 20, no. 9, pp. 1069–1077, 2009.
- [22] K.-T. Wu, Z. Sun, and N. Mrad, "A comparative study on two families of integratable ultrasound transducers for structural health monitoring," in *Proceedings of the International Workshop on Smart Materials & Structures and NDT in Aerospace*, 2011.
- [23] W. J. Staszewski, S. Mahzan, and R. Traynor, "Health monitoring of aerospace composite structures—active and passive approach," *Composites Science and Technology*, vol. 69, no. 11–12, pp. 1678–1685, 2009.
- [24] C.-K. Jen, K.-T. Wu, M. Kobayashi, J. H. Kuo, and N. Mrad, "Integrated surface and plate acoustic wave sensors for health monitoring," in *Health Monitoring of Structural and Biological Systems*, vol. 6532 of *Proceedings of SPIE*, San Diego, Calif, USA, March 2007.
- [25] D. W. Greve, H. Sohn, C. P. Yue, and I. J. Oppenheim, "An inductively coupled lamb wave transducer," *IEEE Sensors Journal*, vol. 27, no. 2, pp. 295–301, 2007.
- [26] K.-T. Wu, W. L. Liu, M. Kobayashi, C.-K. Jen, Y. Ono, and M. Takeuchi, "High temperature guided acoustic wave transducers using mechanical gratings," in *Proceedings of IEEE International Ultrasonics Symposium (IUS '09)*, September 2009.
- [27] P. Zheng, D. W. Greve, and I. J. Oppenheim, "Crack detection with wireless inductively-coupled transducers," in *Sensors and Smart Structures Technologies for Civil, Mechanical, and Aerospace Systems*, vol. 6932 of *Proceedings of SPIE*, San Diego, Calif, USA, 2008.
- [28] X. Zhao, T. Qian, G. Mei et al., "Active health monitoring of an aircraft wing with an embedded piezoelectric sensor/actuator network: II. Wireless approaches," *Smart Materials and Structures*, vol. 16, no. 4, pp. 1218–1225, 2007.
- [29] K.-T. Wu, C.-K. Jen, and N. Mrad, "Non-contact local and global damage detection with integrated ultrasonic transducers," in *Sensors and Smart Structures Technologies for Civil, Mechanical, and Aerospace Systems*, vol. 6932 of *Proceedings of SPIE*, San Diego, Calif, USA, 2008.
- [30] H. J. Park, H. Sohn, C. B. Yun, J. Chung, and M. Lee, "Development of a non-contact PZT excitation and sensing technology via laser," in *Sensors and Smart Structures Technologies for Civil, Mechanical, and Aerospace Systems*, vol. 7981, San Diego, Calif, USA, March 2011.
- [31] C.-K. Jen, K.-T. Wu, and M. Kobayashi, "Ultrasonic probes having three orthogonal polarizations," *IEEE Transactions on Ultrasonics, Ferroelectrics, and Frequency Control*, vol. 57, no. 1, pp. 189–192, 2010.

- [32] S. S. Kessler and A. Raghavan, "Co-located triangulation for damage position identification from a single SHM node," in *Proceedings of the International Conference on Prognostics and Health Management (PHM '08)*, Denver, Colo, USA, October 2008.
- [33] H. Sohn and S. B. Kim, "Development of dual PZT transducers for reference-free crack detection in thin plate structures," *IEEE Transactions on Ultrasonics, Ferroelectrics, and Frequency Control*, vol. 57, no. 1, pp. 229–240, 2010.
- [34] J.-R. Lee and H. Tsuda, "Sensor application of fibre ultrasonic waveguide," *Measurement Science and Technology*, vol. 17, no. 4, pp. 645–652, 2006.
- [35] N. Mrad, H. Guo, G. Xiao, B. Rocha, and Z. Sun, "On the use of a compact optical fiber sensor system in aircraft structural health monitoring," in *Photonic Applications for Aerospace, Transportation, and Harsh Environment III*, vol. 8368 of *Proceedings of SPIE*, Baltimore, Md, USA, 2012.
- [36] J.-R. Lee, J. Takatsubo, N. Toyama, and D. H. Kang, "Health monitoring of complex curved structures using an ultrasonic wavefield propagation imaging system," *Measurement Science and Technology*, vol. 18, no. 12, pp. 3816–3824, 2007.
- [37] B. Wang, J. Takatsubo, N. Toyama, and M. Zhao, "The development of laser ultrasonic visualization equipment and its application in nondestructive inspection," in *Proceedings of the 17th World Conference on Nondestructive Testing*, Shanghai, China, 2008.
- [38] C. C. Chia, J.-R. Lee, and H. J. Shin, "Hot target inspection using a welded fibre acoustic wave piezoelectric sensor and a laser-ultrasonic mirror scanner," *Measurement Science and Technology*, vol. 20, no. 12, Article ID 127003, 2009.
- [39] C. C. Chia, H.-M. Jeong, J.-R. Lee, and G. Park, "Composite aircraft debonding visualization by laser ultrasonic scanning excitation and integrated piezoelectric sensing," *Structural Control and Health Monitoring*, vol. 19, no. 7, pp. 605–620, 2012.
- [40] V. V. Kozhushko and H. Krenn, "Detection of laser-induced nanosecond ultrasonic pulses in metals using a pancake coil and a piezoelectric sensor," *IEEE Transactions on Ultrasonics, Ferroelectrics, and Frequency Control*, vol. 59, no. 6, pp. 1233–1238, 2012.
- [41] F. Yang, D. J. Dorantes-Gonzalez, K. Chen et al., "An integrated laser-induced piezoelectric/differential confocal surface acoustic wave system for measurement of thin film young's modulus," *Sensors*, vol. 12, no. 9, pp. 12208–12219, 2012.
- [42] K.-T. Wu, C.-K. Jen, M. Kobayashi, and A. Blouin, "Integrated piezoelectric ultrasonic receivers for laser ultrasound in non-destructive testing of metals," *Journal of Nondestructive Evaluation*, vol. 30, no. 1, pp. 1–8, 2011.
- [43] J.-R. Lee, C. C. Chia, H. J. Shin, C.-Y. Park, and D. J. Yoon, "Laser ultrasonic propagation imaging method in the frequency domain based on wavelet transformation," *Optics and Lasers in Engineering*, vol. 49, no. 1, pp. 167–175, 2011.
- [44] E. B. Flynn, J.-R. Lee, G. J. Jarmer, and G. Park, "Frequency-wavenumber processing of laser-excited guided waves for imaging structural features and defects," in *Proceedings of the 6th European Workshop on Structural Health Monitoring*, Dresden, Germany, 2012.
- [45] S.-C. Hong, J.-R. Lee, S. Y. Chong, C.-Y. Park, and S. Girrens, "Effect of laser pulse fatigue on the mechanical characteristic of an unpainted CFRP plate," in *Advances in Structural Health Management and Composite Structures (ASHMCS '12)*, Jeonju, Republic of Korea, 2012.
- [46] H. Gao, B. Lopez, S. M. Ali, J. Flora, and J. Monks, "Inline testing of ERW tubes using ultrasonic guided wave EMATs," in *16th US National Congress of Theoretical and Applied Mechanics (USNCTAM '10)*, State College, Pa, USA, June-July 2010.
- [47] R. Murayama, M. Kobayashi, K.-T. Wu, and C.-K. Jen, "Non-contact ultrasonic sensing using induction based method and integrated piezoelectric ultrasonic transducer," in *Proceedings of Symposium on Ultrasonic Electronics*, 2010.
- [48] H. J. Park, H. Sohn, C. B. Yun, J. Chung, and I. I. B. Kwon, "A wireless guided wave excitation technique based on laser and optoelectronics," *Smart Structures and Systems*, vol. 6, no. 5-6, pp. 749–765, 2010.
- [49] H.-J. Park, H. Sohn, C.-B. Yun, and J. Chung, "Development of a laser-based wireless active sensing technique," in *Proceedings of the 6th International Workshop on Advanced Smart Materials and Smart Structures Technology (ANCRiSST '11)*, Dalian, China, 2011.
- [50] H. Sohn, "Laser based structural health monitoring for civil, mechanical and aerospace systems," in *Sensors and Smart Structures Technologies for Civil, Mechanical, and Aerospace Systems*, vol. 8345 of *Proceedings of SPIE*, San Diego, Calif, USA, 2012.
- [51] H.-J. Park, H. Sohn, C.-B. Yun, J. Chung, and M. M. S. Lee, "Wireless guided wave and impedance measurement using laser and piezoelectric transducers," *Smart Materials and Structures*, vol. 21, no. 3, Article ID 035029, 2012.

Research Article

Operational Readiness Simulator: Optimizing Operational Availability Using a Virtual Environment

Shaun Horning,¹ Philip Leung,¹ Andy Fitzgerald,² and Nezhir Mrad³

¹ Controls and Simulation Department, GasTOPS Ltd., Ottawa, ON, Canada K1J 9J3

² ACF Associates, Bath, ON, Canada K0H 1G0

³ Defence R&D Canada, Department of National Defence, Ottawa, ON, Canada K1A 0K2

Correspondence should be addressed to Nezhir Mrad, nezhir.mrad@drdc-rddc.gc.ca

Received 11 March 2012; Accepted 14 August 2012

Academic Editor: Peter Foote

Copyright © 2012 Shaun Horning et al. This is an open access article distributed under the Creative Commons Attribution License, which permits unrestricted use, distribution, and reproduction in any medium, provided the original work is properly cited.

The maintenance and logistics systems that support aircraft fleets are complex and often very integrated. The complexity of these systems makes it difficult to assess the impact of events that affect operational capability, to identify the need for resources that can affect aircraft availability, or to assess the impact and potential benefits of the system and procedural changes. This problem is further complicated by the adoption of condition-based maintenance approaches resulting in dynamic maintenance planning as maintenance tasks are condition directed instead of scheduled or usage based. A proof of concept prototype for an aircraft operational readiness simulator (OR-SIM) has been developed for the Canadian Forces CH-146 Griffon helicopter. The simulator provides a synthetic environment to forecast and assess the ability of a fleet, squadron, or aircraft to achieve desired flying rates and the capability of the sustainment systems to respond to the resultant demands. The prototype was used to assess several typical scenarios including adjustment of preventative maintenance schedules including impact of condition-based maintenance, variation of the annual flying rate, and investigation of deployment options. This paper provides an overview of the OR-SIM concept, prototype model, and sample investigations and a discussion of the benefits of such an operational readiness simulator.

1. Background

Operational availability, capability, or readiness, also known as aircraft mission capable rates, is used to describe the availability of aircraft to fly their assigned missions. Fleet operation and sustainment systems for Air Force weapon systems are highly complex and multilayered and involve stakeholders from different commands within the military, the public service, and industry. There exist three primary elements through which operational capability is generated. The first is the weapon system maintenance plan. The second is the capability and capacity of the maintenance organizations (e.g., Air Force and support contractors) to produce available aircraft through the execution of the maintenance plan. The third is the aircraft operational concept through which the Air Force uses and “consumes” the available aircraft. As shown in Figure 1, the interaction or “fit” of these three elements determines the operational capability of a given fleet. From the perspective of an operational capability model, the

interaction of these elements across different armed forces weapon systems combine to determine the overall operational capability of the armed forces of a nation.

Improving the fit, and thereby increasing the capability, involves understanding the characteristics of each element and the interactions between them and then taking steps to align these elements to maximize such operational capability. Leaders and managers at all levels make decisions that have the potential to either improve or deteriorate the existing fit of these three elements and therefore affect operational capability yet there is no readily available tool through which this impact can be assessed. The result is that potential impacts on operational capability cannot be reliably determined prior to making decisions on these changes.

Furthermore initiatives such as condition-based maintenance (CBM) that may improve operational capability cannot be supported by any objective evidence linking the initiative to the benefit. Central to the CBM concept is the idea that maintenance planning and scheduling become

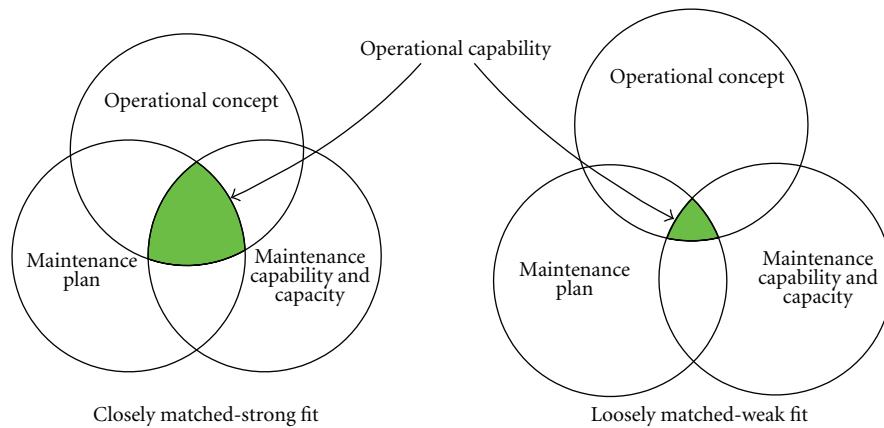


FIGURE 1: Interactions that affect operational capability.

condition directed instead of static or usage based. CBM holds the potential to significantly improve the operational not only availability and ownership costs of aircraft fleets but also increases the complexity and dynamics of fleet sustainment systems. Since with CBM, maintenance actions are driven by need, rather than on a routine or repetitive basis, the coordination of maintenance resources becomes much more dynamic as available resources are deployed to meet the emerging maintenance needs.

Therefore, there exists a need for a means to forecast and assess the ability of a fleet, squadron, or aircraft to achieve a desired operational availability and the capability of the sustainment systems to respond to the resultant demands. In addition, there is a requirement for a scenario planning and assessment capability for operations and maintenance planners, which can be used for quantitative assessments of changes to operations and sustainment plans and to provide a dynamic schedule forecasting capability to assess short- and long-term resource requirements based on forecasted aircraft flying rates. Ideally, this would be implemented in a model in a synthetic (virtual) environment where knowledge of the fleet sustainment systems can be consolidated and provide a true capability to manage operational capability instead of simply managing fleets, aircraft, or contracts.

1.1. CH-146 Griffon Helicopter. The CH-146 Griffon is the Canadian military variant of the Bell 412EP, a multiuse utility helicopter powered by two Pratt and Whitney PT6T gas turbine engines. The Griffon is a multiuse platform equipped to provide aerial support reconnaissance, search, rescue, and mobility tasks. The fleet of CH-146 Griffon Utility Tactical Transport Helicopters is divided into six squadrons spread out across Canada. Collectively, these squadrons operate under the command of 1 Wing Kingston. Five Tactical Helicopter Squadrons support specific Army brigades within their geographic regions. The sixth squadron is an operational training squadron.

While collectively the squadrons operate under the command of 1 Wing, the squadrons are self-contained and field deployable and as such each squadron operates relatively independently of the other squadrons. As each squadron fulfills slightly different roles, the number of aircraft assigned

to each squadron and the number and duration of missions that the squadron flies vary resulting in different usage rates of the aircraft assigned to each squadron. Like all aircraft, the CH-146 has a scheduled (i.e., preventative) maintenance plan. The CH-146 preventative maintenance plan includes both usage and calendar-based inspections of key aircraft components such as airframe, engine, and gearbox. Since aircraft usage tends to vary between squadrons, the resulting preventative maintenance burden is also different.

In addition to the preventative maintenance, the squadrons must also contend with component failures, troubleshooting of issues on the AC, and reconfiguration of the AC for different missions. These tasks are collectively referred to as corrective maintenance and together the preventative and corrective maintenance result in aircraft downtime (i.e., unavailable to fly missions).

The maintenance resources such as the number of repair bays, paint booths, and qualified maintenance personnel also differ between the squadrons. In each squadron, the senior squadron maintenance personnel must optimize the use of the squadron's limited maintenance resources to maintain a level of availability that best meets the demands for operational aircraft. For example, the maintenance planner must assign personnel to specific maintenance tasks to ensure that both short-term and long-term maintenance actions are completed. The squadron personnel must also attempt to assign aircraft to missions such that the upcoming scheduled maintenance for the aircraft is staggered so as to not overload the maintenance capacity of the squadron.

The squadron to squadron differences in number of aircraft, quality of aircraft, aircraft usage rates, and the number and availability of resources represents a difficult modelling challenge and necessitates the need for a data-driven model that can be configured based on the input data. The data input structures must be generic enough to handle the squadron to squadron variations.

1.2. Discrete Event Simulation (DES). The basis for discrete event simulation is a "transaction-flow world view" where a system is visualized as consisting of discrete units of traffic (or "entities") that move ("flow") from point to point in the system while competing with each other for scarce

resources. DES is ideally suited to model a variety of systems ranging from manufacturing, supply chain, customer service, communications, and defence. The state of a model in DES changes at only discrete but possibly random sets of simulated time points. During these time points, one or more entities may move. The general structure of DES software is described in detail in textbooks and papers such as [1]. DES is ideally suited for simulating aircraft operations and support systems. The aircraft would be the entities and different points in the system would represent different processes such as maintenance, the flying of missions, and pre- and postflight checks. To perform an analysis using DES, one or more replications are required. A replication is the execution (running) of the model from start to completion. Multiple replications use the same model but with a different set of (generated) random numbers and so produce different statistical results. The results across multiple replications can then be analyzed to determine averages.

MathWorks provides a toolbox for its Simulink simulation environment called SimEvents [2] for the development of event-based simulations. Since Simulink is a time marching simulation environment, it is also possible to develop hybrid (continuous and event-based) simulations making it ideally suited for development of component degradation models. The use of SimEvents also leverages the data import/export capabilities of MATLAB/Simulink to access either databases or Microsoft Excel workbooks. Aircraft components modelled in SimEvents retained all of their attributes (data) when combined and/or separated with other components. MATLAB/Simulink/SimEvents combine a powerful programming language and modelling toolset with a DES capability making it ideal for use as the modelling environment.

2. Operational Readiness Simulator Model

2.1. Model Overview. The operational readiness simulator (OR-SIM) is a DES model of the fleet operations and maintenance activities. The model simulates flight operations of a squadron and the resulting preventative and corrective maintenance of individual aircraft. The fault characteristics of specific components on specific aircraft are simulated creating a unique simulation of each aircraft. In addition, component degradation models allow for the assessment of condition-based maintenance burdens.

The OR-SIM model is a “closed” simulation where all the input data is preloaded at model initialization and no other (user) inputs are required while the simulation is executing. The model inputs, consisting of configuration, operation, and maintenance data, are stored in data templates that are read in on initialization and the data is then propagated throughout the model to populate the various component models. Examples of model input data include squadron and aircraft specific operations and maintenance data such as squadron nominal flying rates and aircraft component flight hours. Monte Carlo simulation techniques are then used to address the stochastic nature of this data. In addition, scenario specific time scheduled events such as the start of a fleet-wide modification can be used to modify the base

data set. The model data is described in more detail in a subsequent section.

As shown in Figure 2, the model structure is divided into three main components: Aircraft Initialization, Flight Line, and Maintenance. These submodels are briefly described in the following paragraphs.

In the Aircraft Initialization model, AC subcomponent (e.g., airframes, engines, etc.) entities are created and populated with initial usage, condition indicator, scheduled maintenance, and failure data. As the entities are created, they are combined to form AC entities according to the configuration data by matching unique identifiers (e.g., engine serial numbers and airframe tail numbers) and the completed AC entities are sent to the Flight Line model.

The Flight Line model consists of models of the mission planning, preflight checks, mission flying, and postflight checks. The mission planning model selects suitable AC to fly as many of the day’s scheduled missions as possible. The selection of AC in the mission planning model simulates the techniques used by the Air Force to optimize availability by assigning AC to missions so as to maximize use prior to time consuming calendar backstopped inspections (referred to as “stagger”). The pre- and postflight check models check the component failure flags to determine if a component failure has been detected and processes the AC based on the failure effect code. The preflight check model also includes a model of the power assurance check (PAC) that is used to update the interturbine temperature (ITT) margin condition indicator values stored for each engine on the AC.

After the preflight check, the AC entity proceeds to the fly sortie model which consists of three processes: determining in-flight failures, updating component usage, and degradation levels, and holding the AC to simulate the mission time. As part flying the mission, the model simulates component degradation which then results in changes to the condition indicators (e.g., ITT Margin) that are used to trigger condition-based maintenance tasks. Statistical representations of degradation rates determined as a function of mission type and duration and key environmental conditions (e.g., desert versus marine operations) are used to degrade performance as part of each mission. These relationships can be determined through analysis of historical data, experimental study, and detailed performance simulations. Once the AC returns from the mission, it proceeds to the postflight check model.

The Maintenance model includes a maintenance and resource planning model that simulates a maintenance manager and assigns resources to aircraft in maintenance. This model is based on techniques used by squadron maintenance managers to optimize availability by ensuring that long duration maintenance actions such as the annual inspection are continuously worked on. Each maintenance manager can have a unique approach to assigning resources to specific tasks. The model can be adjusted to evaluate different approaches to the assignment of resources to tasks. Once the resources are assigned, the aircraft and resources are processed in the maintenance work model. In the maintenance work model, the fraction of time that the maintenance personnel is working on the AC is simulated as

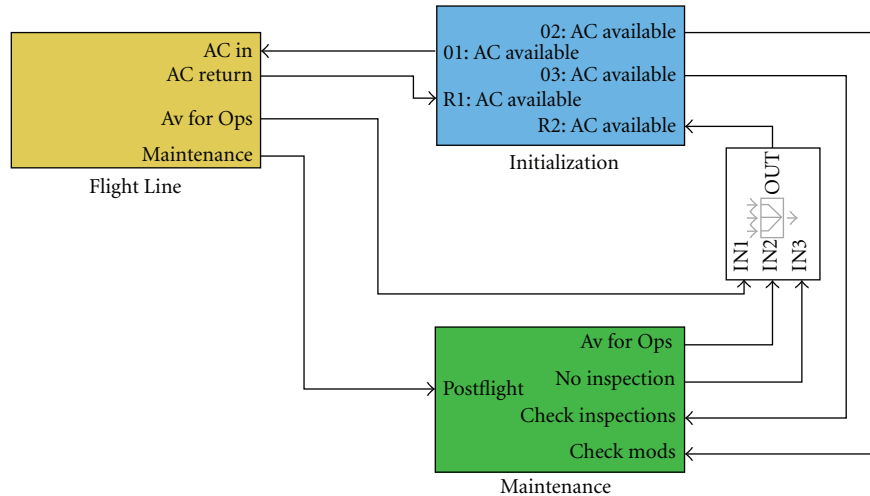


FIGURE 2: OR-SIM SimEvents model.

a contiguous period of time and interruptions are simulated by reducing the time the resource is available during the shift. For example, while maintenance personnel may work an eight hour work shift, due to other responsibilities (e.g., training, base defence, etc.) they may only be available to work on maintenance tasks 50% of the time. When all of the maintenance actions are completed, the maintenance records are closed and the maintenance flags are reset and the AC is returned to the flight line.

During run time, model parameters are continuously monitored and stored in output variables along with a time stamp so that time histories of parameters can be produced. When a test (replication) is completed, all of the model data is saved to an output results files. Results files from replication sets are then postprocessed to determine outputs suitable for direct comparison to data normally captured by the Air Force (e.g., aircraft flying hours, downtime, etc.) and can be viewed for specific actions.

2.2. Model Input Data. The OR-SIM model input data consists of three types of data: configuration, operation, and maintenance data. Configuration data is primarily used in model initialization to create and populate the AC entities. The input operational data is used to determine when AC fly and how long they fly to simulate the missions that were flown during the study period. Maintenance input data includes component failure rates, scheduled maintenance plans, and the time required to complete maintenance tasks.

The current version of the OR-SIM simulates only 4 major subassemblies (components or entities) of the CH-146: airframe, engine, gearbox, and rotor. These were selected primarily based on the preventative maintenance plan for the CH-146 which is divided into airframe, engine, and gearbox inspections. To accurately model the fleet, the simulated AC entities must reflect the same configuration and usage as the fleet at the start of the study period. Each component is created at model initialization, populated with usage data such as current flying hours and condition indicator values, and assembled into AC according to the

configuration data. To properly model aircraft maintenance, previous maintenance dates and component failure data are also assigned to each assembled AC entity. The configuration data is used to baseline the simulated fleet to a configuration and level of usage at some point in time. Records from Health and usage monitoring systems (HUMS) installed on the AC and maintenance records for performance or power assurance checks (PAC) can be used to obtain initial values for relevant condition indicators such as ITT Margin.

Since the AC have been in use and have undergone periodic maintenance, the preventative maintenance schedule for each AC is initialized to the date and flying hours of the last scheduled maintenance. The model can then calculate the aircraft flying hours (AFH) or calendar date of the next scheduled maintenance. The component failure rates used to trigger corrective maintenance are similarly initialized.

The operational data is a function of the operational concept or profile. This data is used to determine the number of missions and the durations of the missions to simulate the AC usage. Different mission types can be simulated and distributions are used to add variation to the flights and durations. A usage factor is used to define the ratio of AFH (engine-on-time) to the actual time that the AC is executing the mission. A repeating schedule of a single day, week, month, year, and so forth can be used.

The OR-SIM maintenance data consists of component failure data, scheduled maintenance plan, maintenance completion data, and squadron resource levels.

Component failure data is used to trigger corrective maintenance activities. The failure data consists of failure rates, when the failure was detected and the effect that the failure had on the mission (e.g., no effect, delay, abort, etc.). Ideally, a mean flight hours to failure and standard deviation would be calculated for each corrective maintenance type (Work Unit Code or WUC) for each AC. However, the historical failure rates were generally low so that an AC specific average and standard deviation for each WUC for all AC could not be calculated. Therefore, a method based on dividing and categorizing the fleet based on failure rate was used to

obtain the average and standard deviation component failure rates. A discrete distribution was used to model the effect of the failure for each WUC.

For each component, the scheduled maintenance (inspection) can be triggered based on usage and/or calendar time. For each inspection, the usage and calendar time between inspections are required. In addition a usage and calendar time window are used to define a range of usage or time when the inspection would be done if the aircraft was already in maintenance. A hierarchy of concurrent scheduled maintenance is used to trigger inspections that are performed as part of other scheduled maintenance (e.g., lower usage interval inspections are performed when higher usage interval inspections are triggered).

The maintenance completion data is used by the model to determine the number of maintenance person hours (MPHR) that are required to complete each of the simulated maintenance actions. For each maintenance action, the average, standard deviation, minimum, and maximum MPHR are input into the model. A minimum calendar time value is also included to simulate delays in the parts supply network that was not modelled. For each maintenance action, minimum and maximum numbers of workers are also defined. The maintenance completion data for the OR-SIM was obtained from the historical maintenance records stored in the Air Force maintenance repository database.

The input data is stored in Microsoft Excel spreadsheets that are loaded on model initialization. The use of spreadsheets provides a means to input data in an organized and readily understandable format. The configuration and maintenance data required for the model was obtained from existing databases that track aircraft configuration and maintenance records (e.g., failure rates and maintenance action completion times). The Excel tables match airframe tail number to component (e.g., engine and gearbox) serial numbers and can be easily updated with changes in configuration. The maintenance records are preprocessed offline to calculate the required model data and saved to the Excel tables. Similarly, the preventative maintenance plan was also defined in a table in Excel that matched component inspections with usage and calendar backstops. Historical operational records of flight times by aircraft were used to create operational profiles of flights that were used by the Flight Line model to simulate the flying rate of the AC (usage hours). Squadron specific data (e.g., number of resources, available repair bays, etc.) are stored in a MATLAB data (.m) file. Different scenarios can be simulated by manipulating the input data (e.g., adding/removing inspections, increasing flying rate, etc.).

2.3. Model Output Data. The OR-SIM outputs can be calculated for an individual aircraft tail number, for a group of specific aircraft (e.g., squadron), or for the entire fleet of aircraft. Since the OR-SIM models each AC individually during the study period, almost any data regarding AC condition and location can be tracked during the simulation. For example, it is possible to examine an individual AC throughout the study period to determine when the AC was idle, when it was flying, and when it entered maintenance (and the cause for maintenance) and to track its usage and

performance/condition indicators such as ITT Margin. For convenience the outputs are grouped in the following categories: summary, operational, and maintenance.

The summary information calculated from the OR-SIM model includes common indicators of fleet performance including the total number of calendar hours that the AC spends in preventative and corrective maintenance and the operational availability (ratio of calendar hours where the aircraft is available to fly missions to the total number of calendar hours). In many cases the output must be calculated in a given time period (e.g., flying hours may be calculated per month or per year). In these cases the outputs can be calculated for specific periods and averaged (e.g., average monthly flying rate per year). In other cases the specific output is defined only at a particular instant (e.g., Preventative Maintenance/Inspection Stagger Charts). Time outputs such as MPHR and aircraft downtime can be expressed in time (e.g., hours or days) or as a relative measure (e.g., percentage of downtime due to corrective maintenance).

In addition to the summary information, the OR-SIM can output other important data including total AFH, number of mission aborts, number of maintenance hours and the total number of hours the AC are unavailable due to corrective or preventative maintenance, maintenance personnel utilization rates, AC usage between calendar-based inspections, and the time from when a modification order is issued to when the last AC receives the modification. In addition, condition indicators can be monitored to determine when maintenance was triggered to assess the effectiveness of the CBM program.

These outputs are directly comparable to the metrics used in the quarterly fleet health reports and therefore the simulation results can be used to essentially forecast the fleet health reports for different scenarios. The model summary outputs can be compared to the actual fleet health reports to evaluate and support decisions, identify bottlenecks in the organization, and predict availability.

2.4. Model Validation. The OR-SIM was validated against historical data from two squadrons over a two-year period. The objective was to predict overall results consistent with average trends found in actual fleet data. In particular, it was intended for the prototype model to predict total maintenance hours and maintenance actions and total flight hours within 10% of the fleet data.

To ensure proper model initialization or “warm-up,” the model was initialized with data from one year previous to the validation period. The warm-up period ensures that the modelled system has reached equilibrium representative of normal operations and any assumptions in the initial data no longer have an impact on the output of the system. The simulation was executed for 3 years starting with twenty replications of simulation. The initial seeds for the random number generators in the model (e.g., for determining flight duration, MPHR for maintenance actions, etc.) were randomized between replications. Once all of the replications were complete, the model outputs from each replication were processed to determine the average and the 90% confidence

interval. In general the simulation results match well with the historical records and were typically within the 10% target.

For the first squadron, the simulated squadron total AFH, downtime, and operational availability for the first year were within 2% of the fleet totals. The total maintenance MPHR was within 10% of the fleet total, although the corrective maintenance results were overpredicted by 16%. Since the model is based on average values based over several years of mean time between failure data, it cannot replicate the short-term differences in failure times that can occur in one year. The difference in actual and simulated corrective MPHR could be reduced by further refining the component fault data and possibly using more sophisticated probability distributions (e.g., Weibull) rather than the normal distribution used in the model. Since the purpose of the study was to develop a proof of concept model structure for an operational availability simulator, a rigorous analysis of the failure data was not performed and normal distributions were generally assumed. Further analysis of the reliability data may show that other distribution types provide a better fit and these can be easily accommodated with minor updates to the model and input data.

There was also some variation in the preventative maintenance MPHR distribution among the periodic maintenance types. These differences may be caused by assumptions in the initialization data, the use of waivers to extend intervals between periodic maintenance, which was not modelled, or variations in the recording of the maintenance data.

In the second year the airframe hours were again within 2%, although the availability was overpredicted by 7%. The maintenance burdens were similar to the previous year so it is possible that the drop in availability was due to a reduced maintenance capacity (i.e., maintenance personnel), or parts availability—neither of which were accounted for in the simulation input data. These influences could be further investigated, but since the results were within the validation target of 10% they were outside the scope of the prototype model.

Similar results were observed for the second squadron. The first-year model results matched the historical operational availability, downtime, total airframe hours, and total corrective MPHR within 2% or less. However, the model overpredicted the total preventative MPHR. Detailed analysis of the historical preventative maintenance records show significantly less than the expected number of monthly airframe inspections. This finding requires further investigation. The second-year validation results were similar.

3. Scenario Investigations

Once the OR-SIM was validated, it was used to investigate several different scenarios. In each scenario, the effects of a change to the fleet baseline on key fleet performance parameters such as availability, yearly flying rate, maintenance hours, and aircraft downtime were investigated. Examples of scenarios included adjustment of calendar backstops on periodic maintenance, effect of changes to squadron operating profiles (increases/decreases in flying rates), effect of deployment on operational capacity, assessment of

implementation methods for a modification, and extension of engine wash intervals based on power assurance check (PAC) results. The results of two of these investigations are discussed below.

3.1. Aircraft Flying Hours Variation. This scenario investigated the sensitivity of operational availability and preventative and corrective maintenance burdens to changes in annual flying rate. As the aircraft flying rate was changed it was expected that there would be a variation in aircraft availability and in the ratio of preventative and corrective maintenance. The aircraft flying rates were revised by $\pm 10\%$ and $\pm 25\%$ of the nominal value by adding or removing flights. A 10-year simulation of the fleet was executed and compared to the fleet baseline. For reference, a set of 20 replications was completed in approximately 19 hours on a standard single core 2010 era desktop computer. A sample of results from the simulation is shown in Figure 3.

In general, increases in flying rate resulted in decreases in operational availability but the squadron was able to still achieve the planned flying rates up to 125% of the nominal illustrating that it is possible for the squadron to support sustained increased operations with the current maintenance capacity. It is interesting to note that a 10% reduction in flying rate resulted in negligible increases in operational availability. The amounts of corrective and usage-based scheduled maintenance are functions of usage and hence flying rates. However, calendar-based scheduled maintenance is relatively constant. For the CH-146 the annual inspection represents approximately 50% of the total scheduled maintenance MPHR and is unaffected by usage or flying rate. The model shows that a minor reduction in flying rate does not reduce the remaining required scheduled maintenance enough to increase the availability.

This is an example of using the OR-SIM to forecast the effect of annual flying rate on availability and maintenance burden. It can be used to assess the capacity of the squadron to support higher flying rates and can be used to forecast the expected preventative and corrective maintenance hours that will be required to support the new flying rates. The model can also be used to identify aspects of the maintenance plan (e.g., calendar backstops on preventative maintenance) that can lead to lower availability even with reduced flying rates.

3.2. Engine Wash. In this scenario, the OR-SIM model was used to investigate the effect of increasing the engine wash interval as well as to simulate the impact of on-condition washes. The CH-146 maintenance plan includes an on-condition compressor wash triggered by data collected by the onboard HUMS. The PAC is an aircrew function performed with the aircraft light on skids on a daily basis (i.e., first flight of the day) to verify the engine performance. Data collected by the HUMS for each PAC is used to calculate the engine ITT margin which is used to evaluate the engine performance. The engine wash also has an operating hours limit and analysis has shown that the degradation rate between washes was negligible and so the majority of the engine washes were completed due to this schedule requirement rather than on-condition.

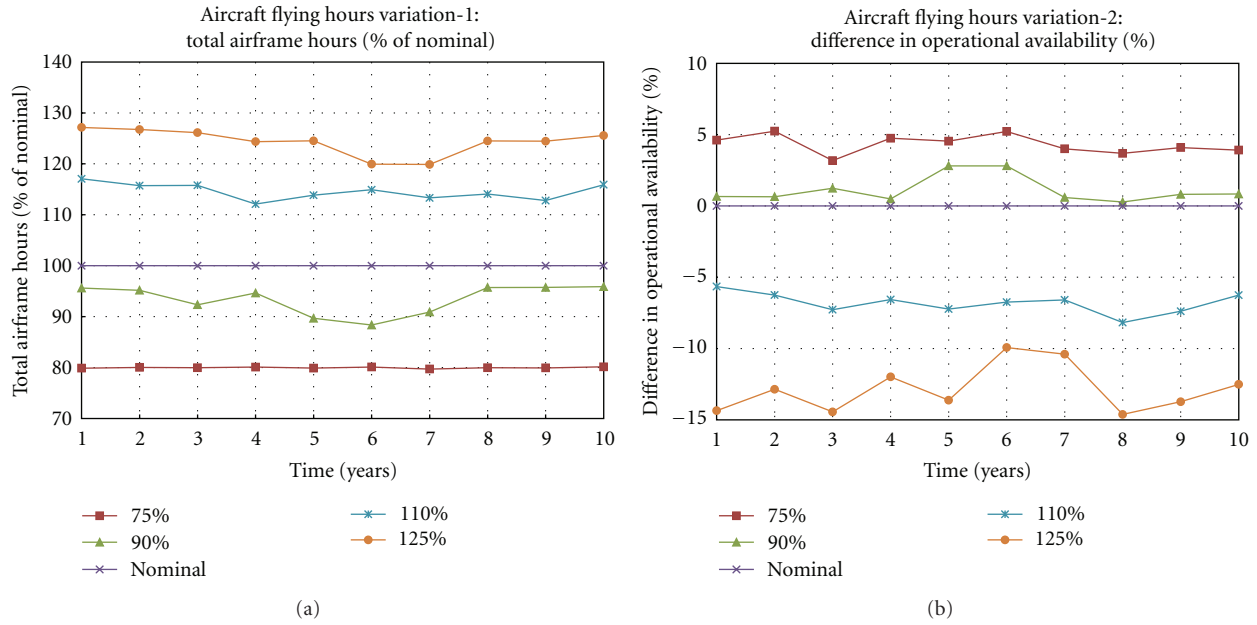


FIGURE 3: Aircraft flying hours and operational availability for variations in yearly flying rate.

TABLE 1: Extension of engine wash interval results.

Parameter (change relative to default degradation rate and schedule)	10-Year average			
	Default ITT margin Degradation rate		Increased ITT margin Degradation rate	
	Default schedule	Extended schedule	Default schedule	Extended schedule
Case	A	B	C	D
Operational availability	—	1%	-1%	0%
Down time	—	-3%	3%	0%
Total airframe hours	—	0%	0%	0%
Total maintenance MPHR	—	-1%	0%	-1%
Total washes	—	-34%	15%	-15%
Scheduled washes (% total)	100%	100%	74%	57%
On-condition washes (% total)	0%	0%	26%	43%

As part of this scenario investigation, the airframe maintenance schedules were revised to extend the operating hours limit. Since it can be expected that there would be an increase in the ITT margin degradation rate due to the extension of the operating hours limit, the model was also modified to investigate the influence of ITT margin degradation rate. It is expected that the change in degradation rate would increase the frequency of on-condition compressor washes. A 10-year simulation of the fleet was executed. In this scenario, it was assumed that the level of effort to complete the engine wash was constant between scenarios and there would be no change in fault rate of aircraft components. The results for the two compressor wash intervals for no degradation and with component degradation are summarized in Table 1.

Comparing Case B to Case A, assuming no significant degradation in the ITT margin, as expected, extending the wash schedule resulted in a reduction in the number of

engine washes and a slight increase in availability due to the reduced preventative maintenance burden. Also as expected, since the degradation rate remained the same, there were no on-condition washes. Case B represents the ideal case where the extension of the wash schedule had no impact on engine performance and would result in a 34% reduction in the number of washes. The likelihood of that is expected to be relatively low since it can be expected engine performance would be affected by having a dirty compressor/engine. These two cases (A and B) were run to provide a comparison for the cases where the degradation rate was changed.

For a simulation with an increased degradation rate and the default wash schedule (Case C), there were a number of on-condition washes which resulted in an increase in the total number of washes compared to the default case (Case A). This increase in the number of washes resulted in a decrease in availability but marginal change in the overall maintenance burden.

When the wash schedule was extended with the increased degradation rate (Case D), the total number of washes was found to decrease and a higher percentage of washes were completed on-condition compared to the previous case (Case C). Compared to the default case (Case A), even with the increased degradation rate the availability was unchanged and the overall maintenance burden was slightly decreased. Compared to Case A, the 15% less engine washes would also reduce the materiel costs for the wash fluid.

Based on these results, one could conclude that it can be expected that the extension of the compressor wash interval would yield a reduction in compressor washes of up to 34% (Case B) but likely would be closer to 15% because it is expected that the engine performance would be affected by the increased interval. To validate these results, the schedule would have to be increased and the ITT margins would have to be monitored to determine the actual degradation rate due to the extended wash interval. Once the degradation rate has been determined, this analysis can be repeated to determine the expected reduction in the total number of washes or the ratio of on-condition to scheduled washes. This scenario highlights the potential of an OR-SIM model to predict the effects of proposed changes to a CBM plan on aircraft availability and maintenance hours.

4. Summary

A CH-146 operations model was developed as a proof of concept prototype for an Operational Readiness Simulator. The model was validated against historical flight and maintenance data records for two squadrons over a two-year period. Overall, the model provided a reasonable match to the historical data. The simulated squadron total AFH, downtime, and operational availability were typically within 2% of the fleet totals. Predicted total maintenance labour hours were within approximately 10% with some differences in the distribution of preventative and corrective activities. Total preventative maintenance MPHR matched well indicating that the total preventative workload is being modelled but the historical records showed variability in the individual inspection records. The validated model successfully demonstrated that it could be used to investigate representative scenarios.

This project has developed several technological advances that incorporate a number of unique attributes and capabilities that are not readily found in previous discrete event simulations applied to the domain of fleet operations and sustainment. In particular, the incorporation and use of condition data obtained from embedded health and usage monitoring systems and the integration of process models spanning operations, logistics, and maintenance are expected to greatly enhance the fidelity and scope of the simulated operations and sustainment processes.

This work has demonstrated that an integrated model can simulate operations, scheduled, corrective, and condition-based maintenance in a synthetic environment. The fundamental framework including the procedures and techniques for modelling the operations, maintenance-and in particular the maintenance decision-making processes that was developed for this project can be used to model other

fleets or organizations. The OR-SIM model serves as a basis for models to provide the fleet managers a synthetic environment to quantify the cost-benefit tradeoffs during the decision-making processes required to manage the operations and maintenance for a fleet of vehicles or other group of complex machinery. This further allows the fleet managers the ability to assess changes to the maintenance including the assessment of impacts of condition-based maintenance on mission capability and operating costs.

Another use for an OR-SIM-type model is as a training tool to illustrate the operations of the fleet and provide candidate maintenance managers a synthetic environment to apply their understanding of the maintenance processes and receive immediate feedback on their performance.

5. Future Plans

This OR-SIM project addressed the base simulation component of the OR-SIM. There are additional simulation components as well as other components of the OR-SIM platform yet to be investigated including a user interface (for use by fleet managers and candidate maintenance managers who may not be familiar with the simulation platform). Currently the OR-SIM model is very technical and requires a user that is knowledgeable and comfortable in the modelling language to develop scenarios, execute the model, and analyze the results. The user interface component is a key component in ensuring that the target users and fleet managers are provided a means to execute the model with only a very minimal knowledge of the details and technology of the base simulation. This phase of the development would require input from the target users to ensure that the interface meets their needs and expectations. In particular the model results processing and results display will need further refinement. Web-based model hosting is also a possible component to ensure availability of the OR-SIM to users.

Additional simulation components not developed in this project include the component models primarily related to logistics (e.g., sparing/inventory management models and organization transfer models). These are models that can be developed to expand the scope of the OR-SIM model.

As previously mentioned, other possible areas of further development and analysis include refining the data collection and data reduction processes (e.g., distributions).

References

- [1] T. J. Schriber and D. T. Brunner, "Inside discrete-event simulation software: how it works and why it matters," in *Proceedings of the Winter Simulation Conference*, pp. 14–22, December 1997.
- [2] SimEvents for MATLAB/Simulink by The MathWorks, 2011, http://www.mathworks.com/products/simevents/?s_cid=HP_FP_SL_SimEvents Retrieved: April 2011.

Research Article

Integrated Instrumentation and Sensor Systems Enabling Condition-Based Maintenance of Aerospace Equipment

Richard C. Millar

Department of Systems Engineering, Naval Postgraduate School, 47323 Tate Road (Bldg. 2071), Patuxent River NAS, MD 20670, USA

Correspondence should be addressed to Richard C. Millar, rcmillar@nps.edu

Received 26 February 2012; Accepted 8 August 2012

Academic Editor: Nezih Mrad

Copyright © 2012 Richard C. Millar. This is an open access article distributed under the Creative Commons Attribution License, which permits unrestricted use, distribution, and reproduction in any medium, provided the original work is properly cited.

The objective of the work reported herein was to use a systems engineering approach to guide development of integrated instrumentation/sensor systems (IISS) incorporating communications, interconnections, and signal acquisition. These require enhanced suitability and effectiveness for diagnostics and health management of aerospace equipment governed by the principles of Condition-based maintenance (CBM). It is concluded that the systems engineering approach to IISS definition provided clear benefits in identifying overall system requirements and an architectural framework for categorizing and evaluating alternative architectures, relative to a bottom up focus on sensor technology blind to system level user needs. CBM IISS imperatives identified include factors such as tolerance of the bulk of aerospace equipment operational environments, low intrusiveness, rapid reconfiguration, and affordable life cycle costs. The functional features identified include interrogation of the variety of sensor types and interfaces common in aerospace equipment applications over multiplexed communication media with flexibility to allow rapid system reconfiguration to adapt to evolving sensor needs. This implies standardized interfaces at the sensor location (preferably to open standards), reduced wire/connector pin count in harnesses (or their elimination through use of wireless communications).

1. Scope, Objectives, and Methods

This article paper the instrumentation and sensors employed to support condition-based maintenance (CBM) of aerospace equipment, sensing the condition of equipment and components (state and operation) needed to enable diagnostics triggering necessary maintenance actions. It encompasses such instrumentation and sensors, plus the signal acquisition function and the intervening communication media, thus “integrated instrumentation/sensor systems” [IISS]. The focus is on IISS application to diagnostics and health management (DHM) enabling more cost effective CBM for the complex mechanical systems required for propulsion & power, environmental control, flight control, and other essential functions that are weight and volume constrained, tightly integrated with other systems and vehicle structure, and exposed to the full rigors of the flight envelope and environment.

Modern aerospace equipment control systems include many control sensors that may also serve CBM functions. However, IISS are being proposed and deployed for aerospace equipment diagnostics and health management (DHM) (as described by Urban [1], Litt et al. [2], and Paris et al. [3]) to enable more effective CBM. The growing complexity of such IISS is leading to consideration of distributed DHM architectures to overcome the cost, weight, and dependability challenges of centralized system architectures.

A distinction between sensor systems, or elements of sensor systems, relates to the signal acquisition bandwidth and inherent data processing requirements. The majority of the physical parameters sensed for DHM require discrete samples at relatively low rates, on the order of 100 to 1 per second. Periodic quasistatic samples of parameters such as pressure, temperature, rotational speed, strain, position, and flow are adequate for most physical system state assessments. On the other hand, dynamic sensor measurements

(acoustic, pressure fluctuations, vibratory motion, and strain...) require high bandwidth, high frequency records. This study addresses sensor system applications interrogating a multiplicity of diverse sensed parameters at relatively low bandwidth, but the conclusions may also apply to high bandwidth signal acquisition given appropriate multiplexing technologies.

It is hypothesized that, within the above bounds, a top down systems engineering approach will be more fruitful than a bottom up pursuit of advanced sensor technology in meeting user needs for more suitable and economic instrumentation and sensor solutions. This approach involves defining DHM IISS requirements and objectives, assessing user preferences, defining a functional architectural framework capturing the full range of alternative functional architectures, and identifying functional features and architectures that transform the performance, suitability and cost/benefit trades limiting the exploitation of advanced sensor capabilities in CBM. Relevant state of the art examples of these are briefly described.

2. Basic Sensor System Requirements

This section addresses the instrumentation/sensor requirements inherent to DHM IISS functionality, that is, acquisition of sensor signals indicative of equipment condition.

2.1. Accuracy, Precision, and Range. DHM may often require accurate measurements covering the full range of conditions experienced by the system in normal and abnormal operation, although in many cases thresholds identifying abnormal conditions or modes of operation may be all that is necessary. However, such thresholds may need to be field adjustable over a significant range based on service experience and high precision is required for critical measurements.

2.2. Repeatability and Stability. The operational implications of diagnostic sensor servicing or recalibration on intervals less than months and even years of service are usually unacceptable. Access to degraded sensors usually requires removal of the equipment in which it embedded. Servicing signal acquisition subsystems may not be as onerous, but it is still an undesirable cost and unavailability driver. Intermittent wire harnesses and connector faults are often the major contributor to poor repeatability of DHM sensor data. Corrupt DHM data records are common impediments to troubleshooting, prolonging, and undermining effective CBM responses.

2.3. Endurance and Reliability. Similarly, sensor and IISS dependability is crucial for diagnostic applications. Dispatch with DHM failures may be restricted, and sensors and harnesses are often inaccessible. Interconnecting harnesses are an important source of failures and false alarms that reduce mission capability and availability, and contribute to the high maintenance cost of aerospace systems.

For some specific sensor requirements in the domains considered here, for example, assessing system behavior and component state in gas turbine hot sections, sensor durability may limit the possibilities but research and development continues to expand the environmental capabilities of available sensors.

The above metrics are central to sensor selection and IISS serviceability and the overall sensor system architecture and functionality must accommodate these requirements. However, one must also consider DHM IISS requirements driven more by suitability and life cycle cost (LCC) considerations derived from the operational challenges of CBM, requirements related to the process more than the product. The sensor system must be both suitable and affordable for CBM usage. In the US Navy, CBM is expected to be implemented in accordance with the principles of reliability centered maintenance (RCM), identified as CBM+. The most cost effective solution for individual failure modes is adopted and the cost of IISS enabled CBM must be competitive with traditional approaches.

3. Suitability and Life Cycle Cost Objectives

DHM IISS design considerations and requirements must consider the application and usage of the system in serving the needs of CBM.

3.1. Serviceability and Affordability. Justifying total DHM IISS life cycle cost, including maintenance, technical support and data analysis, versus the known and accepted burden of direct periodic inspection, or removal and test, of aerospace system components is a significant barrier for DHM IISS application, even when users appreciate the value of CBM. Development and deployment of DHM IISS that are serviceable and affordable in aerospace applications limits the application of CBM.

A critical factor driving cost in instrumentation and sensor systems in aerospace applications is the usual architecture of a single sensor energized by, and communicating with, unique signal acquisition circuitry over a dedicated communication channel (usually more than a few conductors per sensor). This is less common in industrial applications, where networked "smart" sensors (e.g., Madni [4]) that locally process sensor readings and communicate the results in a standard format over a digital data bus to a central data recorder are common.

The possibility of distributed sensor & signal acquisition architectures in aerospace control system applications has been the subject of much analysis and research (e.g., see Behbahani et al. [5], Litt et al. [2], Culley and Behbahani [6], and Tulpule et al. [7]) but has been limited in application to date as the demanding aerospace operating environment and the limited thermal and vibration capabilities of available analog and digital circuit components preclude the use of such "smart" sensors.

A related issue is quality assurance for DHM IISS. Once all sensors have been installed and hooked up, verifying that the sensors are correctly hooked up and functional,

and correcting any faults, is critical. Furthermore, DHM sensors are usually expected to be field replaceable with no change in signal acquisition calibration or compensation. Both factors drive IISS cost versus capability trades, and should be considered in selecting IISS architectures that enable embedded sensor identification and functionality checks.

3.2. Compatibility versus Intrusiveness. Sensor size, the need for access and interconnections, and signal acquisition equipment weight and volume constrain the application and utility of DHM sensor systems. Provisions for accessibility of sensors and interconnects have significant impact on equipment cost, while the need to measure more parameters, more reliably, increases DHM IISS complexity and cost. As aerospace programs proceed through design and development, with tightening cost and weight margins, the weight and cost of DHM IISS combine to drive reduction or (indefinite) deferral of CBM essential capability.

3.3. Adaptability and Flexibility. A central issue in all instrumentation/sensor systems is uncertainty, the risk that what needs to be measured to meet the system performance and reliability/availability objectives has not been anticipated or considered. Aerospace equipment is designed and developed to be robust and reliable with limited reliance on preventive and corrective maintenance. Much of the need for scheduled maintenance is in response to unanticipated equipment failure modes becoming apparent late in development and in service. Thus, the ability to reconfigure DHM IISS to acquire data not foreseen when the equipment was specified and acquired is essential for effective CBM. (Xu et al. [8] emphasize these imperatives). DHM systems should be reconfigurable in days or weeks to enable data collection for informed root cause determination and to preempt significant degradation of operability and mission availability by rapid fielding of DHM system upgrades.

3.4. User Preferences. To validate the above, a survey was sent to known DHM subject matter experts [SME], asking them to rank the above factors as contributors to DHM IISS suitability. The results of the seven responses received are displayed in Figure 1, with highest priority given to serviceability in the aerospace environment but with significant concern with user needs for easy of IISS integration with the equipment serviced and adaptability to emerging CBM requirements.

When asked to weight these system level factors, the median SME responses results were intuitively satisfactory: 1, 2/3, and 1/3 for serviceability, unobtrusiveness, and flexibility, respectively.

4. Functional Architecture and Implications

4.1. DHM IISS Schematic Functional Architecture Framework. Figure 2 represents a schematic framework for DHM IISS functional architectures. It depicts a number of diverse

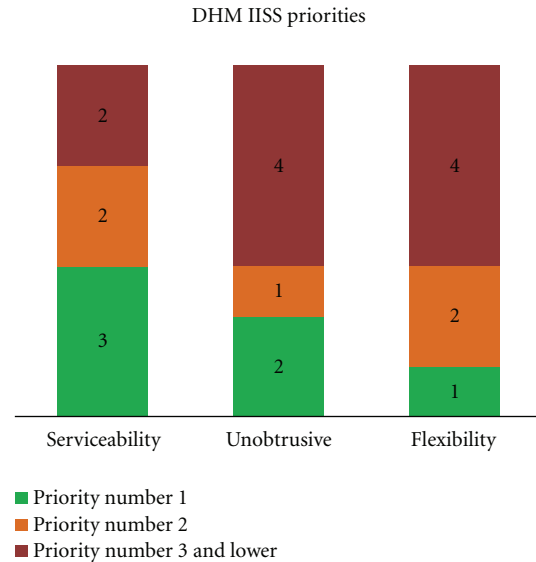


FIGURE 1: Subject matter expert ranking.

sensors monitoring a piece of aerospace equipment. This illustration neglects auxiliary elements, such as power supply and sensor excitation, to highlight the core functions for the purpose of identifying primary functional architectural options.

In this illustration, the state of a piece of equipment is measured by a number (n) of sensors, each of which first converts a physical input into an analog input intrinsic to the physical sensor mode/design (PIN-AIn). For example, sensed pressure deflects a diaphragm to strain a strain gauge, or an optical fiber Bragg grating.

A schematic illustrating the common functions of systems for data acquisition from multiple, diverse sensors, including alternatives for multiplexed sensor data communication.

The second class of functions converts the fundamental analog input to an analog output (AIn-AOn) appropriate for signal transmission and acquisition, for example, a voltage or specific frequency of light. The third class of functions converts this analog output to a digital output (Aon-DOn), a basic function of modern a signal acquisition systems enabling further automated processing of the IISS output data (DOn) by the DHM system. These are proposed as the fundamental functional building blocks of any DHM IISS.

Furthermore, if the selection and implementation of the IISS functions are appropriate, the “digital output” originating from multiple sensors can be transmitted using a common, standardized protocol to the DHM signal acquisition and processing functions over a single multiplexed digital data bus.

If the selection and implementation of the first two functions are compatible, “analog output” originating from multiple sensors can be transmitted in a standardized format via a frequency and/or time division multiplexed channel (e.g., optical fiber or wireless analog signals sharing a common transmission medium).

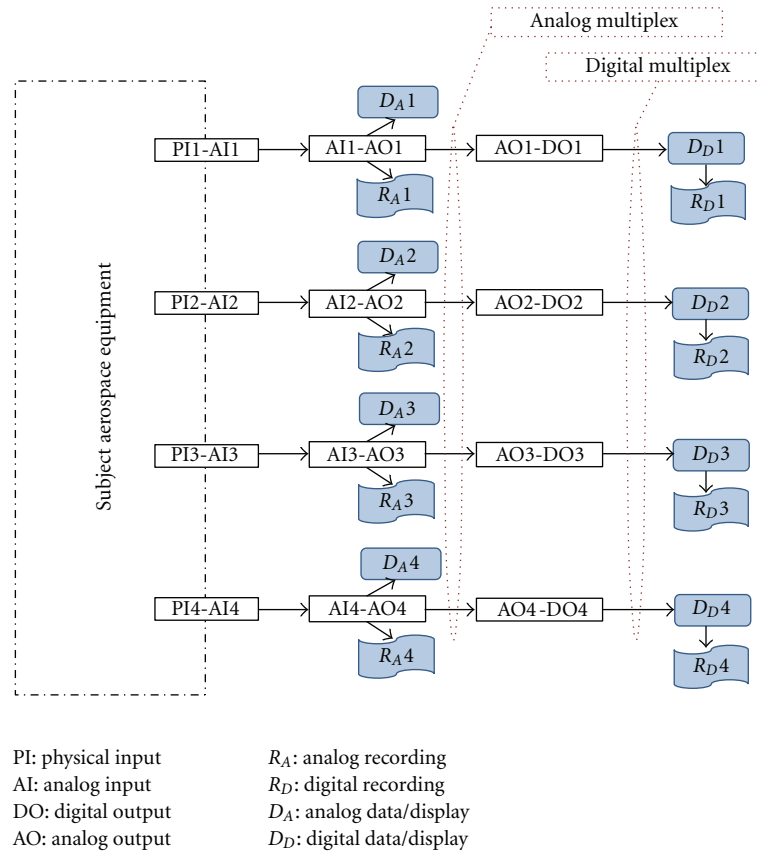


FIGURE 2: Generic functional architecture for DHM IISS.

4.2. *Architectural Alternatives.* The more common alternative is the standardization and multiplexed transmission of the digital outputs. This functional architecture is almost essential for state of the art DHM, where data bus based architectures for digital data transmission are the norm. However, for many aerospace applications the sensor environment and space constraints require placing the analog output signal acquisition, digital conversion, and further processing in an avionics bay or other protected environment removed from the equipment being monitored and the embedded sensors. This typically requires communication of analog sensor output over a multiplicity of dedicated channels feeding dedicated signal acquisition subsystems, curtailing the desired benefits of digital signal multiplexing: reliable, lighter, unobtrusive, and economical interconnections.

A distributed physical architecture, where the analog to digital conversion and signal multiplexing function is allocated to embedded “smart sensors,” appears highly desirable. However this alternative is constrained by the environmental limitations of conventional silicon based digital electronics. Work is in progress to demonstrate a cost effective and suitable capability exploiting high temperature qualified electronic components, (see Millar and Tulpule [9] for one example).

A second architectural alternative exploits standardized analog output signals to attain the benefits of multiplexed signal transmission at this interface, as exemplified by applications of optical fiber Bragg gratings where multiple fiber optic sensors are interrogated by over a single optical fiber. (See Abad [10]). This alternative architecture requires sensors (preferable unpowered transducers) designed to conform to standardized analog outputs (electrical, optical, or radio frequency) communicated over a common transmission medium using time or wavelength division multiplexing for acquisition by a common signal acquisition channel. This is attractive in both reducing the size and complexity of harnesses and limiting the number and variety of signal acquisition interfaces and devices.

The second architecture puts severe constraints on the analog output, and demands innovation in sensor design to suit a common interface. The design disclosed in Millar [11], for example, requires that all sensors are designed such that diverse sensed physical parameters strain an optical fiber Bragg grating or otherwise modify its optical characteristics in compliance with a defined common standard, so all results can be read out with a single optoelectronic signal acquisition subsystem.

However, the latter approach is an attractive option for aerospace environments and applications where the cost,

volume, complexity, and immaturity of robust smart sensors would otherwise put the desired benefits out of reach. (Designing sensor suites to standard analog outputs alone would enable some of the features proposed below, but the ability to multiplex the sensor analog output is necessary to radically address suitability and life cycle cost objectives).

4.3. Features Addressing Suitability and Life Cycle Cost Objectives. In general, the implication of the suitability and life cycle cost [LCC] driven objectives for integrated instrumentation/sensor system design is to make the sensors “smart” by moving the sensor specific (AOn) interface as close as possible to the sensed parameter, without compromising the sensor performance objectives. Distributed systems with standardized multiplexed interfaces at the sensor location should reduce the weight, complexity, and cost of interconnections and facilitate IISS modification in response to sensor requirements changes or capability improvements.

If the standard interface is “open,” to a public specification, system capability will increase and LCC will reduce as suppliers compete to provide improved sensors meeting the standard interface, for both existing measurements and novel sensor requirements.

A capacity to support multiplexed communication will yield gains in cost and compatibility, particularly if it allows a single (smaller and less complex and costly) signal acquisition unit to interrogate multiple sensors. A variety of communication network architectures become viable, allowing optimization for enhanced system reliability and reconfiguration on the fly. As noted above, multiplexing the “analog outputs” of the sensors is the more attractive option as it may eliminate a multiplicity of differentiated signal acquisition channels. Appropriate standardization of the analog output communication protocol would enable “plug and play” sensor interchangeability, enhancing IISS adaptability to emerging DHM requirements.

Another desirable feature would be functionality for automated sensor identification (type and item) and characterization, avoiding the onerous signal tracing of conventional instrumentation, and alleviating the high costs of manufacturing sensors with effectively identical calibrations. Embedded identification and calibration (or classification) data interrogated over the signal acquisition network would be ideal, allowing plug and play sensor addition, configuration management, and interchange on the network. The non-volatile memory function implied by this requirement might also be used to store usage, fault and system configuration data to guide maintenance.

A further desirable characteristic is a technology base shared by current and future applications in other fields, preferably ones with commercial markets that can contribute to financing technological maturation and add production volume for common components. These alternative markets would then share in recovering the sensor system investments. For example, wireless and optical fiber technology spun off from communications industry applications is a resource for development of analog multiplexed IISS.

5. Conclusions and Recommendations

The schematic DHM IISS functional framework presented is a useful tool to categorize alternative DHM IISS approaches. Within this framework, it will be fruitful to identify a variety of compatible implementations for each function, for example, generation of suitable pairings of analog inputs and common analog multiplex output protocols from optical fiber sensors measuring diverse physical inputs. Morphological variations on these options could be used to identify promising design alternatives for DHM IISS.

A variety of design approaches implementing the second alternative functional architecture—standardized multiplexed analog sensor outputs—have been defined and are in the early stages of feasibility demonstration and development. Six years ago, Mrad and Xiao [12] pointed out a key technology hurdle for aerospace optical fiber sensor systems: the need for robust optoelectronic signal acquisition. Luna Innovations Inc. [13] recently completed a US Navy Ph. II SBIR contract addressing this requirement.

Fonseca et al. [14] early demonstrated multiple pressure transducers responding to microwave interrogation, and Environetix [15] offered temperature sensors using a similar principle. Recent Navy SBIR topics exploring the potential of multiplexed analog signals are also bearing fruit. Gregory et al. [16] describe a SBIR project exploiting a wireless transducer concept applicable to a variety of sensor types which will allow numerous sensors in a gas turbine hot section to be wirelessly interrogated by a single signal acquisition unit. Syntonics LLC [17, 18] is developing a novel surface acoustic wave (SAW) wireless transducer with multiple sensor capabilities for use up to 750 deg. C.

Further effort to investigate the feasibility of, and develop, such innovative technological approaches is a promising route to more suitable and cost effective DHM IISS. In defining and evaluating such approaches, the desirable features described in the previous section should be considered. In general, the systems engineering approach provided clear benefits in defining user significant IISS system requirements and an architectural framework for categorizing, identifying, and evaluating alternative architectures, relative to a bottom up focus on sensor technology not addressing system level user needs.

Nomenclature

CBM: Condition Based maintenance
 DHM: Diagnostics and health management
 IISS: Integrated instrumentation/sensor systems
 LCC: Life cycle cost
 RCM: Reliability centered maintenance
 SBIR: Small business innovation research.

Acknowledgment

The work reported here was performed for the Office of Naval Research, under the direction of Dr. Joseph Doychak. It is published here under the authority of Office of Naval Research Public Release Case no. 43-037-11.

References

- [1] L. A. Urban, "Gas path analysis applied to turbine engine conditioning monitoring," in *Proceedings of the AIAA Joint Propulsion Conference*, December 1972, Paper 72-1082.
- [2] J. S. Litt, D. L. Simon, S. Garg et al., "A survey of intelligent control and health management technologies for aircraft propulsion systems," *Journal of Aerospace Computing, Information and Communication*, vol. 1, no. 12, pp. 543–563, 2004.
- [3] D. E. Paris, L. C. Trevino, and M. D. Watson, "A framework for integration of IVHM technologies for intelligent integration for vehicle management," in *Proceedings of the IEEE Aerospace Conference*, March 2005.
- [4] A. M. Madni, "Smart configurable wireless sensors and actuators for industrial monitoring and control," in *Proceedings of the 3rd International Symposium on Communications, Control, and Signal Processing (ISCCSP '08)*, pp. 447–448, March 2008.
- [5] A. Behbahani, R. C. Millar, and B. Tulpule, "Vision for next generation Modular Adaptive Generic Integrated Controls (MAGIC) for military/commercial turbine engines," in *Proceedings of the AIAA Joint Propulsion Conference*, pp. 6921–6932, July 2007, paper no 007-5710.
- [6] D. E. Culley and A. Behbahani, "Communication Needs Assessment for Distributed Turbine Engine Control," NASA/TM-2008-215419, 2008.
- [7] B. Tulpule, A. Behbahani, and R. Millar, *Vision for Next Generation Modular Adaptive Generic Integrated Controls (MAGIC) for Military/Commercial Turbine Engines*, American Institute of Aeronautics and Astronautics, 2007.
- [8] X. Xu, Q. Liu, and G. Wu, "Restudying on the concept, mechanism and composition of instrumentation flexible developing system," in *Proceedings of the 9th International Conference on Electronic Measurement and Instruments (ICEMI '09)*, pp. 3269–3274, August 2009.
- [9] R. C. Millar and B. Tulpule, "Intelligent sensor node as an approach to integrated instrumentation & sensor systems for aerospace systems control," in *Proceedings of the AIAA Infotech at Aerospace*, St. Louis, Mo, USA, March 2011.
- [10] S. Abad, "Fiber Bragg grating sensor applications for thermal monitoring in satellites," in *Proceedings of the International Conference of Space Optics*, Toulouse, France, October 2008.
- [11] R. C. Millar, Patent No. 7, 091, 472 B1, USA, 2006.
- [12] N. Mrad and G. Z. Xiao, "Multiplexed fiber bragg gratings for potential aerospace applications," in *Proceedings of the International Conference on MEMS, NANO and Smart Systems*, pp. 359–363, 2005.
- [13] Luna Innovations Inc., "SBIR N06-121, Open Architecture Fiber Optic Engine Monitoring System," 2010, http://www.navysbir.com/06_2/14.htm.
- [14] M. A. Fonseca, J. M. English, M. von Arx, and M. G. Allen, "Wireless micromachined ceramic pressure sensor for high-temperature applications," *Journal of Microelectromechanical Systems*, vol. 11, no. 4, pp. 337–343, 2002.
- [15] Anon, "Passive Wireless Sensor Systems for Harsh Environments, Environetics Technology Corporation," 18 July 2011, http://www.environetix.com/files/Environetix_Wireless_Harsh_Environment_Sensors_and_Systems.pdf.
- [16] O. Gregory, J. Conkle, and T. Birnbaum, "Wireless temperature sensor for gas turbine engine applications," in *Proceedings of the 56th International Instrumentation Symposium*, pp. 177–200, Rochester, Vt, USA, May 2010.
- [17] Syntronics LLC and SBIR N08-037, "High Temperature Sensing Parameters," 2010, http://www.navysbir.com/08_1/103.htm.
- [18] J. B. Friedlander, *Wireless strain measurement with surface acoustic wave sensors [M.S. thesis]*, Graduate School of The Ohio State University, 2011.

Research Article

Assessment of Combustor Working Environments

Leiyong Jiang and Andrew Corber

Aerospace Research, Gas Turbine Laboratory, The National Research Council of Canada, 1200 Montreal Road, M-10, Ottawa, ON, Canada K1A 0R6

Correspondence should be addressed to Leiyong Jiang, leiyong.jiang@nrc-cnrc.gc.ca

Received 10 March 2012; Accepted 29 June 2012

Academic Editor: Victor Giurgiutiu

Copyright © 2012 L. Jiang and A. Corber. This is an open access article distributed under the Creative Commons Attribution License, which permits unrestricted use, distribution, and reproduction in any medium, provided the original work is properly cited.

In order to assess the remaining life of gas turbine critical components, it is vital to accurately define the aerothermodynamic working environments and service histories. As a part of a major multidisciplinary collaboration program, a benchmark modeling on a practical gas turbine combustor is successfully carried out, and the two-phase, steady, turbulent, compressible, reacting flow fields at both cruise and takeoff are obtained. The results show the complicated flow features inside the combustor. The airflow over each flow element of the combustor can or liner is not evenly distributed, and considerable variations, $\pm 25\%$, around the average values, are observed. It is more important to note that the temperatures at the combustor can and cooling wiggles vary significantly, which can significantly affect fatigue life of engine critical components. The present study suggests that to develop an adequate aerothermodynamics tool, it is necessary to carry out a further systematic study, including validation of numerical results, simulations at typical engine operating conditions, and development of simple correlations between engine operating conditions and component working environments. As an ultimate goal, the cost and time of gas turbine engine fleet management must be significantly reduced.

1. Motivation

It is a promising approach to assess the remaining life of gas turbine critical components, based on their service history (flight operating conditions and sensor readings), by applying aerothermodynamics, structural and material analysis models. It is consistent with condition-based maintenance (CBM) of gas turbine engines, that is, maintenance actions would be performed only when they are required. As a result, the expense of maintenance/repair of an engine fleet can be reduced, the engine operation can be made more reliable, and service life can be extended. This approach has been investigated by researchers from various disciplines under a major collaboration program [1].

One of the subprograms is the development of an aero-thermodynamics model. The model will provide more realistic distributions of temperature and pressure or loads for safety/cost critical components from engine operational conditions and sensor readings. Furthermore, it will also provide an environment for the assessment of current and enhanced sensor suites and the prediction of degraded

operation with wear/damage or control changes. With the required thermal flow information, structural and material analyses can be performed, and the remaining life of engine components can be assessed with confidence.

For technology development, a practical gas turbine combustor is selected as a research case. Gas turbine combustors are exposed to high-temperature, high-pressure, and high-dynamic load environments, and failures occasionally occur during operation. The flow parameters around and inside the combustor vary significantly, which causes considerably uneven structural stresses. Increased localized metal temperatures and thermal gradients can both reduce the combustor fatigue life. A higher temperature reduces the fatigue strength of the material, while a larger gradient increases the strain excursion and causes higher stresses. Therefore, for reliable structural, material and life analyses, the accurate definition of the working environment for the combustor is deemed necessary.

Due to the harsh conditions, experimental measurements inside the engine are extremely difficult. An alternative is to use validated computational flow dynamics (CFD) methods

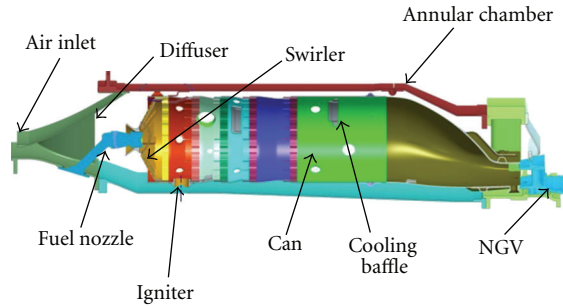


FIGURE 1: A 60-degree sector.

to document typical operating conditions and then correlate these detailed numerical results with the engine operating conditions and sensor readings to form semiempirical models. These models can be used for engine component life analysis or an essential component of CBM for engine fleet management.

This paper covers a high-fidelity CFD model of the gas turbine combustor, complex flow fields inside the combustor, temperature and pressure distributions over the combustor can as well as indications or suggestions from the present study.

2. Thermal Fluid Dynamics Modeling of the Combustor

2.1. High-Fidelity CFD Model of the Combustor. Figure 1 illustrates a 60-degree sector of the gas turbine combustor. It is a can-annular design with six combustion cans and an annular air supply chamber [2]. Compressed air enters the annular chamber through a narrow annulus, decelerates in the diffuser, and then flows over and enters the combustor can or liner through air-management holes and cooling wiggly strips around the can. Inside the can, fine fuel droplets from a fuel nozzle evaporate, mix with air, and then burn. The mixture continues to react with air, cools down further downstream, and eventually reaches the air-cooled nozzle guide vanes (NGVs). For the present phase of work, the NGV is not included in the CFD model.

For traditional numerical simulations of gas turbine combustors, the computational domain is limited to the flow field inside the combustor liner, that is, the liner internal and external flow fields are decoupled. The airflow-splitting over the combustor liner is estimated based on semi-empirical discharge coefficient correlations [3, 4] and the flow rate is assumed evenly distributed over each liner airflow device (a row of holes, a wiggly strip, etc.). In the present study, both the liner internal and external flow fields are simulated simultaneously, that is, they are directly coupled.

Two engine operating conditions, takeoff and altitude cruise [2], are considered in the present study and the flow parameters for a single can are listed in Table 1.

2.2. Fuel Spray Measurements at the GTL High-Pressure Spray Rig. The temperature field in a combustor is dominated by

TABLE 1: Engine operating conditions.

		Flow parameters	
Takeoff	Air inlet total pressure (kPa)	1000	
	Air mass flow rate (kg/s)	2.36	
	Air inlet temperature (K)	606	
	Fuel mass flow rate (kg/s)	0.053	
Cruise	Air inlet total pressure (kPa)	463	
	Air mass flow rate (kg/s)	1.17	
	Air inlet temperature (K)	552	
	Fuel mass flow rate (kg/s)	0.0207	

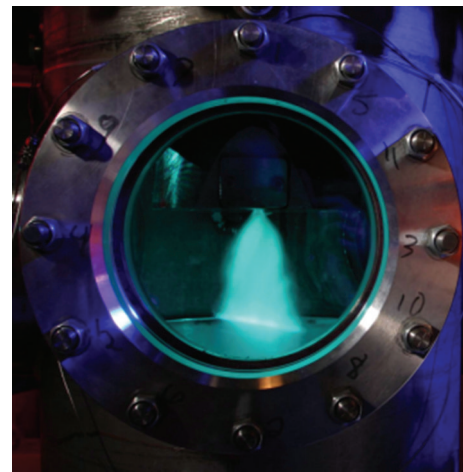


FIGURE 2: Fuel spray measurements in the GTL HPSR.

the fuel distribution and arrangement of primary, cooling and dilution air [5]. Therefore, it is essential to have proper fuel spray parameters in order to predict the combustor flow field accurately. The fuel spray characteristics were measured in the GTL (Gas Turbine Laboratory) High-Pressure Spray Rig (HPSR) with a phase Doppler particle analyzer (PDPA), as shown in Figure 2, at the engine cruise and takeoff conditions. Figure 3 gives a picture of the fuel spray in an air box which is the domed portion of the combustor can.

During spray measurement, the air and fuel flow rates remained the same as the flight conditions, and the pressure in the HPSR was adjusted to match the air density at flight. The measured parameters included the radial distributions of axial, tangential, and radial velocities, droplet size as well as fuel flux. All these results were used as the initial conditions of fuel spray for the predictions of the combustor thermal fields.

2.3. Mesh-Independent Studies and Combustor Mesh. Due to the geometrical complexity of practical gas turbine combustors, it is difficult to fully meet mesh-independence requirements. Researchers, such as [6], have pointed out that a gas turbine combustor simulation would need 410 million cells in order to claim mesh independence. This is understandable, for example, if the rollup of vortices along the bending jet and the structures of horseshoe and wake

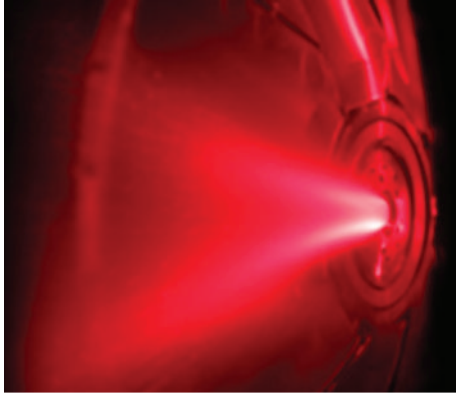


FIGURE 3: The fuel spray in a specifically built air box.

vortices for a single cross-flow jet [7] have to be properly resolved in numerical simulations, the required mesh size can be even larger than 410 million cells. Therefore, the best way to check mesh independence would be to examine if the objectives or required flow parameters remain mesh-independent in simulations.

As mentioned before, the main objective of this work is to obtain accurate temperature and pressure distributions over the combustor can. Since the air distribution over the combustor can directly determines the combustor performance and metal wall temperature, the mesh-independence issues related to liner airflow devices (holes and wiggle strips) were studied first before meshing the whole 60-degree sector. For detail, please refer to [8, 9].

During meshing of the whole geometry, 36–84 surface elements were used for medium and large liner airflow holes. For small holes, such as the splashing holes over the dome swirler plates and cooling baffles (Figure 1), about 30 surface elements were generated. With these arrangements, the area-weighted numerical uncertainty of air distribution over the liner is less than 2%.

For the whole combustor simulation, the wiggle strip was replaced by an equivalent slot which gave the same mass flow rate as that of the wiggle-strip for similar flow conditions. For the purpose of structure/material/life analyses of wiggle strips, the flow field of a single wiggle strip element was resolved with the boundary conditions obtained from the results of whole combustor simulations.

A few meshes were created and preliminary test runs were performed to improve the quality of numerical simulations. In the end, a mesh with 13.3 million cells was used for the simulations. Figure 4 illustrates the meshes of the 60-degree annular chamber (top) and the combustor can (bottom). Efforts were made to generate hexahedral cells as far as possible. Fine nodes were laid in and around holes, cooling slots, baffles, regions, dome swirler, and dome section. The nondimensional wall boundary parameter, y^+ , at the combustor can walls varied from ~ 20 to ~ 250 .

2.4. Flow Fields of the Combustor. A large amount of data is available to reveal complicated flow features and physical

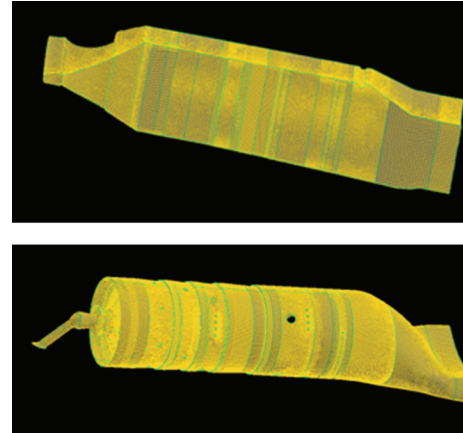


FIGURE 4: Meshes of 60-degree annular chamber and a combustor can.

phenomena inside the combustor [8]. Only some of the results at the cruise conditions are presented here. The flow features at takeoff are similar to those at cruise. Figures 5–7 show the velocity vectors and contours of Mach number and temperature along the middle longitudinal plane of the 60-degree sector of the combustor. In the figures, the thick black lines are the cut-through surfaces of the combustor can and fuel nozzle, and the dimensions and flow parameters are normalized by their representative values.

As shown in the upper plot of Figure 5, the compressed air flows into the annular chamber through a narrow inlet, slows down in the diffuser, and then enters the can dome through the splashing holes on the dome walls. As a result, two large recirculation zones are formed immediately downstream of the dome swirler, and the shape of the lower one is distorted by the igniter (Figure 1). These swirling flows are used to start and anchor flame in the combustor (Figure 7), and at the same time cool the dome head walls. Further downstream, the air flows through cooling slots into the combustion can, and the flow velocity gradually increases towards the can exit, as shown in both upper and lower plots of Figure 5. Another recirculation zone inside the can is also observed adjacent to the two dome recirculation regions. For the annular chamber, due to the geometrical blockage, strong swirling flows are found upstream of the dome, and a mild recirculation zone is observed in the dead flow region above the can exit section.

The Mach number contours at this section are given in Figure 6. In the primary zone of the combustor can (just downstream of the dome swirler), the Mach number or flow velocity is low. This gives enough time for fuel droplets to evaporate, mix and burn with air, and provides good environments for flame stabilization. The Mach number inside the can gradually increases downstream of the dome section and reaches a high value of ~ 0.28 at the can exit. In Figure 6, a maximum Mach number of 0.32 is observed in the diffuser due to the narrow flow passage (Figure 1). Shown in Figure 7 are the temperature contours inside and outside the can. As illustrated in Figures 5 and 6, the flow field is not symmetric, even in the upstream region of the

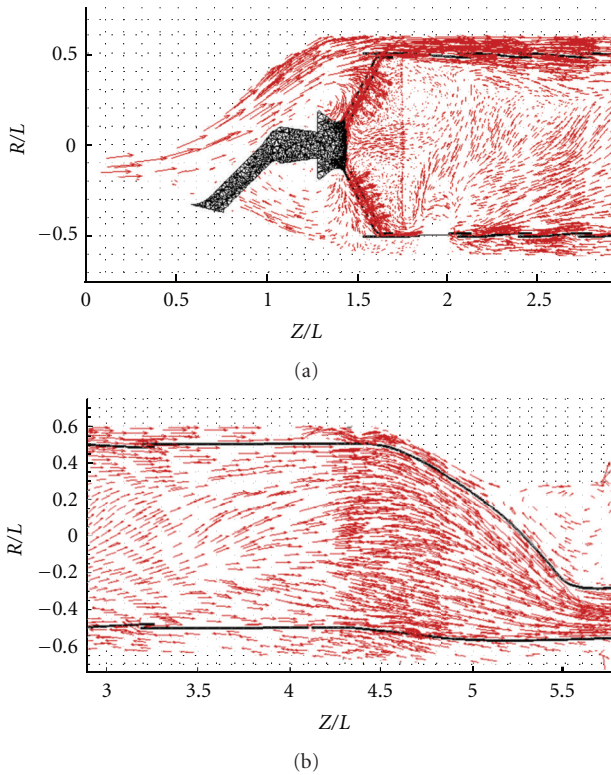


FIGURE 5: Velocity vector plots along the middle longitudinal plane.

combustor can. The high temperature region starts from the dome swirler and extends to the middle of the can with a maximum of ~ 1 . This complies with gas turbine combustor design criteria [5], that is, the high-temperature region should be located in the primary and secondary zones. The low-temperature region in the center immediately downstream of the dome swirler is where the fuel spray is introduced into the flow field.

Figure 8 shows the velocity vector and Mach number plots, while Figure 9 illustrates temperature distribution at a dome swirler cross-section. This section cuts through the dome section, including swirler plates, splashing holes, and can liner wall, as indicated in thick white lines in Figures 8 and 9. There are eight swirler plates with 5 splashing holes for each, and only one hole for each plate is shown in the figures. As shown in Figure 8, the air enters the dome through small splashing holes and forms swirling flow at the plane perpendicular to the combustor axial axis. Referring to the two swirling regions inside the can observed along the longitudinal plane in Figure 5, it is understood that a donut-shaped vortex is formed immediately downstream of the dome swirler. Due to the geometric variation, high Mach number is found in the inner region of the annular chamber. The maximum temperature at this section (Figure 9) is close to that of the whole flow field (Figure 7), as shown in Figure 12, which could cause defects and cracks on the dome swirler [8].

The flow features at the cross-section of the second primary holes are given in Figures 10 and 11. Air enters

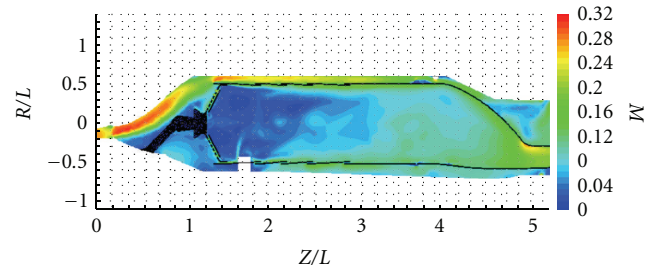


FIGURE 6: Mach number contours along the middle longitudinal plane.

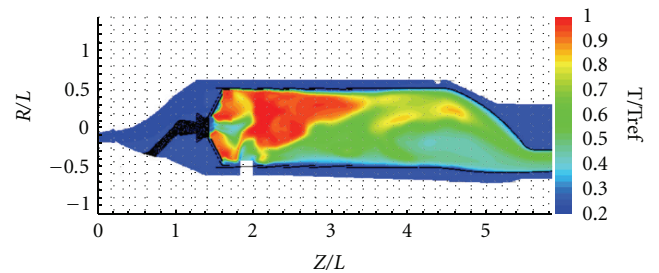


FIGURE 7: Temperature contours along the middle longitudinal plane.

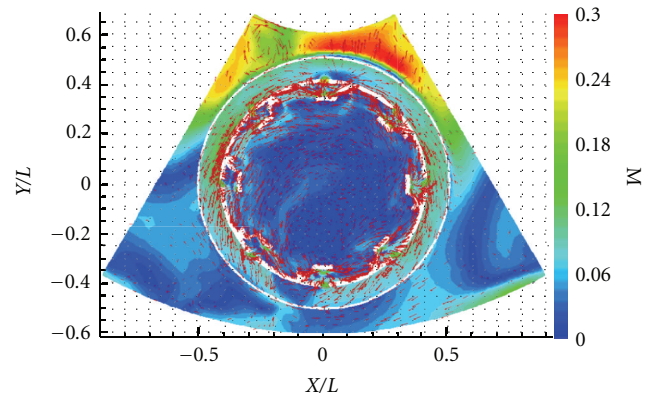


FIGURE 8: Velocity vectors and Mach numbers at a dome swirler cross-section.

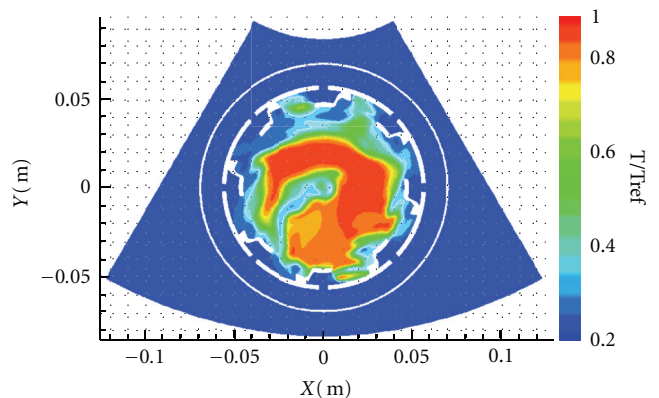


FIGURE 9: Temperature at a dome swirler cross-section.

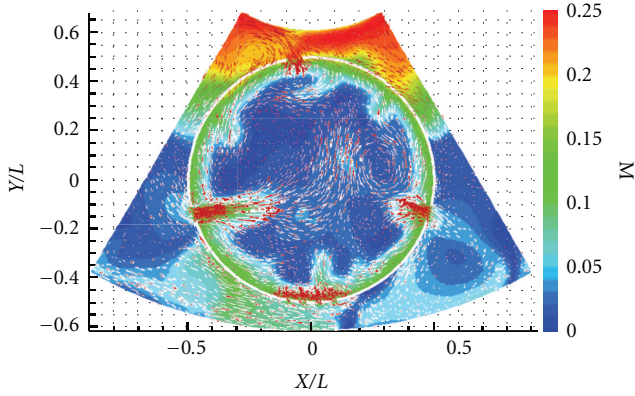


FIGURE 10: Velocity vectors and Mach numbers at the second primary hole section.

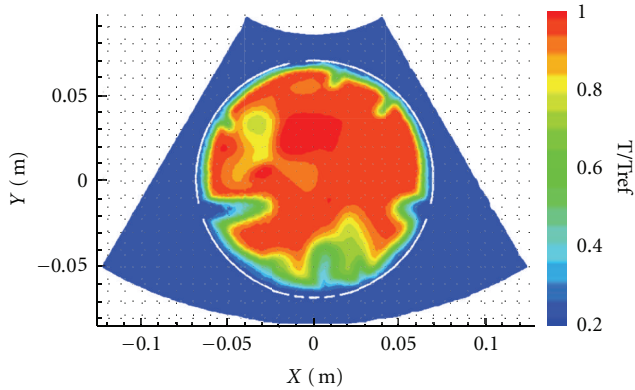


FIGURE 11: Temperature at the second primary hole cross-section.

the combustor can through 3 holes, and two large and two medium swirling regions are observed inside the can. It is important to note that although the size of the three air entry holes is the same, the airflow rate varies significantly, as shown in Figure 10. This is also observed at other liner air entry cross-sections (holes and wobble strips), and the deviation of airflow rate can be as high as $\pm 25\%$.

It is expected that the flow parameters such as flow and liner temperature distributions can be significantly different from those with the even airflow distribution over each cooling device in the traditional decoupled combustor simulations as mentioned earlier. As a result, the accuracy of combustor performance and life assessment can be considerably affected. This observation strongly suggests that for combustor simulations, the flow fields inside and outside the liner should be coupled in order to avoid potential prediction errors. At this primary zone section, the temperature is highest in the combustor flow field, as shown in Figure 11. This is because the combustion process takes place mainly in this zone. In Figures 10 and 11, a cooling baffle with four small splashing holes is displayed, and its cooling effect can be found in Figure 11.

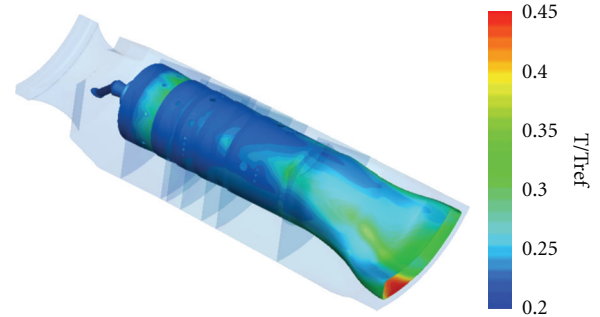


FIGURE 12: Combustor can and dome temperature contours at cruise.

2.5. Combustor Working Environment. Figures 12 and 13 present 3D temperature and absolute static pressure distributions over the combustor can and fuel nozzle at the cruise conditions. The maximum temperature occurs at the bottom left of the can exit. It reaches ~ 0.50 , which is below but close to the allowable temperature for Hastelloy X alloy. As shown in Figure 12, the temperature over the combustor can vary significantly, which can cause considerably uneven structural stresses. As mentioned, increased localized metal temperatures and thermal gradients can both reduce the combustor fatigue life. Therefore, for reliable structural, material, and life analyses, the reliable working environments for engine components are deemed necessary.

The pressure distribution over the can walls is fairly uniform, as indicated in Figure 13. For the current combustor case, the pressure difference inside and outside the liner is minor, and therefore the pressure effect on the combustor life is probably insignificant in comparison with temperature. The detailed temperature distribution over the wobble-strip element is illustrated in Figure 14 for cruise. The maximum temperature reaches ~ 0.288 .

These detailed 3D temperature and pressure distributions over the combustor can and wobble-strip element will be used for structural, material and life analyses of the combustor. It is expected that the critical or representative regions and/or parameters for the life analysis would be



FIGURE 13: Combustor can pressure contours at cruise.

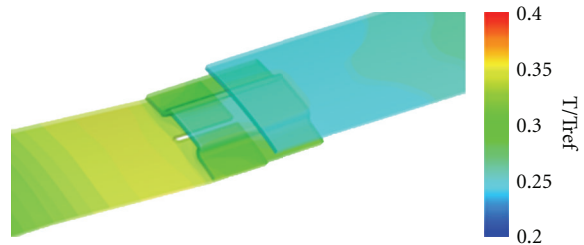


FIGURE 14: Temperature distribution over wiggly strip element at cruise.

identified, which may help the development of a simple aerothermodynamics model. This model should be able to correlate the engine operating conditions/sensor readings with the working environments of engine critical components.

3. Conclusions and Future Work

To be able to reduce the cost of gas turbine engine fleet management, extend their service time, and perform maintenance actions only when they are required, it is vital to provide reliable aero-thermodynamic loads for the engine critical components.

As a first phase of the development of an aerothermodynamics model, the benchmark modeling on a practical gas turbine combustor is successfully carried out, and the two-phase, steady, turbulent, compressible, reacting flow fields at the cruise and takeoff conditions are obtained. The complicated flow features inside the combustor are observed. More importantly, the present study indicates that the airflow over each liner flow device is not evenly distributed, and $\pm 25\%$ variations around the average values are observed. These findings suggest that the coupled combustor simulation should be performed.

The detailed 3D temperature and pressure distributions over the combustor can and wiggly-strip element at the engine cruise and takeoff conditions are available for structural, material, and life analyses. It is expected that the critical or representative regions and/or parameters would be identified for the development of a simple aerothermodynamics model, which can correlate the engine operating conditions/sensor readings with the working environments of engine critical components.

The present study also indicates that it is necessary to carry out a further systematic study in order to develop an adequate aero-thermodynamics model. The on-going and future activities should include validation of numerical results, simulations at typical engine operating conditions, and development of simple correlations between engine operating conditions and component working environments.

Acknowledgments

The authors are grateful to the Department of National Defence and the Canadian Forces as well as the National Research Council Gas Turbine Laboratory for funding and supporting this collaborative research project. The technical authorities and project managers at DND and NRC, Mr. Ken McRae and Mr. Jeff Bird, respectively are gratefully acknowledged.

References

- [1] J. Bird, M. Mrad, X. Wu, and C. Yang, "Propulsion System Mission and Maintenance Planning Demonstrator," LTR-GTL-2010-0092, The National Research Council of Canada.
- [2] V. L. Oechsle, P. T. Ross, and H. C. Mongia, "High density fuel effects on gas turbine engines," Tech. Rep. AIAA-87-1829, San Diego, Calif, USA, 1987, AIAA/SAE/ASME/ASEE 23rd Joint Propulsion Conference.
- [3] P. J. Stuttaford and P. A. Rubini, "Preliminary gas turbine combustor design using a network approach," *Journal of Engineering for Gas Turbines and Power*, vol. 119, no. 3, pp. 546–552, 1997.
- [4] R. C. Adkins and D. Gueroui, "An improved method for accurate prediction of mass flows through combustor liner holes," Tech. Rep. GT86-149, Duesseldorf, Germany, 1986.
- [5] A. H. Lefebvre and D. R. Ballal, *Gas Turbine Combustion*, Taylor and Francis Group, 2010.
- [6] H. C. Mongia, "Recent advances in the development of combustor design tools," Tech. Rep. AIAA-2003-4495, Huntsville Alabama USA, 2003, AIAA/SAE/ASME/ASEE 39th Joint Propulsion Conference.
- [7] M. Samimy, K. S. Breuer, L. G. Leal, and P. H. Steen, *A Gallery of Fluid Motion*, Cambridge University Press, Cambridge, UK, 2003.
- [8] L. Y. Jiang and A. Corber, "Benchmark Modeling of T56 Gas Turbine Combustor—phase I, CFD model, flow features, air distribution and combustor can temperature distribution," LTR-GTL-2010-0088, The National Research Council of Canada, 2011.
- [9] L. Jiang, "Combustor cooling wiggly strip and geometrical simplification," in *Proceedings of the International Mechanical Engineering Congress and Exposition (IMECE '08)*, pp. 177–184, November 2008.

Research Article

Corrosion Sensor Development for Condition-Based Maintenance of Aircraft

**Gino Rinaldi,¹ Trisha Huber,² Heather McIntosh,³ Les Lebrun,³
Heping Ding,³ and John Weber³**

¹NRC Institute for Aerospace Research, National Research Council Canada, Building M-14, Ottawa, ON, Canada K1A 0R6

²Dockyard Laboratory Pacific, Defence Research & Development Canada-Atlantic, CFB Esquimalt D199,
P.O. Box 17000, Station Forces, Victoria, BC, Canada V9A 7N2

³NRC Institute for Microstructural Sciences, National Research Council Canada, Building M-50, Ottawa, ON, Canada K1A 0R6

Correspondence should be addressed to Gino Rinaldi, gino.rinaldi@nrc-cnrc.gc.ca

Received 19 February 2012; Accepted 10 April 2012

Academic Editor: Peter Foote

Copyright © 2012 Gino Rinaldi et al. This is an open access article distributed under the Creative Commons Attribution License, which permits unrestricted use, distribution, and reproduction in any medium, provided the original work is properly cited.

Aircraft routinely operate in atmospheric environments that, over time, will impact their structural integrity. Material protection and selection schemes notwithstanding, recurrent exposure to chlorides, pollution, temperature gradients, and moisture provide the necessary electrochemical conditions for the development and profusion of corrosion in aircraft structures. For aircraft operators, this becomes an important safety matter as corrosion found in a given aircraft must be assumed to be present in all of that type of aircraft. This safety protocol and its associated unscheduled maintenance requirement drive up the operational costs of the fleet and limit the availability of the aircraft. Hence, there is an opportunity at present for developing novel sensing technologies and schemes to aid in shifting time-based maintenance schedules towards condition-based maintenance procedures. In this work, part of the ongoing development of a multiparameter integrated corrosion sensor is presented. It consists of carbon nanotube/polyaniline polymer sensors and commercial-off-the-shelf sensors. It is being developed primarily for monitoring environmental and material factors for the purpose of providing a means to more accurately assess the structural integrity of aerospace aluminium alloys through fusion of multiparameter sensor data. Preliminary experimental test results are presented for chloride ion concentration, hydrogen gas evolution, humidity variations, and material degradation.

1. Introduction

Metals are vulnerable to corrosion due to environmental factors, and in the majority of cases engineering-grade metals and alloys are selected based on design and functionality priorities: strength, light-weight, mechanical and electrical properties, and so forth, rather than corrosion resistance per se [1]. Unfortunately, the cost of corrosion has a substantial impact on the economies of all nations with the United States spending approximately \$437 billion annually for corroded infrastructure maintenance and replacement [2].

This costing trend is increasing because aircraft are exposed to service operating environments that negatively impact their long-term durability. This is an on-going design, materials selection, and maintenance scheduling issue whose combined neglect or oversight can lead to a shortened life cycle or catastrophic failure of the aircraft [3, 4]. For aircraft,

the effects of corrosion damage are cumulative and can increase in severity if the damage is not detected early. A serious result of undetected corrosion is that it can have a cascading effect by which it can precipitate and accelerate fatigue damage [5] leading to a corresponding decrease in the load bearing capacity for that structure. In this respect, the structural integrity of the aircraft is undermined by two separate yet complicit factors. Corrosion damage occurs slowly, insidiously, and often out of sight. In the short term, it may represent only a small part of the total maintenance cost of a short-life aircraft; however, due to its cumulative nature, corrosion damage-based maintenance expenses will inflate to a substantial amount the ownership cost of a long-life aircraft at retirement [6].

Due to the extreme environments often encountered in military and search-and-rescue (SAR) air operations, these types of aircraft are often flown in conditions that can

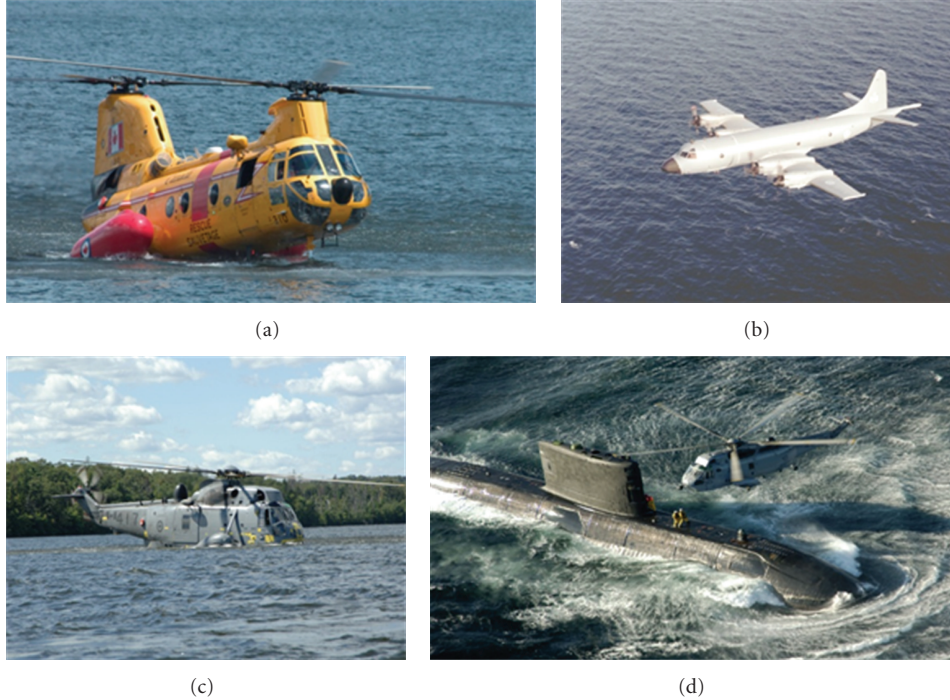


FIGURE 1: (a) an CH-113 “Labrador” search-and-rescue helicopter during a training exercise; (b) an CP-140 “Aurora” aircraft on patrol; (c) an CH-124 “Sea King” helicopter during water-bird training; (d) an CH-124 “Sea King” helicopter rendezvousing with HMCS Windsor.

be considered to be “pushing their design and operational limits.” As an example, exposure of a few hours to sea water may cause pitting, and if it is not removed, as can happen in hidden or difficult to access areas, it can lead to premature crack nucleation in aircraft components [7]. Also, dissolved chlorides are known to be involved in the penetration of the protective aluminium oxide layer [8]. The combined effects of corrosion and accelerated fatigue due to corrosion will eventually limit the performance and availability of these aircraft. Presented in Figure 1 are images of Canadian Forces and SAR aircraft [9] in various typical operational modes.

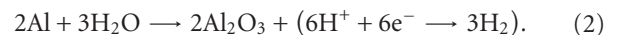
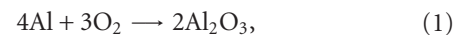
The integrated corrosion sensor development program presented here intends to mitigate these consequences by providing a condition-based approach to aircraft maintenance protocols through a data-intensive maintenance scheduling methodology. The primary aim is to trim maintenance schedules down to actual structural, component or material requirements as opposed to operating under predefined inspection timetables. Presented in Figure 2 is a schematic of various factors involved in the corrosion process. Using data fusion, these factors will determine a corrosion index, which in turn will determine the condition-based maintenance (CBM) protocol. Figure 3 shows a proposed breakdown of the CBM into preventative and corrective protocols as a function of the corrosion index.

2. Aluminium Corrosion Chemistry in Aqueous Solution

2.1. Aluminium Oxide Passivation Layer. Aluminium is only workable from an engineering point of view because of the

existence of a natural aluminium oxide (Al_2O_3) protective layer, without which it would react violently. Aluminium reacts quickly with any available oxygen source to immediately form Al_2O_3 . This thin layer inhibits chemical interaction between bare aluminium and the local environment. However, aqueous solutions carrying anionic species can diffuse through Al_2O_3 and lead to corrosion [10]. The corrosion process of aluminium (Al) in aqueous solutions involves a combination of several factors: (i) moisture; (ii) anionic concentration (chloride); (iii) pH of the solution; (iv) temperature [11, 12].

The protective reactions, in air and water, respectively, are given as



Equation (2) indicates that the reaction of Al with water (H_2O) will also release hydrogen gas (H_2).

2.2. Oxidation Reduction. The oxidation reaction of Al (in H_2O) is given by [13]:



Trivalent Al ions (Al^{3+}) readily bind with chloride (Cl^-) and hydroxide (OH^-) ions present in the solution, and this bonding competition either leads to continued degradation of the Al_2O_3 layer or its regeneration, respectively.

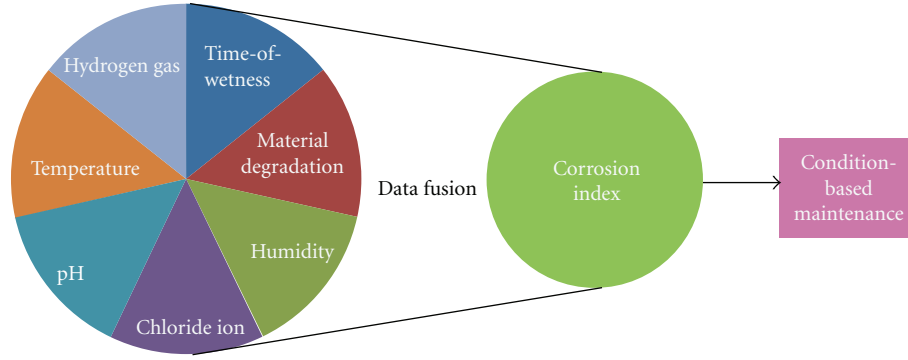


FIGURE 2: An overview of the proposed sensor nodes.

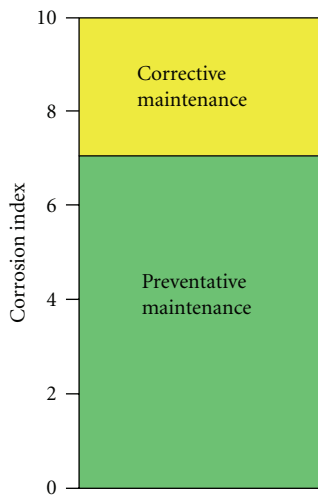
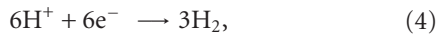
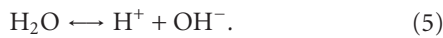


FIGURE 3: A sample CBM scheme based on an environmental factor derived corrosion index.

The above reaction is electrochemically balanced by a corresponding reduction reaction given by [13]:



where the hydronium (H^+) ions are a result of the dissolution of H_2O given by



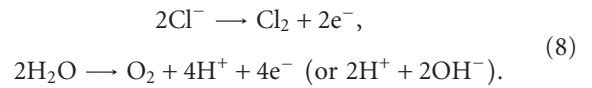
Generally, the dissolution of Al in water is the sum of the oxidation and reduction reactions, as given by (3) and (4):



Employing (5) and (6), the dissolution of Al with water results in the formation of aluminium-hydroxide ($\text{Al}(\text{OH})_3$) and the release of H_2 and is given by [8, 14, 15]:



2.3. *Chloride-Based Aqueous Solution.* Chloride enters the aqueous solution through the absorption of gaseous hydrochloric acid or an organic gas containing chlorine or through the deposition of sea salt [16]. For chloride-based solutions, the oxidation/reduction reactions would involve the following [17]:



As more and more Cl^- is adsorbed, repair of the Al_2O_3 layer is no longer possible, and corrosion proceeds rapidly [12, 18]. This process is shown schematically in Figure 4(a). Competitive adsorption of Cl^- , or OH^- at Al^{3+} lattice sites will result in either continued dissolution or reoxidization, respectively [18–20]. A sample chain structure for a dissolution complex is shown in Figure 4(b) (adapted from [21]).

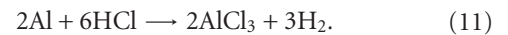
2.4. *Hydrochloric Acid.* Hydrochloric acid represents an aggressive environment for Al, particularly Al alloys [13, 16, 22]. After Al_2O_3 penetration by Cl^- , the dissolution process continues as follows:



where HCl further attacks the Al_2O_3 layer:



which exposes more bare aluminium to HCl and the evolution of H_2 [23]:



When fully corroded, 1 gram of Al will produce 1.245 litres of H_2 gas [23]. The AlCl_3 in (9) can then further react with H_2O to create more HCl (as in (11)), and the dissolution process continues. Of importance, during the corrosion process, H_2 gas creates blisters on the Al surface due to H_2 gas accumulating in microcavities beneath the Al_2O_3 layer, thereby causing structural damage [24].

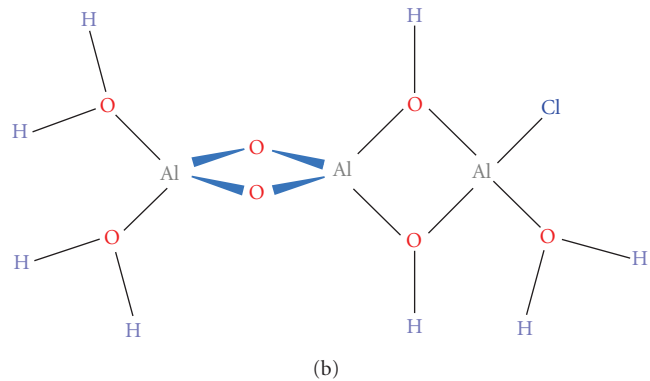
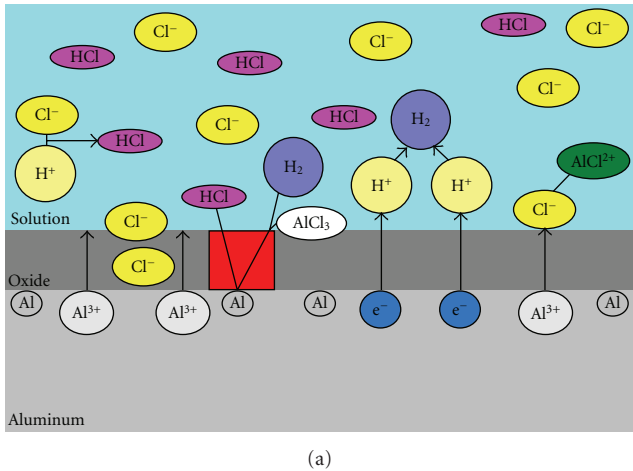


FIGURE 4: (a) breakdown of the aluminium oxide layer in a chloride-based aqueous medium. (b) chain structure showing the bonding of chloride with aluminium at a competition site.

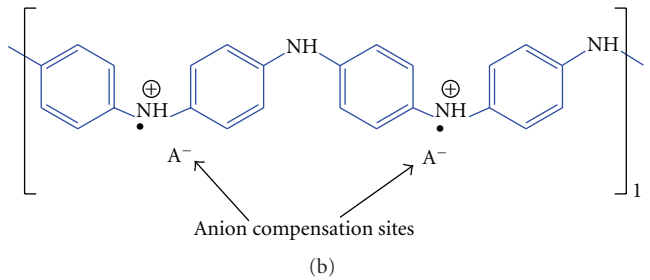
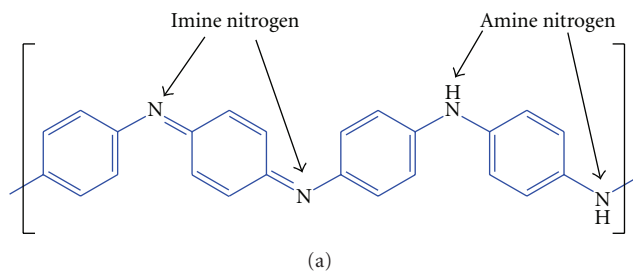


FIGURE 5: Chemical structure for the acid doping of PANI. (a) amine and imine nitrogen sites and (b) acid anion compensation sites.

3. Sensor Node Development

3.1. Hydrogen Gas and Humidity Sensing Nodes: Conducting Polymer-Based Sensing. Conducting polymers become electrically conductive through the addition or removal of π -electrons; however, polyaniline [25] (PANI) is more commonly doped by the addition of an acid. Shown in Figures 5(a) and 5(b) is a sample acid-doped chemical structure of PANI [26, 27]. The electrical conductivity of PANI depends on the size and shape of the acid anion [27], and it may be further enhanced by incorporating carbon nanotubes (CNTs) in the preparation of the polymer [28]. The addition of carbon nanotubes is thought to influence the semiconductor charge carrier mechanism (p -doped or n -doped) in polyaniline. Carbon nanotubes also significantly increase the current output of I - V type tests [29] because CNTs exhibit greater electrical conductivity along their length as compared to conducting polymers, although bulk CNTs do not conduct as well as expected, as the charge transfer is believed to occur by hopping. The conductivity of composites apparently exceeds that of the parent materials alone. This apparent synergy is attributable to the reduction in contact resistance between CNTs by the presence of the conducting polymer. The PANI/CNTs blend can then be readily applied to a sensing platform such as interdigitated

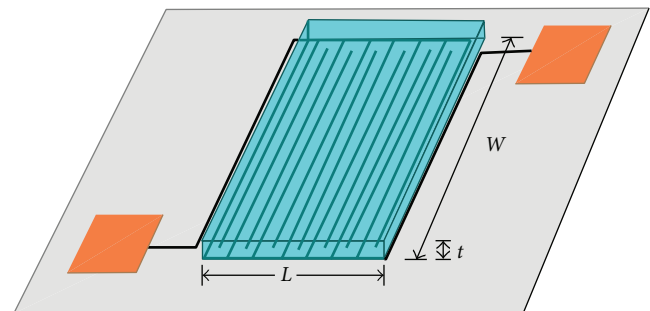


FIGURE 6: Schematic of an IDEs chip with a PANI polymer conductive coating.

electrodes (IDEs). Shown in Figure 6 is a schematic of an IDEs chip coated with PANI/CNTs (not to scale).

3.2. Integrated Chloride Ion, Relative Humidity, and Temperature Sensing Node. The development of this node presents an opportunity for integrating various “corrosion” sensors within the same enclosure. Also, the electronics and the associated computer interface capability being developed in parallel will provide a means that can allow for simultaneous

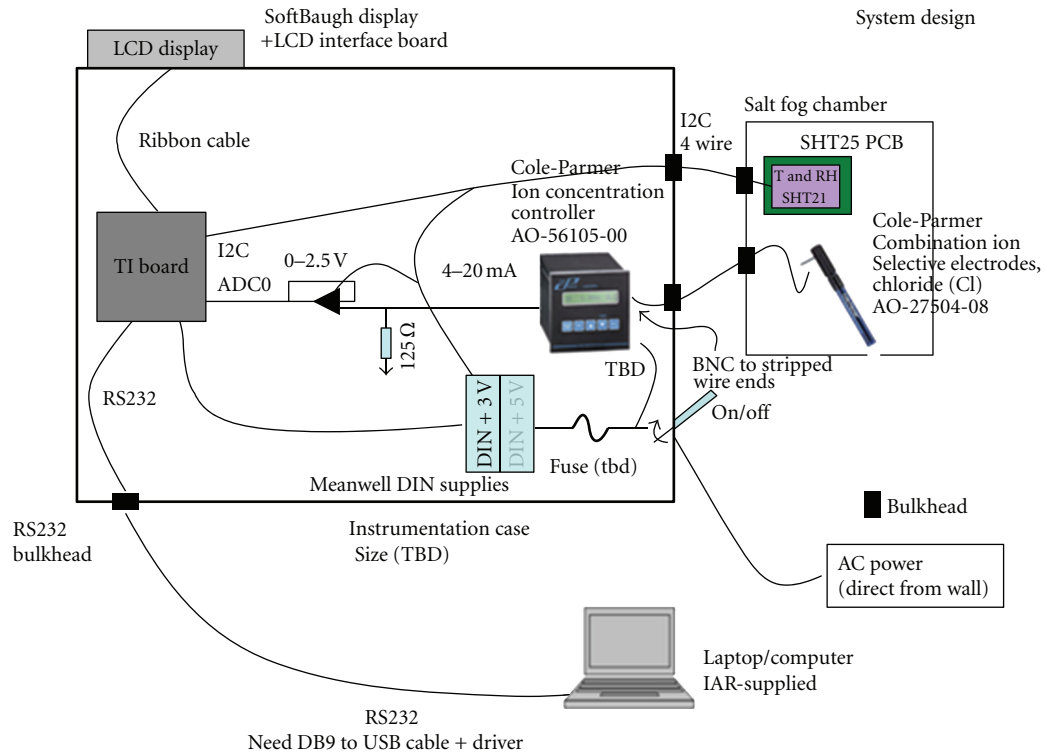


FIGURE 7: An overview of the components of the chloride ion, relative humidity, and temperature sensing node.

data acquisition from the various sensors. At this stage of the corrosion sensor project, it can be considered as a prototype from which refinements in sensor integration, electronics and scaling-down can be developed. This unit consists of COTS chloride ion, relative humidity, and temperature sensors. Currently, the primary components include (i) a chloride ion electrode (Cole-Parmer Instrument Company); (ii) an ion concentration controller that interfaces to the electrode (B&C Electronics IC 7685); (iii) a packaged SHT21 humidity and temperature sensor (Sensirion AG); (iv) an MSP430FG461x/F20xx Experimenter's Board (Texas Instruments). Presented in Figure 7 is an overview of the integrated sensor. The microcontroller communicates with the SHT21 sensor through an I2C bus and reads the chloride ion level detected by the IC 7685 controller through one of its analog inputs (ADC0). The microcontroller platform is MSP430FG4618 (Texas Instruments). The firmware resides in the FLASH memory of the microcontroller device and performs various functions required for detection of chloride ion, temperature, and relative humidity. On power up, the system boots automatically and enters the default mode for detection.

At the current developmental stage of the corrosion sensor project, the microcontroller hardware and firmware are very much underutilized. For example, only one of the eleven available analog inputs is used, and the firmware is often in "sleep" mode. Thus, such a microcontroller system has room to accommodate future extensions such as adding more sensing elements, and more functions. In this respect, the integration of additional features along with size and

weight reductions forms the basis for the next phase of the project.

3.3. Material Degradation Sensing Node. For the material degradation sensing node, an XCorr multiarray sensor (Aginova Inc.) was adopted. This sensor is a 16-element passive electrochemical sensor that does not require any applied voltage for operation (Figure 8(a)). The sensor's 16 elements are designed to measure uniform or localized corrosion through a naturally occurring corrosion-current between anodic and cathodic sites on the metal surface when it is exposed to a corrosive solution. The probe's 16 elements are connected together through a common interface within the electronics (Figure 8(b)). The corrosive aqueous solution creates both cathodic and anodic sites at the elements on the probe head (Figure 8(c)). In this regard, corrosion at anodic sites can develop as on an actual metal surface. The system integrates data from the 16 individual elements and extrapolates both average and maximum yearly corrosion rates (Faraday's Law).

4. Experimental Section

4.1. Polyaniline Preparations. In its finished form, PANI/CNTs blends resemble a dark powder, as shown in Figure 9(a). In this state, it cannot be employed directly for sensing applications but must be dispersed in a suitable solvent in order to apply it to a sensor surface such as IDEs. In this work, two types of metallic IDEs (Synkera Technologies

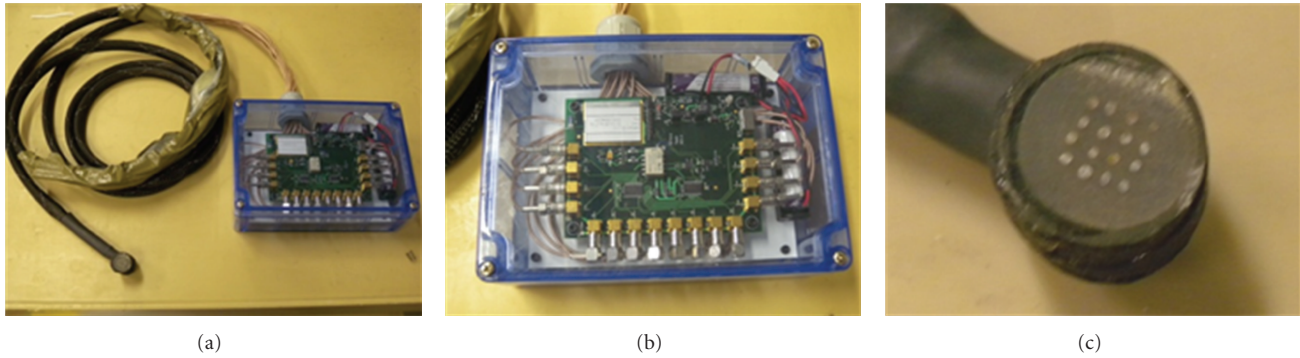


FIGURE 8: (a) XCorr multiarray sensor; (b) encased sensor electronics unit; (c) close-up of the 16 element probe.

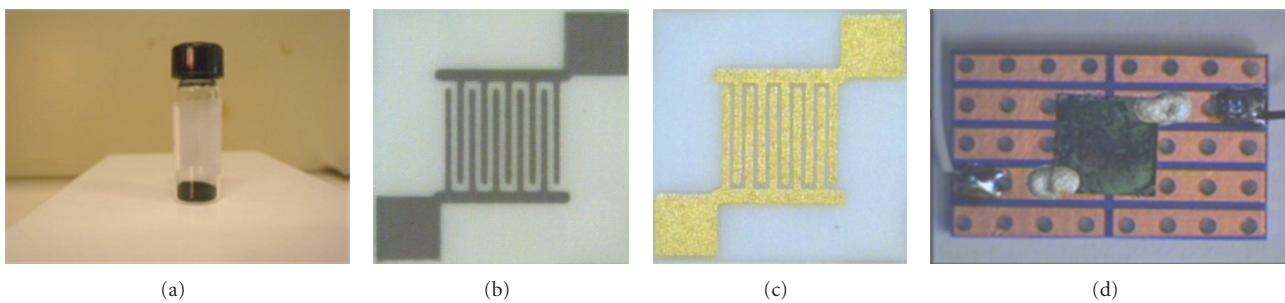


FIGURE 9: (a) PANI/CNTs ‘powder;’ (b) platinum IDEs; (c) gold IDEs; (d) IDEs coated with a PANI/CNT blend.

Inc.), platinum (Figure 9(b)) and gold (Figure 9(c)), were employed for hydrogen gas and humidity sensing, respectively. Figure 9(d) shows a platinum $5 \times 5 \text{ mm}^2$ IDEs chip coated with a PANI/CNTs blend. In this figure, the IDEs chip is mounted onto a small electrical bread-board for ease of wiring and handling.

4.1.1. PANI: Hydrogen Gas Sensor Node. Hydrogen sensing using PANI and PANI/CNTs blends has been reported in the literature [30–32]. In this work, camphor sulfonic acid (CSA) was employed as the doping material. The PANI/CSA/CNTs were dispersed in a chloroform solvent (0.040 grams PANI/CNTs powder per mL solvent). The mixture was then placed into a sonication bath for approximately 18 hours in order to obtain a uniform suspension. Small pipettes were used to transfer the solutions, and drop small amounts onto platinum IDEs. Spin-coating (2000 RPM for 1 minute) was used to distribute the solution over the IDEs surface.

4.1.2. PANI: Humidity Sensor Node. Humidity sensing using PANI blends has been reported in the literature [33–35]. In this work, the PANI humidity sensitization was prepared by doping PANI with bis-(2-ethylhexyl) phosphoric acid (HDEHP), toluene, and CNTs. For this preparation, ethanol was employed as a dispersing solvent (0.021 grams PANI/CNTs powder/0.5 mL solvent). The same transfer, sonication, and spin-coating procedures, as described previously, were employed. For humidity sensing, a gold IDEs chip was used.

4.1.3. Electrical Continuity Measurements. The electrical continuity of the deposited polymer was measured by applying a ramp voltage (0–500 mV) across the polymer-coated IDEs and measuring the resulting current. A sample result is shown in Figure 10(a). The equation relating resistance (R), length (L), cross-sectional area (A), and resistivity (ρ) of an electrical conductor is given as

$$R = \frac{\rho L}{A}. \quad (12)$$

Due to the nature of the spin-coating polymer deposition process, L and A can vary between sensors. A sample conductivity curve is shown in Figure 10(b).

Given in Table 1 are the electrical continuity characteristics for the various IDEs/polymer sensors tested. The resistances shown include the contact resistance of the pads, associated wiring, and the particular PANI formulation. For ease of comparison, in this table the conductivity₁₀₀ is a derived value for a polymer thickness of 100 microns.

4.2. Experimental Results

4.2.1. PANI/CSA Hydrogen Sensing. The PANI/CSA-based sensors developed for hydrogen sensing were tested in a dry hydrogen/argon atmosphere. Presented in Figure 11 is an overview of the fully automated gas flow system and electrical interface. Data was acquired in real time and transferred to a PC (not shown). Shown in Figure 12 is a typical response obtained for the hydrogen sensors. It can be seen from

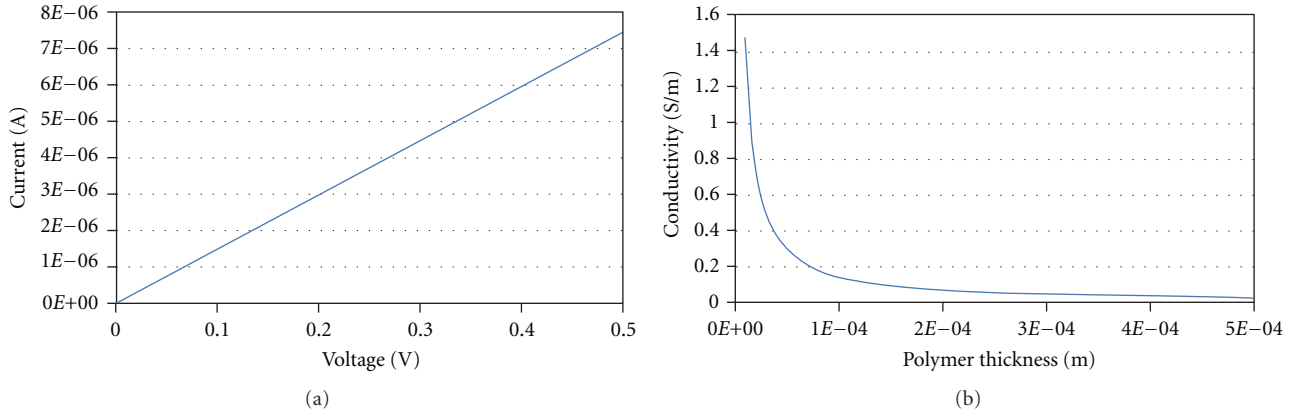


FIGURE 10: Continuity testing. (a) current as a function of an applied ramp voltage and (b) electrical conductivity as a function of the polymer thickness.

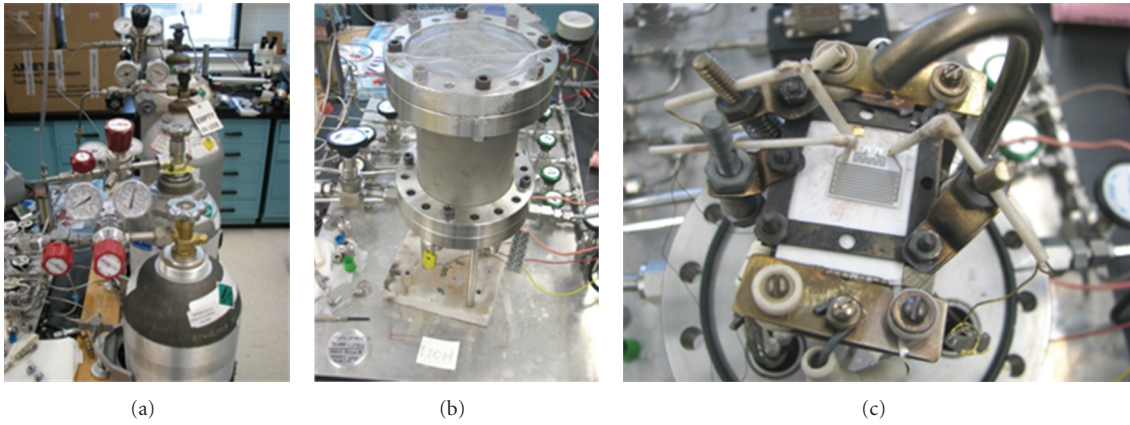


FIGURE 11: (a) argon and hydrogen gas cylinders; (b) the hydrogen/argon gas chamber used for the PANI sensor testing; (c) interior of the chamber and electrical contacts.

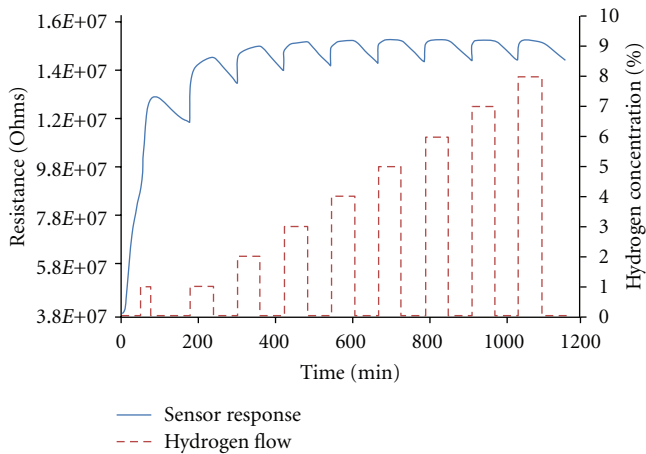


FIGURE 12: PANI hydrogen sensor response as a function of hydrogen gas concentration (dashed line).

TABLE 1: The measured resistances and derived conductivities for various polyaniline polymer formulations.

Sensor designations	Resistance (10^3 ohms)	Conductivity ₁₀₀ (S/m)
CSA-1	68	0.147
CSA-2	758.1	0.0132
CSA-3	4.1	2.42
CSA/CNTs-1	4.0	2.46
CSA/CNTs-2	2.0	4.93
HDEHP-1-A	377.6	0.0265
HDEHP-1-B	91.1	0.11
HDEHP-2-A	102.1	0.098
HDEHP-2-B	105.1	0.095
HDEHP-3-A	28.6	0.35
HDEHP-3-B	7.2	1.39
HDEHP-4-A	0.009	1000
HDEHP-4-B	0.011	882

this figure that the PANI/CSA formulation is sensitive to the presence of hydrogen. However, it is summarized that

the similar responses seen for different hydrogen concentrations are in part due to hydrogen-bonding sites within

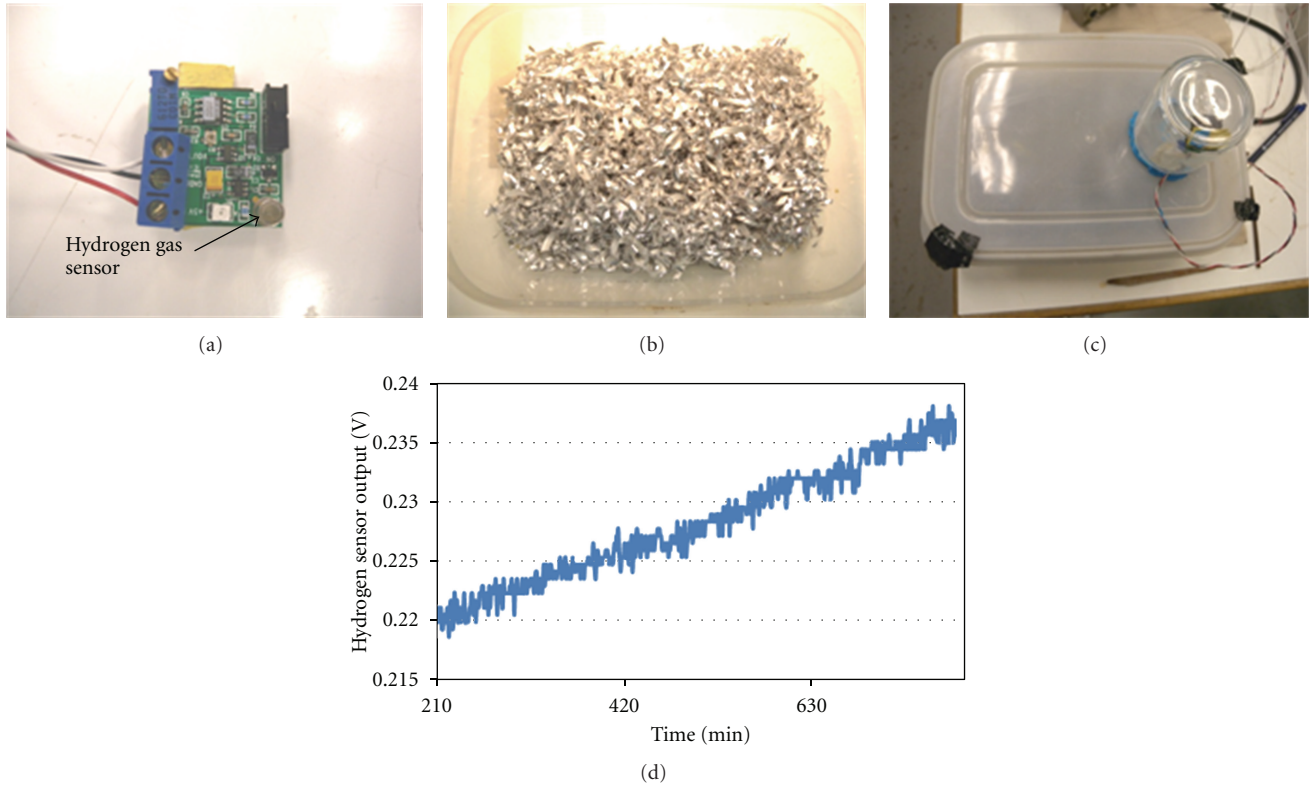


FIGURE 13: (a) hydrogen sensor and evaluation circuit board; (b) 6061-T6 aluminium alloy shards in a plastic container; (c) overview of the test setup showing the glass jar with hydrogen sensor within; (d) the sensor response as a function of hydrogen evolution over time.

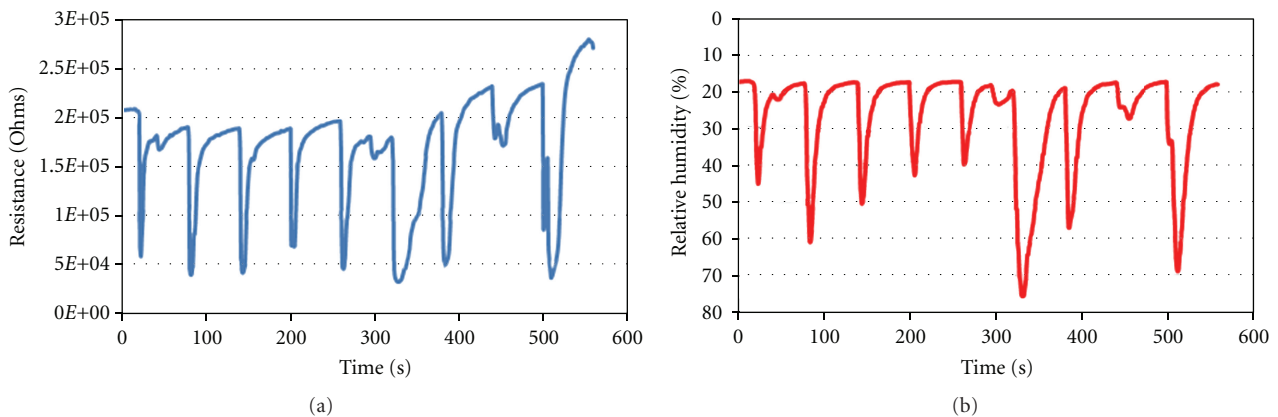


FIGURE 14: Humidity sensor responses. (a) PANI-based humidity sensor and (b) COTS humidity sensor.

the PANI/CSA material not being fully vacated when the flow is stopped or it is possible that the saturation point for this particular PANI/CSA formulation is below 1% hydrogen. Another possibility is that despite curing of the polymer in a desiccator prior to testing, some residual moisture may have remained trapped, thereby limiting the effective sensitivity of the PANI/CSA in these tests.

4.2.2. COTS Hydrogen Sensor. Described here is an experiment in which hydrogen gas was detected evolving from 6061-T6 aluminium alloy in a 5% saltwater solution. This

test was carried out to demonstrate the possibility of measuring hydrogen evolution for corrosion monitoring of aluminium. Testing was carried out with a COTS hydrogen sensor (Kebaili Corporation) as shown in Figure 13(a). This sensor is capable of measuring hydrogen up to 4% per volume in air and is based on the microcatalytic oxidation of hydrogen. The variation of the sensing element resistance due to the exothermic reaction of hydrogen oxidation is directly proportional to the hydrogen concentration. In these tests, the baseline offset of the sensor was set to 215 mV. These “accelerated” corrosion tests consisted of immersing

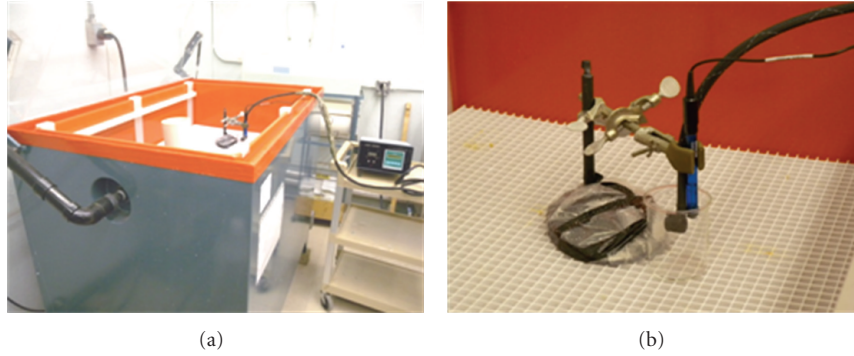


FIGURE 15: (a) salt-fog chamber and (b) chloride ion and material degradation probes.

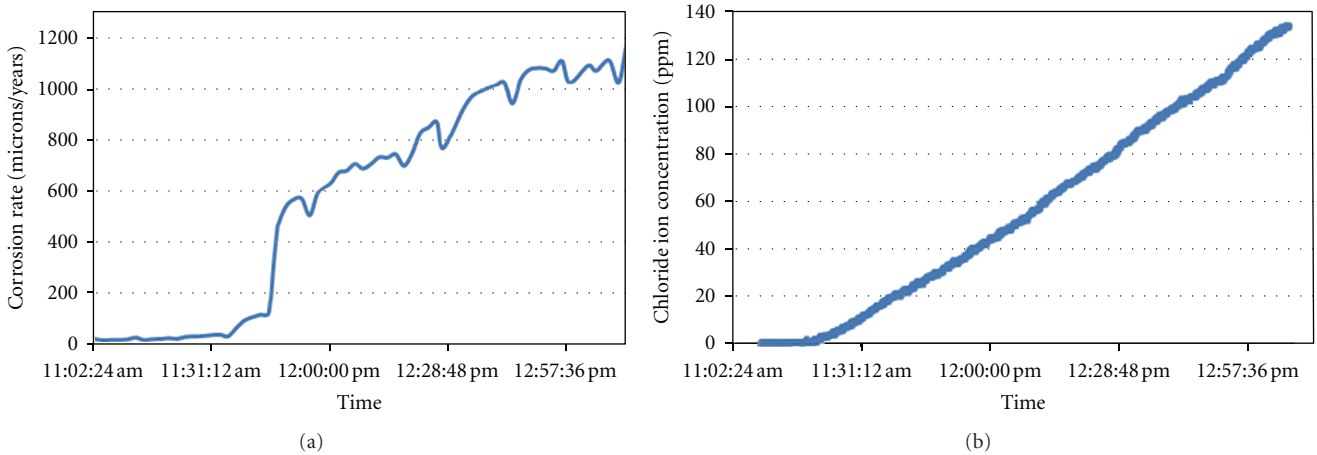


FIGURE 16: A comparison of the corrosion rate for steel with the increase in chloride ion concentration over time.

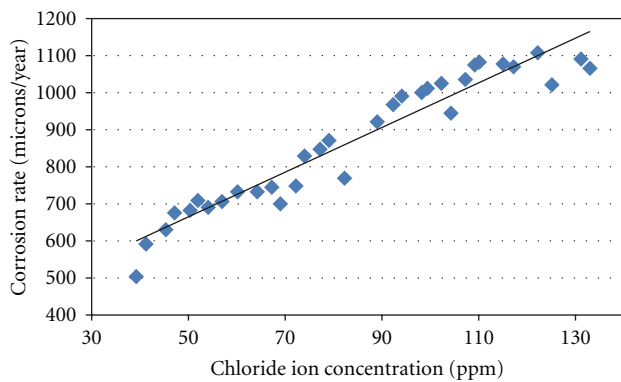


FIGURE 17: Corrosion rate as a function of the chloride ion concentration (solid line is a linear fit to the data).

6061-T6 aluminium alloy shards (Figure 13(b)) into a 5% salt water solution. The hydrogen sensor was affixed inside a 250 mL glass jar and then placed over a small opening in the plastic cover (Figure 13(c)). The glass/plastic interface was sealed with a putty material. The aluminium was left in the saltwater solution for ~36 hours prior to testing. A digitized acquisition system (Omega instruNet) was employed for the data acquisition. The result, shown in Figure 13(d), shows a

gradual increase in the hydrogen concentration over time. In this figure, the sensor output increased by 15 mV over the measuring span, which corresponds to ~3% hydrogen (7.5 mL) within the glass container, which in turn indicates that approximately 6 mg of aluminium was consumed.

For aircraft applications, hydrogen sensing would require an enclosed area, where the diffusion of hydrogen is reduced and the gas concentrations reach levels that are practical for detection. Enclosed fuel storage areas such as under-fuel bladders, where condensation can form and initiate corrosion, are seen as potential areas for monitoring hydrogen gas evolution.

4.2.3. Humidity Sensor Node. Humidity sensor tests were conducted using a small container that allowed the flow of humid air through it. Both a PANI/HDEHP + toluene formulation IDEs sensor and a COTS (Omega RH820) sensor were placed inside the container for humidity sensing. Presented in Figure 14 is a comparison between the humidity sensitive response of the PANI-based and the COTS sensor as a function of time. As can be seen, the PANI sensor responds very well to humidity with excellent response.

4.2.4. Chloride Ion and Material Degradation Sensor Nodes. The chloride ion and material degradation testing was

carried out in a salt-fog chamber (Singleton Corporation) as shown in Figure 15(a). The chloride ion sensor and material degradation sensor were placed into a beaker of deionized water (Figure 15(b)). Salt-fog condensate (3.5% sodium chloride solution) was captured within the beaker and mixed with the deionized water. Data was acquired over a two-hour span. Shown in Figure 16 is a comparison of the increase in chloride concentration and material degradation as a function of time.

Shown in Figure 17 is the dependence of the yearly corrosion rate on chloride ion concentration (40–130 ppm range).

From Figures 16 and 17, it can clearly be seen that salt-fog condensation into the prepared beaker containing deionized is detected by the increase of Cl^- concentration and also in the increase in the corrosion rate of test metal electrodes. For example, a Cl^- concentration of ~ 90 ppm corresponds to a corrosion rate of 900 microns/year. Hence, if such a solution were to remain undetected for an extended period of time, it could cause significant damage to an aircraft structure.

With the cumulative data of the various sensors, it will be possible to cross-correlate the influence of each corrosion parameter. In this way a theoretical corrosion index can be developed. In this regard, further testing is required in order to obtain adequate data for a more in-depth analysis and interpretation. This being said, the corrosion index will provide an indication of the environmental and material conditions so that either preventative or corrective maintenance actions can be taken.

At this stage the sensors are still in the developmental stage. However, as further refinement to the sensing technology is conducted, it is the aim that their use in aircraft will be in areas most prone to corrosion such as the cockpit in fighter aircraft, galley and latrine areas, or any other area prone to the accumulation and retention of moisture.

5. Conclusions

Part of the ongoing development of a multiparameter integrated corrosion sensor, consisting of carbon nanotube/polyaniline-based and commercial-off-the-shelf sensors, has been presented. This paper also described the integration methodology being investigated for the various sensor nodes and presented preliminary chloride ion, humidity, and temperature data acquisition capabilities. Also, experimental test results were presented for chloride ion concentration, hydrogen gas evolution, humidity variations, and material degradation. The integrated corrosion sensor development program presented here intends to provide a condition-based approach to aircraft maintenance protocols through a data-intensive maintenance scheduling methodology in order to tailor maintenance schedules for structural/component/material requirements as opposed to operating under predefined inspection timetables. Through data fusion, environmental and material factors were proposed for determining a corrosion index, which in turn was suggested for developing condition-based maintenance protocol consisting of both preventative and corrective maintenance scheduling.

Acknowledgments

The technical support given by Dr. Gerardo Diaz-Quijada and Dr. Bhavana Deore from NRC Steacie Institute for Molecular Sciences, and Dr. Jim Tunney and Dr. Jeffrey Dunford from NRC Institute for Chemical Process and Environmental Technology is gratefully acknowledged.

References

- [1] C. M. Hansson, "The impact of corrosion on society," *Metallurgical and Materials Transactions A*, vol. 42, no. 10, pp. 2952–2962, 2011.
- [2] A. Winkleman, E. B. Svedberg, R. E. Schafrik, and D. J. Duquette, "Preventing corrosion from wearing our future away," *Advanced Materials and Processes*, vol. 169, no. 3, pp. 26–31, 2011.
- [3] N. Symonds and C. Pitt, "Military helicopters: have the seeds of future accidents already been sown?" *Engineering Failure Analysis*, vol. 13, no. 3, pp. 493–515, 2006.
- [4] Accident Report: Aloha Airlines, "Flight 243, national transportation safety board," Tech. Rep. NTSB/AAR-89/03, 1989.
- [5] A. Jaya, U. H. Tiong, and G. Clark, "The interaction between corrosion management and structural integrity of aging aircraft," *Fatigue and Fracture of Engineering Materials and Structures*, vol. 35, no. 1, pp. 64–73, 2012.
- [6] W. Wallace, D. W. Hoepfner, and P. V. Kandachar, "AGARD corrosion handbook volume 1—aircraft corrosion: causes and case histories," Tech. Rep. AGARD-AG-278, North Atlantic Treaty Organization, 1985.
- [7] R. M. Chlistovsky, P. J. Heffernan, and D. L. DuQuesnay, "Corrosion-fatigue behaviour of 7075-T651 aluminum alloy subjected to periodic overloads," *International Journal of Fatigue*, vol. 29, no. 9–11, pp. 1941–1949, 2007.
- [8] G. Rinaldi, "Chloride ion and humidity sensor for aluminum corrosion monitoring: sensor technology selection and overview," Defence R&D Canada, Technical Note DRDC-Atlantic TN 2009-209, 2009.
- [9] <http://www.rcaf-arc.forces.gc.ca/v2/netpub/index-eng.asp?mode=1>.
- [10] K. S. Lewis, J. Yuan, and R. G. Kelly, "Chemical conditions inside occluded regions on corroding aircraft aluminum alloys," *Journal of Chromatography A*, vol. 850, no. 1-2, pp. 375–380, 1999.
- [11] A. Tosun, M. Ergun, M. Balbaşı, and M. Tamirci, "The use of experimental design method for the investigation of pitting potential of aluminum," *Materials and Corrosion*, vol. 58, no. 7, pp. 502–505, 2007.
- [12] K. F. Lorking and J. E. O. Mayne, "The corrosion of aluminium," *Journal of Applied Chemistry*, vol. 11, pp. 170–180, 1961.
- [13] C. Vargel, *Corrosion of Aluminium*, Elsevier, 2004.
- [14] L. Soler, J. Macanás, M. Muñoz, and J. Casado, "Aluminum and aluminum alloys as sources of hydrogen for fuel cell applications," *Journal of Power Sources*, vol. 169, no. 1, pp. 144–149, 2007.
- [15] J. Skrovan, A. Alfantazi, and T. Troczynski, "Enhancing aluminum corrosion in water," *Journal of Applied Electrochemistry*, vol. 39, no. 10, pp. 1695–1702, 2009.
- [16] T. E. Graedel, "Corrosion mechanisms for aluminum exposed to the atmosphere," *Journal of the Electrochemical Society*, vol. 136, no. 4, pp. 204C–212C, 1989.

- [17] T. Urabe, M. Tanaka, S. Kumakura, and T. Tsugoshi, "Study on chemical speciation in aluminum chloride solution by ESI-Q-MS," *Journal of Mass Spectrometry*, vol. 42, no. 5, pp. 591–597, 2007.
- [18] A. A. Mazhar, W. A. Badawy, and M. M. Abou-Romia, "Impedance studies of corrosion resistance of aluminium in chloride media," *Surface and Coatings Technology*, vol. 29, no. 4, pp. 335–345, 1986.
- [19] R. M. Stevanović, A. R. Despić, and D. M. Dražić, "Activation of aluminium in chloride containing solutions," *Electrochimica Acta*, vol. 33, no. 3, pp. 397–404, 1988.
- [20] T. H. Nguyen and R. T. Foley, "The chemical nature of aluminum corrosion: II. The initial dissolution step," *Journal of the Electrochemical Society*, vol. 129, no. 1, pp. 27–32, 1982.
- [21] A. Sarpola, V. Hietapelto, J. Jalonen, J. Jokela, and R. S. Laitinen, "Identification of the hydrolysis products of $AlCl_3 \cdot 6H_2O$ by electrospray ionization mass spectrometry," *Journal of Mass Spectrometry*, vol. 39, no. 4, pp. 423–430, 2004.
- [22] H. W. von Kohlschütter and P. Hantelmann, "Basische Aluminiumchloride," *Zeitschrift für Anorganische und Allgemeine Chemie*, vol. 248, pp. 319–344, 1941 (German).
- [23] A. Reza, A. Kemal, and P. E. Markey, "Runaway reactions in aluminum, aluminum chloride, HCl, and steam: an investigation of the 1998 CONDEA vista explosion in Maryland," *Process Safety Progress*, vol. 21, no. 3, pp. 261–267, 2002.
- [24] S. N. Rashkeev, K. W. Sohlberg, S. Zhuo, and S. T. Pantelides, "Hydrogen-induced initiation of corrosion in aluminum," *Journal of Physical Chemistry C*, vol. 111, no. 19, pp. 7175–7178, 2007.
- [25] A. G. Macdiarmid, J. C. Chiang, A. F. Richter, and A. J. Epstein, "Polyaniline: a new concept in conducting polymers," *Synthetic Metals*, vol. 18, no. 1–3, pp. 285–290, 1987.
- [26] T. A. Huber, "A literature survey of polyaniline, Part 1: polyaniline as a radar absorbing material," Defence R&D Canada, Technical Memorandum DRDC-Atlantic TM 2003-014, 2003.
- [27] T. Huber, P. Saville, and D. Edwards, "Investigations into the polyaniline and polypyrrole families of conducting polymers for application as radar absorbing materials," Defence R&D Canada, Technical Memorandum DRDC-Atlantic TM 2003-005, 2003.
- [28] C. Chow and T. Huber, "The potential of conducting polymer—carbon nanotube composites as supercapacitor electrodes," Defence R&D Canada, Technical Memorandum DRDC-Atlantic TM 2007-320, 2007.
- [29] P. C. Ramamurthy, A. M. Malshe, W. R. Harrell, R. V. Gregory, K. McGuire, and A. M. Rao, "Polyaniline/single-walled carbon nanotube composite electronic devices," *Solid-State Electronics*, vol. 48, no. 10–11, pp. 2019–2024, 2004.
- [30] C. Conn, S. Sestak, A. T. Baker, and J. Unsworth, "A Polyaniline-based selective hydrogen sensor," *Electroanalysis*, vol. 10, no. 16, pp. 1137–1141, 1998.
- [31] J. D. Fowler, S. Virji, R. B. Kaner, and B. H. Weiller, "Hydrogen detection by polyaniline nanofibers on gold and platinum electrodes," *Journal of Physical Chemistry C*, vol. 113, no. 16, pp. 6444–6449, 2009.
- [32] S. Srivastava, S. S. Sharma, S. Kumar, S. Agrawal, M. Singh, and Y. K. Vijay, "Characterization of gas sensing behavior of multi walled carbon nanotube polyaniline composite films," *International Journal of Hydrogen Energy*, vol. 34, no. 19, pp. 8444–8450, 2009.
- [33] M. Matsuguchi, T. Yamanaka, M. Yoshida, S. Kojima, and S. Okumura, "Long-term stability of humidity sensor using polyaniline blend films upon DC operation," *Journal of the Electrochemical Society*, vol. 156, no. 10, pp. J299–J302, 2009.
- [34] M. L. Singla, S. Awasthi, and A. Srivastava, "Humidity sensing; using polyaniline/ Mn_3O_4 composite doped with organic/inorganic acids," *Sensors and Actuators B*, vol. 127, no. 2, pp. 580–585, 2007.
- [35] F.-W. Zeng, X.-X. Liu, D. Diamond, and K. T. Lau, "Humidity sensors based on polyaniline nanofibres," *Sensors and Actuators B*, vol. 143, no. 2, pp. 530–534, 2010.